Experimental Study of Foam Generation and Flow in Carbonate Fracture Systems

Master Thesis in Reservoir Physics

Snorre Sande Vasshus

Department of Physics and Technology

University of Bergen

June 2016

Abstract

This experimental thesis study foam generation during co-injection of gas and surfactant in three fracture systems with increasing size: 2-inch core, 4-inch core and a fractured block network. Important parameters established experimentally were 1) the gas fraction and injection rate that generated the strongest and most stable foams, 2) the injection strategy that produced the highest differential pressure, 3) the outlet conditions that reduced the gas compressibility effect, and 4) the effect of fracture system size to generate foam. The rock material used was an impermeable marble without porosity, and fluid flow and foam generation therefore only occurs within the fracture network itself.

A total of 20 co-injections for in-situ foam generation were conducted to systematically evaluate the effects of differences in total injection rate, injection strategy (increasing/decreasing gas fraction flow) and backpressure conditions. The results show that the strongest foams were generated at high gas fraction (fg=0.8-0.9) for all three fracture systems, and corroborates with both theory and previous work. Foam stability was evaluated based on reduction in differential pressure from its peak (usually fg~0.8-0.9) to when only gas was injected (fg=1.0). Foam stability was influenced by the fraction of stationary/trapped gas, the injection rate and the effect of gas compressibility. Increased injection rate influenced foam stability negatively because of an increased viscous drag, and hence displacement of non-stationary foam bubbles, resulting in a decline in pressure. The highest relative increase (from start to peak) and the lowest reduction (from peak to end) in differential pressure was observed during co-injections with lowest (relative) total injection rate.

In addition to consistent foam generation, hysteresis effects were observed when changing the injection strategy between subsequent co-injections for the 2-inch core and fractured block. Effects of hysteresis were especially apparent in the results from the 2-inch core, and displayed a substantial saturation of trapped gas, presumably due to considerable gas saturation prior to the co-injection with decreasing gas fraction. The significance of initial gas saturations on the effects of hysteresis was in accordance with the literature. A range of co-injections with variation in backpressure demonstrated that a sufficiently high backpressure reduced adverse gas compressibility effects and contributed positively on foam stability.

Using an injection rate scaled for size, the larger 4-inch fracture system generated higher differential pressure compared with the 2-inch system. The 4-inch system demonstrated higher differential pressure for all gas fractions, with a more finely textured foam, which was observed in the transparent production tubing. Access to local changes in saturation was obtained through visual inspection for the block network, and using a positron emission tomography (PET) imaging approach for the two cores. PET visualization was performed at Haukeland University Hospital, applying the radioactive isotope ^{18}F as a nuclear tracer in the liquid surfactant solution phase. The imaging displayed foam's ability to block and divert fluid flow as large variations in fluid distribution.

Acknowledgements

First and foremost, I would like to thank my supervisor Associate Professor Martin A. Fernø and laboratory assistant Inez Buzdugan at the Department of Physics and Technology, University of Bergen. In addition I want to acknowledge Geir Ersland, Marianne Steinsbø, Jarand Gauteplass, Bergit Brattekås and Professor Arne Graue. Thank you all for giving me the opportunity to work with challenging research subjects within reservoir physics as well as support and guidance with this thesis. I would also like to thank the mechanical workshop at the department and the PhD Candidates Arthur Uno Rognmo and Stian Almenningen for sharing their experience and knowledge in scientific discussions.

A special thanks goes to my lab partner, fellow master student and friend Sigbjørn Aasheim Johansen. We have certainly been through a tremendous amount of hours of hard work, dedication, determination, frustration, fascination and jubilation. There were times where we did not quite know what we did, what to expect or how we were going to do it – but in the end we made it. I think our mental toughness and exceptional collaboration has provided a research foundation to be proud of, and it has been a real pleasure to do it together with you!

Even though this thesis is produced by myself, I want to emphasize that I would not have been able to do it without the support of my friends and fellow master students at UiB. Thank you all for fun times and laughter, making my years as a student an invaluable time that I will never forget. A quick shout-out to TG, HC Andersen, PTEK FC and Svigjengen.

I want to express my deepest appreciation to my parents Helge and Marit, and my brother Krister for unconditional support, motivation and advises in sports, studies and life through all my years of learning and studying.

Finally, a sincere thanks to my dearly beloved girlfriend Hilde for being an essential part of my life and always making me want to achieve ambitious goals. You are simply my biggest drive in life.

Bergen, June 2016

Table of Contents

Abstract 3
Acknowledgements 5
Thesis Rationale 9
Chapter I – Theory 11
1 Fundamentals 12
1.1 Mobility ratio 12
1.2 Interfacial Tension 12
1.3 Capillary Pressure 13
1.4 Oil Recovery and Displacement Efficiency 13
1.5 Imaging Techniques and Visualization 16
1.6 Scaling/Perspective 17
2 Fractured Reservoirs 19
2.1 Characterization of Fractures and Fractured Carbonate Reservoirs 19
2.2 Recovery Mechanisms in Fractured Reservoirs 21
3 Theory and Application of Foam 23
3.1 Foam Fundamentals 23
3.2 Foam EOR 30
3.3 Field Reports/Literature Survey 33
Chapter II - Experimental Procedures 37
4 Fractured Systems and Fluids 38
4.1 Fractured Block System 38
4.2 Fractured Marble Cores 39
4.3 Fluids 46
5 Foam Generation and Visual Inspection of Foam Flow in Fractured Block System 47
5.1 Setup and Equipment 47
5.2 Laboratory Procedures 48
6 Foam Generation in Fractured Marble Cores 49
6.1 Setup and Equipment 49
6.2 Laboratory Procedures 52
7 Visualization of Fractures and Foam Flow in Fractured Cores Using PET/CT 53
7.1 Laboratory Procedures 54

Chapter III – Results and Discussion 55
8 Characterization of Fracture Networks 56
8.1 Fracture System in 2-inch Core 56
8.2 Fracture System in 4-inch Core 60
8.3 Fracture System in Rectangular Block 61
9 Foam Generation by Co-Injection in Fractures 63
9.1 2-inch Fractured Marble Core 63
9.2 4-inch Fractured Marble Core 75
9.3 Fractured Block System 76
10 Visualization of Foam Flow/Propagation in Fractures 80
10.1 Visualization of Foam Flow in The 2-inch Fractured Core Using PET/CT 80
10.2 Visualization of Foam Flow in The 4-inch Fractured Core Using PET/CT 91
10.3 Visual Inspection of Foam Flow/Propagation in Fractured Block System 94
Chapter IV – Conclusions and Future Work 99
11 Conclusions 100
12 Future Work 102
Chapter V – Appendix and References 103
Appendix A – Uncertainties and Calculations 104
Appendix B – Experimental Overview 106
Appendix C – Nomenclature 107
Appendix D – Abbreviations 108
Appendix E - Additional Theory 109
AE.1 Capillary Pressure 109
AE.2 Capillary Number 111
Appendix F – PET/CT Imaging 113
References 117

Thesis Rationale

The worldwide demand for energy is steadily increasing in line with overall technological development globally. The majority of societies are dependent on technology and every day solutions that are largely based on energy that sources from fossil fuels. Oil and gas are therefore highly likely to remain among the main energy resources in the foreseeable future. Numerous speculations of peak-oil production has been projected, the most famous probably from (Hubbert, 1956), whom reported that ultimate world crude-oil production would decline after year 2000. The fact is, however, that never has petroleum been produced in volumes like today. The increased oil production is due to innovation, new solutions and improved technology that enhance oil recovery. At the same time, it is recognized that many conventional reservoirs have matured, in addition to an overall decrease in new discoveries.

About 60% of the world's oil and 40% of the world's gas reserves are stored in carbonate reservoirs (Schlumberger, 2016). Carbonate reservoirs are generally heavily fractured and exhibit large reservoir heterogeneities in terms of both porosity and permeability (Chilingar and Yen, 1983). High conductivity through the fractures usually leads to a rapid decline in production and low ultimate (total) recoveries (Allan and Sun, 2003). The largest fraction of hydrocarbons in carbonate reservoirs are stored in the matrix blocks (Bratton et al., 2006). Water injection as an IOR method is usually inefficient in a majority of fractured carbonate reservoirs because of mixed-wet and oil-wet rock preferences, causing the water to preferentially flow through the fractures instead of spontaneously imbibing into the matrix, leading to an early water breakthrough (Singh and Mohanty, 2016). After primary and secondary oil recovery methods, residual oil saturations are often ranging as high as more than 50% of OOIP (oil initially in place). Volumes of oil may be bypassed by viscous fingering because of an unfavorable mobility ratio, or saturations may become trapped and immobile by snap-off due to capillary pressure. In gasflooding, gravity segregation and channeling may occur because of the high mobility and low density of gas, which results in a decreased recovery potential. This has raised the industry's focus on extracting the remaining oil by implementing tertiary recovery methods involving chemically altered compositions not originally present in the reservoir.

An oilfield's recovery factor (reservoir displacement efficiency) is strongly dominated by the capillary number, which is defined as the ratio of viscous to capillary force, and the mobility ratio between the displacing fluids. The recovery factor is a product of microscopic displacement and volumetric sweep efficiency, and EOR techniques focus on increasing these in order to reduce residual oil saturation. Foam as an EOR method has displayed promising characteristics to improve sweepp efficiency by reducing gas mobility and divert fluid flow to unswept zones both in the laboratory and field scale (Bernard et al., 1980, Schramm, 1994). However, there are still much to learn about foam fundamentals in order to make it commercially feasible/viable. This thesis focus on in-situ foam generation by co-injection of surfactant solution and gas, and foam flow/propagation in fractures. Foam flow and foam

generation in fractures is not fully understood and more experimental studies needs to be quantified in order to improve dynamic foam simulators (Buchgraber et al., 2012). It is standard procedure to simulate results from the laboratory in a field scale by using upscaling techniques before any field application is implemented. It is therefore essential that the dynamic simulations are reliable and based on input data from credible scientific research.

This thesis consist of 5 chapters, divided into 12 sections. Chapter I introduce relevant theoretical foundation that this thesis is built upon, with the purpose of familiarizing the reader to fundamental concepts required for analyzing results and discussing the underlying reservoir physics. Chapter II presents the rock material and fluids used, experimental setups and procedures. Results and discussion are presented in Chapter III. Conclusions and future work are presented in Chapter IV. Chapter V contains Appendix A-F and the references used in this thesis. Appendix A describes uncertainties related to this thesis, Appendix B includes a detailed experimental overview, Appendix C and Appendix D lists the nomenclature and abbreviations, respectively. Appendix E contains complimentary theory, and Appendix F presents enlarged PET/CT images.

Chapter I – Theory

1 Fundamentals

1.1 Mobility ratio

An important factor controlling fluid flow is the mobility ratio, defined as the relationship between the mobility of the displacing fluid λ_i and the displaced fluid λ_j:

$$M = \frac{\lambda_i}{\lambda_j} = \frac{\frac{k_{ri}}{\mu_i}}{\frac{k_{rj}}{\mu_j}} \quad (1)$$

where k_r [m^2] is the relative permeability, μ [Pas] is the viscosity and the subscript i and j denotes the displacing and displaced fluids, respectively. During multiphase flow the mobility ratio describes the displacement stability. Floods with low mobility ratio (M < 1) are considered efficient with a stable displacement front. On the contrary, if the mobility ratio is high (M > 1), the higher mobility of the displacing phase compared to that of the displaced phase is likely to cause viscous fingering and bypassing of oil (Warren and Cosgrove, 1963). It is the residual oil/bypassed oil that is the target for enhanced oil recovery techniques, and foam has displayed promising characteristics for mobility control. This will be discussed more detailed in **Section 3**.

1.2 Interfacial Tension

When two fluids are in contact with each other there exists a membrane-like surface that separates the fluids with relatively strong intermolecular cohesion, defined as interfacial tension, σ (Zolotukhin and Ursin, 2000). The extent of the interfacial tension represents the amount of energy that keeps the two fluids apart, and if the temperature is kept constant this energy depends on the chemical composition of the fluids. The interfacial tension may result in three different outcomes:

- A positive interfacial tension ($\sigma > 0$) implicates that the fluids are immiscible, meaning that the molecules in both fluids have a higher attraction for its own kind
- A neutral interfacial tension ($\sigma \approx 0$) implicates that the fluids are miscible, meaning that the molecules in each fluid are equally attracted to both fluids. The fluids will mix by diffusion and after a given time become truly miscible when equilibrium is reached.
- A negative interfacial tension ($\sigma < 0$) implicates that molecules of both fluids are strongly attracted to each other, and will start mixing instantaneously, creating a new fluid in a process called dissolution.

Surfactants present in foams can reduce the interfacial tension between fluids, and hence enhance foam stability.

1.3 Capillary Pressure

It is important to evaluate capillary pressure concepts, as they can give valuable and key reservoir information like (Ahmed, 2010):

- Determining reservoir fluid saturations and depths of fluid contacts
- Measure the height above the free water level
- Estimate thickness of a transition zone
- Measure pore throat radii distribution and pore-level heterogeneity
- Evaluation of reservoir rock quality and wetting characteristics
- Improve reservoir modelling

A definition of capillary pressure is given as:

$$P_c = \frac{2\sigma_{ij}cos\theta_{ij}}{r} \tag{2}$$

where σ_{ij} [J/m^2] is the interfacial tension between the phases i and j, θ_{ij} [degree angle] is the wetting angle between phases i and j, and *r* [m] is the radius of capillary. **Equation (2)** shows that the capillary pressure is lowest in the bigger pores, and highest in the smaller ones. There are especially two capillary pressure processes of interest: drainage and imbibition. Imbibition describes a process in which an increase in the wetting phase saturation is observed, whereas a drainage process refers to a situation where an increase in the saturation of the non-wetting phase is observed. These processes displace reservoir fluids differently. In a drainage process, the non-wetting fluid will penetrate and displace the middle of the pores, while in an imbibition process the wetting fluid will propagate and displace along the pore walls.

1.4 Oil Recovery and Displacement Efficiency

Oil recovery techniques are traditionally divided into three phases: primary, secondary and tertiary. These phases describes the production from a reservoir as a sequence of techniques of increasing cost and complexity (Ahmed, 2010). Primary recovery is the initial production stage and utilizes the energy naturally present in the reservoir. Natural energy sources are solution-gas drive, gas-cap drive, natural water drive, fluid and rock expansion and gravity drainage (Dake, 1978). As the reservoir depletes and the pressure declines, the production slows down. Once the system is no longer able to produce oil at profitable production rates, secondary recovery mechanisms are implemented, if economically feasible. Secondary recovery is associated with the augmentation of the reservoir's natural energy through injection of, most commonly, water or gas for pressure maintenance, re-pressurization or displacement of oil to production wells. Gas injection, in this case, displaces oil immiscibly. Gas processes based on oil swelling, oil viscosity reduction or favorable phase behavior are considered enhanced oil recovery (EOR) processes – tertiary production mechanisms (Donnez, 2007, Skarestad and Skauge, 2014). Tertiary recovery, the third phase of

production, uses miscible gases, chemicals and/or thermal energy to displace additional oil after the secondary recovery process becomes uneconomical (Zolotukhin and Ursin, 2000).

Dake (1978) defines that the overall displacement efficiency can be considered as the product of microscopic and macroscopic displacement efficiencies and can be written as:

$$E_R = E_D \cdot E_{vol} \tag{3}$$

where E_R is the recovery factor, E_D is the microscopic displacement efficiency and E_{vol} is the volumetric sweep efficiency. The microscopic displacement efficiency is defined as the ratio between the volume of displaced fluid and the volume of contacted fluid:

$$E_D = \frac{Volume\ of\ displaced\ fluid}{Volume\ of\ contacted\ fluid} \tag{4}$$

The volumetric sweep efficiency is defined as:

$$E_{vol} = \frac{Volume\ of\ contacted\ fluid}{Total\ fluid\ volume} \tag{5}$$

Microscopic displacement relates to the remobilization of oil at the pore scale, and is a measure of the effectiveness of the displacing fluid in mobilizing oil at those places in the rock where the displacing fluid contacts the oil (Cook, 2012). The efficiency is reflected in the magnitude of the residual oil saturation in the region contacted by the displacing fluid. The reader may review **Appendix E** for additional details.

Macroscopic displacement efficiency relates to how effective the displacing fluid(s) is/are contacting the reservoir in a volumetric sense, and is a measure of how effectively the displacing fluid sweeps out the volume of a reservoir, both areally and vertically (Ahmed, 2010, Donnez, 2007). The efficiency is reflected in the magnitude of average or overall residual oil saturation, because the average is based on residual oil in both swept and unswept parts of the reservoir. The macroscopic displacement efficiency is improved by maintenance of favorable mobility ratios between all displaced and displacing fluids throughout a process (Cook, 2012). Another factor important for good volumetric sweep is the density difference between the displaced and displacing fluids. Significant density difference can result in gravity segregation – either the underriding or overriding of the fluid being displaced, effectively bypassing fluids at the top or bottom of a reservoir. In dipping reservoirs however, this might be used to advantage by injecting in an updip or downdip direction, depending on the density difference between the injectant and displaced fluid.

The character of an EOR process can be evaluated from the values of the microscopic and macroscopic displacement efficiencies, and consequently the overall recovery factor, ref. **Equation (3).** Ideally, the value should be close to 1. Developing fluids with the required properties to give this result cost effectively is the major challenge for EOR technology in the years ahead.

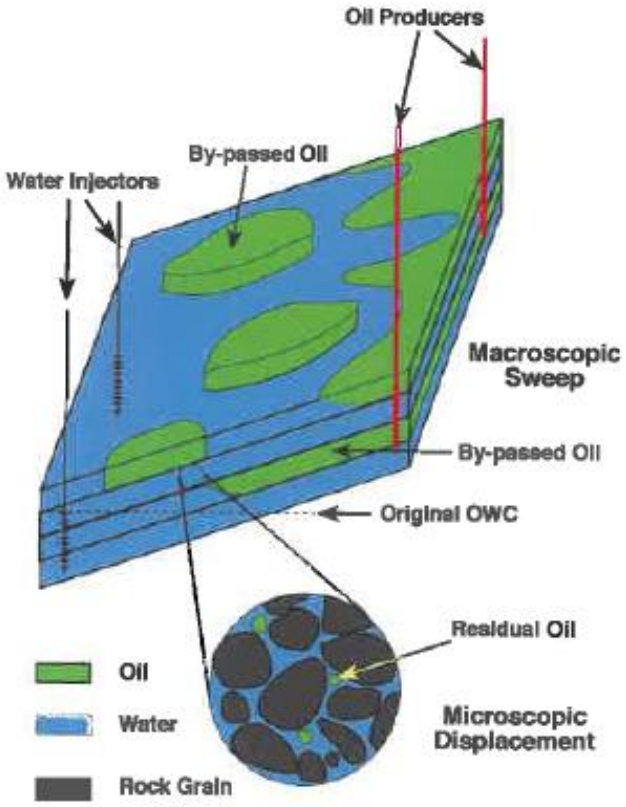

Figure 1: Unswept oil during displacement by water. The residual oil saturation remains as a result of two factors. Firstly, oil remains capillary trapped in areas swept by water, and secondly, a large portion of the reservoir is not contacted by the injected water. This residual oil is the target of EOR techniques. From (Cook, 2012).

1.5 Imaging Techniques and Visualization

Imaging experiments in-situ provides a beneficial supplement to pressure data gathered from laboratory experiments. Visualization of multiphase flow and behavior in-situ contributes to obtain a better understanding and knowledge of a system's underlying reservoir physics. The imaging techniques used in this thesis are briefly discussed below.

1.5.1 Computed Tomography (CT)

A Computed Tomography consists of an X-ray source and a series of detectors. The X-ray source emits electromagnetic radiation while rotating around the sample. The detectors are positioned on the opposite side of the X-ray source. These detectors measure the X-ray attenuation as they pass through materials with different density. When electromagnetic radiation passes through matter the intensity decreases (Ketcham and Carlson, 2001). One of the most important parameters in a CT scan is the voltage. The voltage regulates the energy of the X-rays. High voltage means more energetic X-rays, which determines the penetration ability of the beams. The main advantage of an industrial X-ray CT is the high resolution, which can be as low as a few microns. A crucial part of the CT-scanner is the motion controller. Because each slice can be a few microns thick, it is important that the movement is very precise. If the position is changed during an experiment, it has to be redone. After rotating around the object/sample one time, a two-dimensional image (called slice) can be computed based on the density difference between the sample and its environment. Many 2D slices can then be compiled together to create a 3D representation of the sample.

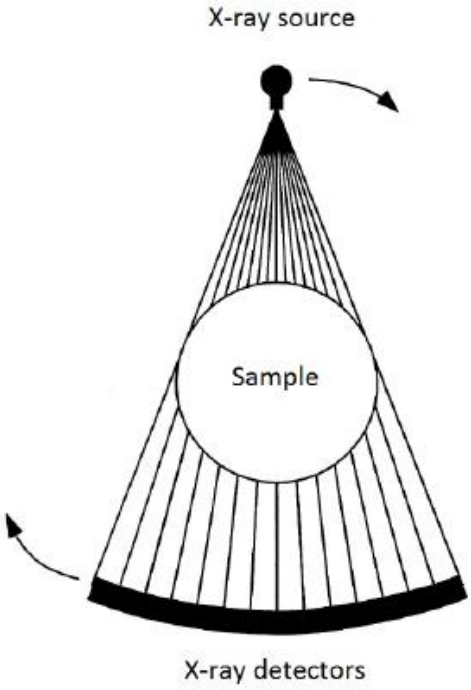

Figure 2: Schematic illustration of a rotate-only CT scan geometry. The concept is based on a X-ray source that rotates around the sample as it emits radiation. The detectors are on the opposite side of the sample and measures the ectent to which the X-rays have been attenuated by the sample. Figure from (Lie, 2013).

1.5.2 Positron Emission Tomography (PET)

Positron Emission Tomography (PET) uses the emitted radiation from radioactive isotopes to visualize in-situ fluid flow. The radioactive isotope can be solved/mixed in one of the phases, individually labeling fluids of interest. The radioactive isotope is produced in a cyclotron and added to the designated injection fluid. In this thesis, Fluorodeoxyglucose (^{18}F - FDG) was used to label the liquid surfactant solution. ^{18}F has a half-life of approximately 110 minutes. The isotope emits a positron (a positively charged electron) which interacts with an orbiting electron. This interaction results in a complete annihilation of both the positron and electron, releasing two energetic photons emitted at almost 180^{o} at each other (Omami et al., 2014). Detectors are placed in a circular ring around the scanned object/sample, which detects the directionality of the emitted photons and provides a mechanism for localizing the origin of the photons and hence the radioactive radiation as the isotope decays.

Images sequentially acquired from both CT and PET can be combined into a single co-registered image: functional imaging obtained by PET depicts dynamic fluid flow, which is correlated with the imaging of the sample's static geometry (fracture network) obtained by CT scanning. The result is a fascinating visualization of dynamic fluid flow in the fractured marble cores.

1.6 Scaling/Perspective

Fractured blocks and core plugs are used in this thesis to investigate foam generation in fractured systems. 3D visualization techniques are used to give a unique insight/knowledge in the foam generation and propagation process through the fractures, and will be helpful in describing foam formation and foam flow behavior. The objective is to produce reliable qualitative and quantitative data that can improve foam simulators in dynamic reservoir models.

Challenges and uncertainty related to oil recovery, combined with the overall requirement that reservoir operations are carried out in a cost-efficient, reliable and sustainable manner, has led the oil and gas industry to be engaged and interested in research and development programs using suitable scaling techniques to uncover the underlying mechanisms of reservoir management. Common laboratory scales are that of micromodels (micrometers), coreplugs and blocks (centimeters). The objective of laboratory studies is to better understand the physical and chemical properties of reservoir rocks, and provide awareness of the strengths and weaknesses encountered in different oil recovery processes to reduce uncertainty in reservoir evaluation (Kull et al., 1984). Fluid properties, reservoir fluid flow and recovery mechanisms are simulated at different conditions to describe the complexity of field scale flow. However, experimental studies of the mechanisms attributed to multiphase flow at the laboratory are conducted at scales completely different from that of a petroleum reservoir.

One must therefore be cautious to draw direct conclusions to field scale reservoir performance and production. Subsequently, in reservoir operations, core analysis should not be treated as a stand-alone technology. Integration with wireline logs, geophysical data, well tests, production data and other reservoir evaluation tools increase the value of any analysis conducted at the laboratory.

Upscaling is necessary to bridge different scaled measurements/data from laboratory pore, core and block experiments to reservoir conditions (Kumar et al., 1997). Dynamic reservoir models and software are used almost exclusively to implement data obtained from experiments and other reservoir evaluation tools to simulate field flow behavior prior to any field intervention or field pilot. The disparity in scale between core measurements and simulator grid-blocks is typically at least an order of magnitude (from centimeters to several meters). Because each grid-block can only be attributed with one average value for every fluid parameter, an effective, robust/reliable and accurate averaging technique is required when upscaling from core scale (Lohne et al., 2006). For more details regarding technical specifics of laboratory data upscaling, the reader may review the investigations by Das and Hassanizadeh (2005), Kossack et al. (1989) and Kumar and Jerauld (1996).

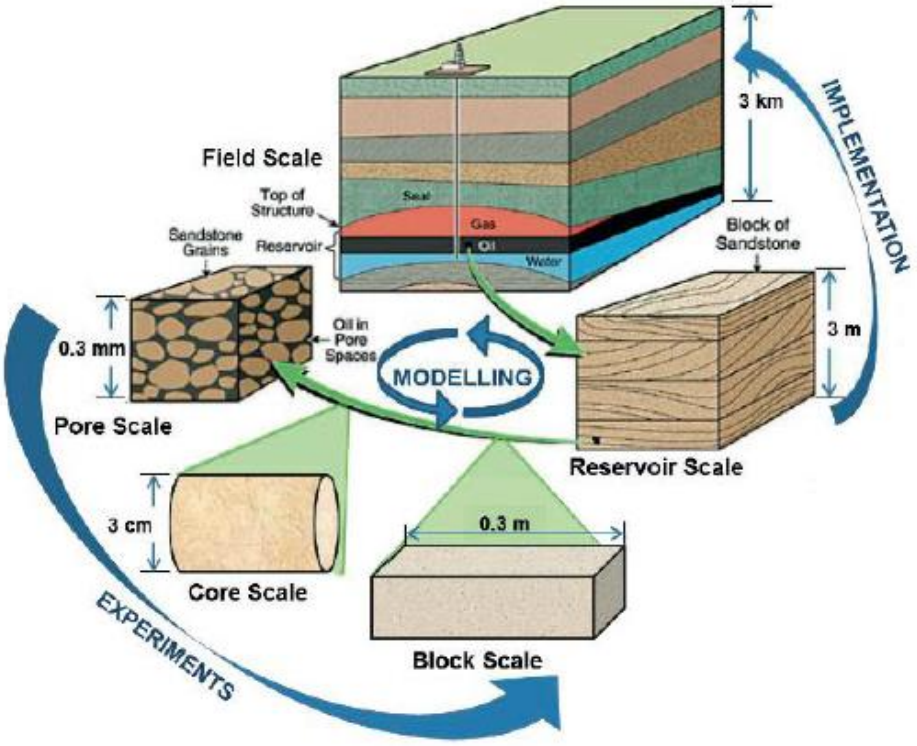

Figure 3: Various scales used in petroleum research for descriptive analysis of oil and gas reservoirs (Brattekås, 2014). This thesis consist of results from experiments conducted at the core and block scale.

2 Fractured Reservoirs

2.1 Characterization of Fractures and Fractured Carbonate Reservoirs

The ability to understand and predict the characteristics of fractures and fractured networks is essential for reservoir characterization and the assessment of fluid flow behavior when developing and modelling fractured reservoirs. A fracture is a macroscopic planar discontinuity, normally induced geomechanically over time by rock deformation or physical diagenesis that may modify rock characteristics (Nelson, 2001). Aperture, orientation and density are the three main features of importance when it comes to establishing a realistic understanding of a fracture network (Ersland, 2008). Fractures may be open, sealing or partly sealing depending on the degree of precipitation and mineralization (Spence et al., 2014).

Generally, fractures are divided into two groups related to their mode of formation: shear fractures that form with shearing parallel to the fracture, or tension fractures that form with tension perpendicular to the fracture created (Bratton et al., 2006). Laboratory tests show that these two groups of fractures origin at distinctly different circumstances, which can help understanding the geology of the reservoir better. Shear fractures corresponds to faults and tension factures correspond to joints. Faulting is most commonly associated with tectonic events where the differential stress is high, whereas joints (or fractures) form perpendicular to bedding (Bratton et al., 2006, Spence et al., 2014).

Fractures can contribute positively to the performance and viability of a reservoir. In some fractured systems, all of the available volume to store oil in the reservoir is in the fractures. Furthermore, fractures significantly impact permeability, or even provide permeability for a porous but otherwise low-permeable reservoir (Gluyas and Swarbrick, 2012). Fractures have permeability several orders of magnitude higher than the rock matrix, yet, in some reservoirs, with a volume many orders of magnitude lower than the matrix (Bratton et al., 2006, Spence et al., 2014). The complex nature of fractured reservoirs is in direct correlation with reservoir heterogeneity.

It is estimated that carbonate reservoirs worldwide account for more than 60% of the world's oil and 40% of the world's gas reserves (Schlumberger, 2016, Singh and Mohanty, 2016). Carbonate reservoirs are often oil-wet with large variations in porosity, permeability and flow mechanisms, even within small sections of the reservoirs. This level of heterogeneity makes them challenging to characterize for oil production. Carbonate reservoirs are typically naturally fractured, with substantial variations in reservoir properties (Chilingar and Yen, 1983, Schlumberger, 2016). Based on a comprehensive study of fractured reservoirs from around the world, Allan and Sun (2003) defined four categories of fractured reservoirs:

- Type I – little or no porosity and permeability in the rock matrix. The interconnected fracture network constitutes virtually all the hydrocarbon storage as well as controlling the fluid flow
- Type II – low matrix porosity and permeability. Some hydrocarbons are stored in the rock matrix. Fractures predominantly control the fluid flow, and both fracture intensity (number of fractures per unit length) and distribution dictates production.
- Type III – high matrix porosity and low matrix permeability. The majority of hydrocarbons are stored in the rock matrix, whereas the fracture network transport fluids for production
- Type IV – high matrix porosity and permeability. Fractures in reservoirs of this category enhance permeability instead of dictating fluid flow. Effects of the fracture network are less significant on fluid flow than other categories.

Experimental results in this thesis are based on investigations of foam generation exclusively in fractures, and parallels/analogs can be drawn to 'Type I' fractured reservoirs. This will be further addressed in **Section 4** (experimental procedures).

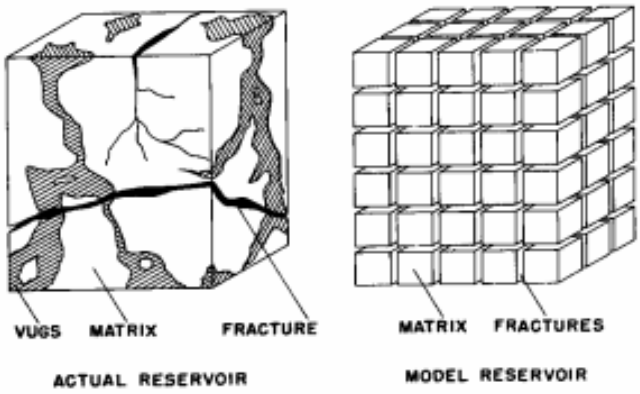

Figure 4: The obvious idealization in fractured reservoir modelling. Modelling description, characteristics and multiphase flow in fractured reservoirs is complex and challenging. Figure from (Warren and Root, 1963).

2.2 Recovery Mechanisms in Fractured Reservoirs

Fractured petroleum reservoirs are often considered to be short-lived with high flow rates, rapid production decline (tail oil production) and low ultimate recovery factors (Allan and Sun, 2003). Fluid flow in interconnected high permeable fractures, results in a limited differential pressure buildup across the reservoir. Subsequently, the large transmissibility contrast between the fracture and the rock matrix will lead to a diminished contribution of the viscous forces for oil production during e.g. a waterflood (Bear et al., 2012, Fernø, 2012). In addition to reservoir heterogeneity, poor sweep efficiency and low ultimate oil recovery is predominantly because of water flow/displacement in the fracture network only, and hence the lack of oil displacement in the individual matrix blocks.

Waterflooding as an IOR method in fractured reservoirs are usually poor. Because of its oil-wet nature, the water preferentially flows through the fractures instead of spontaneously imbibing into the matrix, leading to an early water breakthrough (Singh and Mohanty, 2016). In order to invade the rock matrix and displace oil in systems like this, the injectant fluid (water) must overcome a threshold capillary pressure. Subsequently, high connectivity through the fractures leads to a lack of differential pressure buildup across the reservoir during production (Ahmed, 2010, Spence et al., 2014). Furthermore, the injectant fluid must not channelize through high permeability regions, to prevent that low permeability regions remains unswept. Thus, the two major challenges for IOR and EOR in carbonate reservoirs are oil-wettability and reservoir heterogeneity (Firoozabadi, 2000). However, in a waterflooded water-wet fractured reservoir, capillary imbibition contributes to oil recovery. Counter-current spontaneous imbibition is the phenomenon where water in the fracture spontaneously enters a water-wet rock and oil is displaced in the opposite direction. This is a key recovery mechanism during waterflooding of fractured water-wet reservoirs (Fernø, 2012). For more details regarding capillary imbibition in fractured reservoirs, the reader can review the work of (Fernø et al., 2008), (Fernø et al., 2011) or (Hatiboglu and Babadagli, 2004).

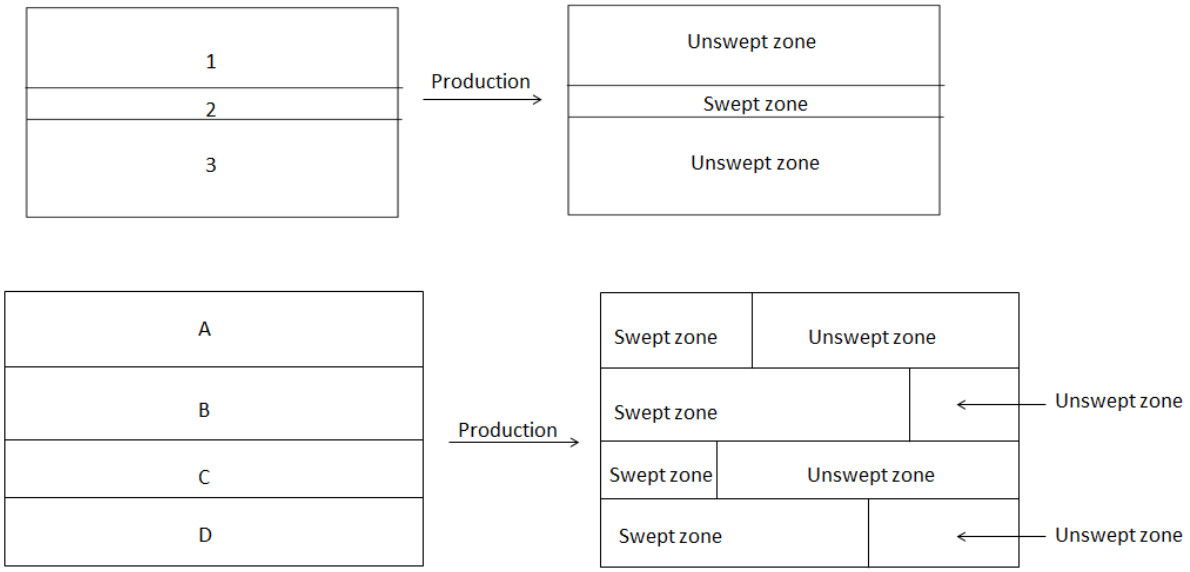

Figure 5: Two schematic examples of the effect of reservoir heterogeneity on oil production. The left hand side represents two layered reservoirs, divided into separate layers denoted as either numbers (1-3) or capital letters (A-D), with no crossflow between the layers (ie. no vertical communication). The right hand side of the figure illustrates the effect of reservoir heterogeneity in a waterflood. It is possible to reduce the fluid transmissibility in the high permeable zones (or fractures) and thus direct the flow towards the less permeable zones. Effective reduction of fluid flow in fractures can be done by introducing foam, which can smooth out permeability contrasts, and to some degree block fractures. This will be discussed in more detail in *Section 3* below.

Low ultimate oil recovery in combination with large known reserves makes carbonate reservoirs good targets for EOR efforts. However, there are problems related to low viscosity fluids such as gases or supercritical fluids used for enhanced oil recovery in fractured systems, as they may channel into the high permeable fractures, potentially leading to viscous fingering and early breakthrough into the production wells. Foam is seen as a potential to increase oil recovery by improving areal and vertical sweep, reduce viscous fingering and divert flow of gas from high permeable layers to unswept zones. The following section contains a detailed revision/review of foam fundamentals and application.

3 Theory and Application of Foam

3.1 Foam Fundamentals

3.1.1 Surfactants

Surfactants may reduce the interfacial tension between two immiscible fluids like oil and water. The molecules in the surfactants, called monomers, have a hydrophilic polar part, which attracts to water, and a hydrophobic part that has an affinity for the nonpolar media (oil) (Schramm, 1994). Hence, the surfactant molecules orientate themselves on the water/oil interface with the hydrophilic part into the water and the hydrophobic part into the nonpolar hydrocarbon chain. An increased concentration of the surfactant at the interface results in a substantial reduction in the interfacial tension between the two phases (Schramm, 2000). As interfacial tension is lowered, monomers will orientate themselves equally to either phase. Eventually, the interfacial tension breaks down, and a dispersion of water molecules into the continuous oil phase starts. In this way, aggregates of water molecules called micelles are formed in the oil phase.

The surfactant concentration is one of the main parameters that can be varied for switching a foam on or off, and for adjusting foam strength, in order to satisfy the requirements for a specific field application (Simjoo et al., 2013). In order to generate a stable foam, the surfactant concentration generally needs to exceed the critical micelle concentration (Skarestad and Skauge, 2014). The critical micelle concentration (CMC) is defined as the specific concentration at which micelle formation becomes significant (Schramm, 1994). If the surfactant concentration in an aqueous phase is increased, monomers will start to aggregate themselves into micelles, with the hydrophobic part inward and the hydrophilic part outward. A further increase in surfactant concentration beyond the critical micelle concentration would only cause an increase in the micelle concentration and not in that of monomers.

3.1.2 Foam formation, structure and characterization

Foam consists of a continuous liquid phase, called lamella, that forms a stable cellular structure that surrounds and entraps a gas phase (Exerowa and Kruglyakov, 1997, Ozbayoglu et al., 2005). Surfactants at the gas-liquid interface stabilize the lamellae by reducing the interfacial tension and consequently inhibiting the coalescence of gas bubbles into a continuous phase. Foams are considered to be either dry or wet, depending on fraction of the gas and liquid, widely recognized as foam quality in the literature. Wet foams have spherical bubbles with a large amount of liquid between them, whereas dry foam bubbles are polyhedral in shape with definite contact between lamella (Ozbayoglu et al., 2005). The polyhedral arrangement of films (shown in **Figure 6** below) which come together at equal angles is a result from the surface tensions along the lamella. Three lamellae will always come together at angles of 120^{o}, which is defined as the Plateau border (Wilson, 2013). In

addition to gas fraction and foam quality, foams are also characterized according to the texture of the bubbles. Texture is the average number of bubbles in a given volume of foam. When foam flows through pore bodies and throats in a porous media, a fine texture indicates a large amount of foam lamellae. This finer texture will in turn increase the resistance to flow, so that the transportation of lamellae through the system require a greater pressure gradient (Buchgraber et al., 2012).

In foams where the bubble sizes are smaller than the space where they are dispersed are categorized as bulk foam (Buchgraber et al., 2012). Bulk foam is further divided in ball-foam and polyhedral foam. Ball foam occurs at low gas fractions with spherical bubbles that are separated by liquid, whereas polyhedral foam bubbles are separated by a thin liquid lamella, as illustrated in **Figure 6**. Within fractures, foam appears to be in bulk in the plane and confined by the cross-sectional are of the fracture (Bikerman, 1973). In contrast, in porous media foam is confined, ie. bubble sizes are larger or in the order of characteristic pore dimensions, where the lamellae span from pore wall to pore wall (Buchgraber et al., 2012).

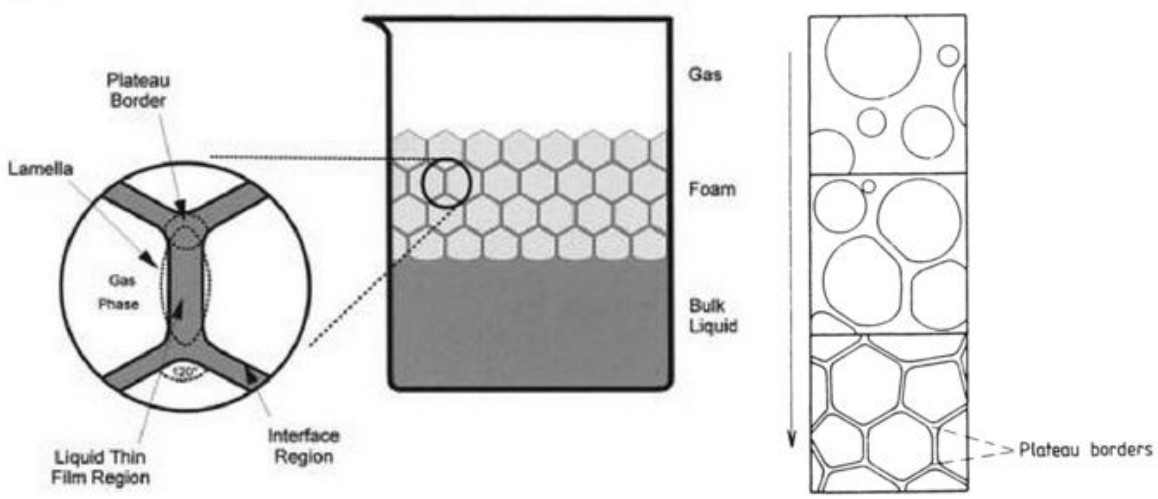

Figure 6: In the middle is a two-dimensional example of foam in a bulk container. Generally, the foam structure is contained by a bulk liquid phase on the bottom and by a second bulk phase (gas) on the upper side. Foam bubbles consist of an entrapped gas phase by a continuous liquid film, called lamella. Within the magnified region to the left, various parts of the foam structure are formulated. The gas phase is separated from the thin liquid film by lamella. When gas bubbles comes in contact with each other and form a bulk foam, individual spherical bubbles arrange themselves into a polyhedral shape, as shown to the right (Schramm, 1994).

Knowledge of foam generation criteria in porous media is key in order to better evaluate the generation of foam in fractured systems, which is the scope of this study. One objective is to investigate whether the generation criteria are similar or different in fractures as that in porous

media. The three primary mechanisms for foam generation in porous media have been identified and classified as (Ransohoff and Radke, 1988):

1) Capillary snap-off of the gas phase
2) Lamella division
3) Leave behind

Capillary snap-off takes place where a restriction in the flow space occurs, like a change in fracture aperture or pore body/throat structure. A transition in capillary pressure from high to low will lead to film thinning and eventually a snap-off of the gas phase and thereby generation of foam (Buchgraber et al., 2012, Zhang et al., 2009). This mechanism is regarded as being the most dominant in foam generation (Ransohoff and Radke, 1988). Capillary snap-off of the gas phase can occur repeatedly at the same site, generating bubbles that block the pathway of gas behind it, effectively reducing gas permeability. Bubbles may also flow but with a greater resistance compared with a continuous gas phase. Foam generation by lamellae division requires pre-generated foam and may occur where a lamella approach a branch point in the flow path where the lamella may separate into two (Ransohoff and Radke, 1988). In the leave behind mechanism a lamella is generated when two gas fronts invade a liquid-saturated region from different directions. The mechanism does not create discontinuous gas bubbles, like lamella division and snap-off, but forms a large number of lamellae that block the gas flow channels and creating dead-end pathways, to reduce the gas relative permeability. A disadvantage with foam generated by leave behind is that once it ruptures or flows out of a pore space, a second lamella cannot be generated in the same pore space unless liquid reinvade the region. According to Ransohoff and Radke (1988) this mechanism generates weaker/less stable foam than snap-off and lamella division.

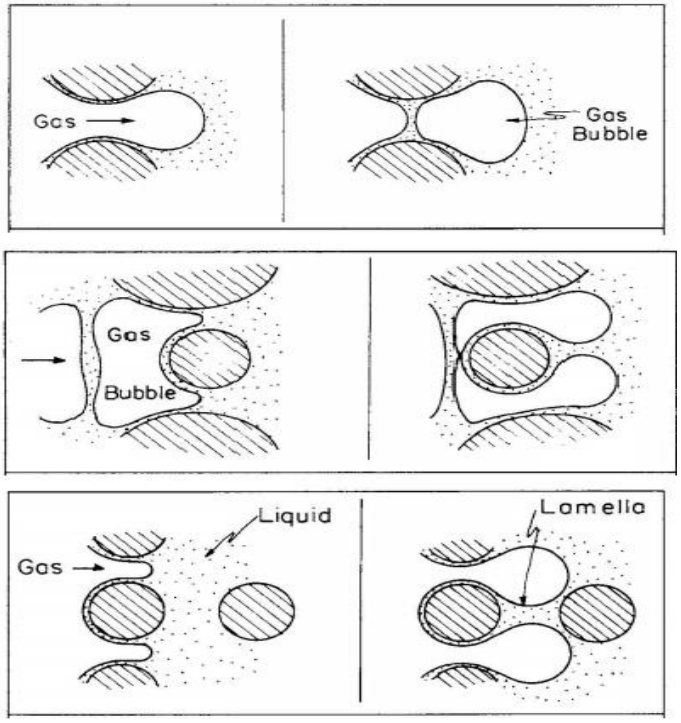

Figure 7: Schematics of the three primary mechanisms for foam generation: snap-off, lamella division and leave-behind from top to bottom, respectively. Modified from Ransohoff and Radke (1988).

The three reviewed mechanisms appear to prefer the existence of a surface wetted by the aqueous phase (Kristiansen and Holt, 1992). Yu and Wardlaw (1986) reports that aqueous foam generation by snap-off is dependent on the disconnection of the non-wetting gas phase. They showed experimentally that for surfaces having a contact angle greater than 70 degrees, generation of foam by snap-off cannot occur. However, it has been demonstrated that a medium that initially was oil-wet, but without oil, can generate foam just as effectively as a water-wet rock (Sanchez and Hazlett, 1992). This result is thought to be a consequence of surfactant absorption on the core material, a process which may alternate the surface water-wet.

Studies by Kovscek and Radke (1993) and Kovscek and Bertin (2002) has shown that abrupt steps or changes in fracture aperture can result in an accumulation of liquid upstream of the adjustment in aperture. As foam crosses from a deep to a narrow step in a fracture, foam texture is changed to more fine. Fernø et al. (2016) showed that foam was generated in fractures by snap-off, and that the bubble size was four times larger compared to that in a porous media (Barea sandstone) as a result of fewer snap-off sites in the fracture.

3.1.3 Rheology

Rheology describes flow and deformation of matter under applied forces. Rheological properties of foam such as shear stress, shear rate and viscosity strongly depend on conditions like temperature, pressure, liquid phase properties, foam quality, foam texture, foam stability and surfactant concentration (Sani et al., 2001). The complexity of the interactions and processes involved in foam production, transportation and application makes understanding foam rheology a real challenge.

If a small shear stress is applied to foam, it will elastically deform like a soft solid, characterized as a visco-elastic response (Stevenson, 2011). For an applied shear stress beyond a certain threshold known as ‘yield stress’, the foam will start to flow like a visco-plastic. This means that the foam will behave like a shear-thinning fluid, where the effective viscosity is a decreasing function of shear rate. Another rheological phenomenon arises when foams are in contact with solid walls or surfaces. If the solid wall or surface is smooth, the foam has a tendency of slipping on the wall/surface. In this particular case, the velocity of the first layers of bubbles in contact with the wall/surface and the wall/surface velocity do not equal, contrary to that of normal liquids (Stevenson, 2011). This means that along the wall, foams behave more like gases, than liquids. If not accounted for, this slippage effect can cause miscalculations in rheological measurements.

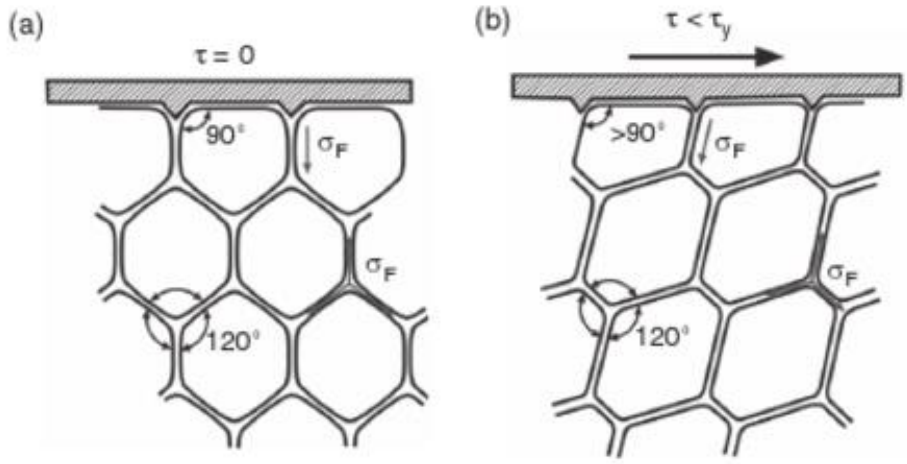

Figure 8: Schematic presentation of the elastic response of foam when subjected to shear stress τ, lower than the yield stress τ_y. a) If no external stresses act on the foam, the bubbles are symmetrical and the tensions on the foam films are balanced. b) Because of the elastic response and behavior of the foam, the tensions on the foam films are still in balance, despite bubble deformation (Stevenson, 2011).

Bubble shape and foam texture is two defining properties for the apparent viscosity in a fracture or porous media (Buchgraber et al., 2012, Hirasaki and Lawson, 1985). Foam bubble shape in porous media is governed by pore configurations, unlike the shape of bubbles in fractures where the deformation is controlled according to the interfacial tension (Pancharoen et al., 2012). The interfacial tension varies continuously according to gas fractional flow, and the flow resistance of the system is a result of bubble shape and foam viscosity. For a given foam formula the general trend is that foam mobility decreases with increasing foam quality (gas fraction) up to an upper foam-quality stability limit. This occurs because of the number of lamellae films within a given volume has increased.

3.1.4 Stability

A major concern regarding the applicability of foam as EOR is the stability of foam in contact with crude oil under harsh reservoir conditions (Sunmonu and Onyekonwu, 2013). Stability of foam in a porous media is a function of both petrophysical and foam film properties (Farajzadeh et al., 2012). The presence of oil in a porous media is generally known to be detrimental to the decrease in mobility reduction and foam stability (Buchgraber et al., 2012, Kristiansen and Holt, 1992, Suffridge et al., 1989), and impact foam flooding in terms of improved oil recovery. There are generally two mechanisms of interaction (Farajzadeh et al., 2012): 1) oil penetrates the foam film via a phenomenon called bridging and destabilize it, or 2) the lamella flow across a water film that covers the oil to create a new oil/water interface which is known as a pseudoemulsion (Farajzadeh et al., 2012). Spreading of oil on foam bubbles or lamellas will displace the original liquid film, and if the film is thinned below a critical limit for mechanical stability, the film/lamellae is likely to break (Kristiansen and Holt, 1992).

Farajzadeh et al. (2012) mentions two types of foam films that has been identified; 1) films separating the gas bubbles, and 2) the wetting films that are formed once foam bubbles contacts the rock walls. Foam stability is observed to be sensitive to rock wettability (Farajzadeh et al., 2012, Kristiansen and Holt, 1992). In oil-wet rocks, the foam films will rupture because of the dewetting of water films from the rock. Foam generation/formation in oil-wet rocks is therefore believed to be possible only if the surfactants alternate the rock wettability towards more water-wet conditions (Farajzadeh et al., 2012, Sanchez and Hazlett, 1992). Surfactant concentration may affect foam stability. Surfactants are foaming agents that lower the interfacial energy at the liquid-gas interface when it is adsorbed onto the lamella making it easier to both form and maintain a large interfacial area (Schramm, 1994). Surface viscosity increases with surfactant concentration that reduce the liquid drainage rate by gravitational forces of the lamellae (Kristiansen and Holt, 1992), hence substantiating foam stability.

Effects of capillary pressure on foam stability are widely discussed in the literature. If rock system conditions are favorable for foam generation, the foam will develop a finer texture, and thus, lower the gas mobility. The lower mobility of gas will result in an increased displacement of water. The decreased water saturation will in turn lead to a higher gas-water capillary pressure. A limiting capillary pressure has been identified, where foam becomes unstable if exceeded (Farajzadeh et al., 2012, Khatib et al., 1988, Shan and Rossen, 2004). The limiting capillary pressure depends strongly on the surfactant solution phase and rock morphology, and is found to be close to the rupture pressure of foam films that leads to bubble/foam coalescence (Farajzadeh et al., 2012). Khatib et al. (1988) showed that foam coalescence caused abrupt capillary pressure drops which made foam texture to coarsen (decrease), and thereby less stable. However, Schramm (1994) concludes that an increased surfactant concentration can retard foam coalescence by increasing the surface viscosity.

Gas diffusion through the lamellae between bubbles of different size may influence foam stability. In general, foams are more stable if bubble sizes are uniformly (small) distributed. Schramm (1994) emphasize that if there exists an imbalanced bubble size distribution, there will be pressure gradients between bubbles of different size which promote gas transfer that cause larger bubbles to grow on the expense of smaller bubbles, referred to as coarsening in the literature. A typical consequence is merging/coalescence of large bubbles and an increased average bubble size that becomes a mechanism for degeneration of foam. Even in the most ideal reservoirs small irregularities and heterogeneity in the porous media can cause finite size perturbation in bubble size, hence leading to the growth of larger bubbles that stimulates gas diffusion, adversely affecting foam stability (Farajzadeh et al., 2012). Experimental results from Kapetas et al. (2015) showed that the liquid drainage rate of lamellae increased with temperature. Additionally, they found coarsening to be accelerated at higher temperatures due to increased lamellae/film permeability, both as a result of lower surface viscosity.

3.1.5 Applicability

The hydrodynamical and rheological properties of gas-liquid foam can be utilized to make it a versatile multiphase system for a variety of process applications (Stevenson, 2011). Depending on the application in terms of oil recovery, foams can either be pregenerated at the surface, generated during downward flow in pipes/tubing or generated in-situ within the reservoir itself (either by co-injection or SAG) (Buchgraber et al., 2012).

Surfactant retention is a significant barrier to field application of surfactants in EOR on the Norwegian continental shelf (NCS) and other international fields (Skarestad and Skauge, 2014). Retention causes a drastic reduction in the surfactant concentration that reduce the technical and economic feasibility/efficiency of the chemical flooding. Its significance is a function of a range of chemically complex parameters (Kamari et al., 2015), and comes about three noteworthy mechanisms:

1) Adsorption
    - The adsorption of surfactants in porous rocks depends surfactant type and types of electrolytes in the solution and their interplay with rock characteristics such as mineralogy and morphology (Kamari et al., 2015). Surfactant monomers adsorb through hydrogen bonding and ionically bond with cationic surface sites. At critical micelle concentration and above, the supply of monomers becomes constant as well as the retention (Skarestad and Skauge, 2014).
2) Precipitation
    - Divalent cations in saline brines may cause precipitations locally inside the reservoir, resulting in unintentional chemical ion exchange between the reservoir rock and chemical compounds present in the reservoir (Maini and Novosad, 1989)
3) Phase trapping
    - Surfactant phase trapping could be due to mechanical trapping or hydrodynamic trapping. The mechanisms are complex and depend on the multiphase flow conditions. For detailed information the reader may review literature by (Glover et al., 1979) and (Sheng, 2013).

3.2 Foam EOR

The decline in discoveries of new petroleum reserves combined with the global increase in demand for energy is highlighting the oil and gas industry's need for enhanced oil recovery techniques (Belhaij et al., 2014). Gas injection for improved oil recovery is a commonly implemented method in both mature and new fields. Despite favorable characteristics in gas-oil displacements, like oil swelling and reduced density difference between gas and oil (in CO_2 flooding), disadvantages such as viscous fingering, gravity override and reservoir heterogeneity are often reported and lead to poor sweep efficiency (Belhaij et al., 2014).

Due to the low density, gas is expected to rise to the top of the reservoir and override the oil zone. Because of the high gas mobility (low viscosity), viscous instabilities in the reservoir are likely. These properties of the injected gas promotes gravity override and heterogeneity by forming high mobility gas channels (Shan and Rossen, 2004). It is the competition between the horizontal pressure gradient and the density difference and gravity that results in gravity override (Shi and Rossen, 1998). By introducing foam to the reservoir, one can obtain improved volumetric sweep efficiency through the reduction of gas mobility and effects of reservoir heterogeneity (Schramm, 1994).

Foam displayed promising flow characteristics once introduced as EOR, including favorable mobility ratio, selective blocking of thief zones and flow diversion to lower permeability regions (Belhaij et al., 2014, Bernard et al., 1980, Farajzadeh et al., 2010). Foam is useful to mitigate an unfavorable mobility ratio between the displacing and displaced reservoir fluids to control and redirect the injected aqueous phase to unswept reservoir zones. The aim is to reduce fluid mobility in fractures or "thief zones" by injecting foam that aids matrix-fracture transfer of surfactant solution into the matrix blocks. Large, thick and highly conductive fractures that act like thief zones are regarded as targets for blocking fluid flow, in order to divert flow to smaller fractures and their adjacent matrix blocks. Foam flow and foam generation in fractures is not fully understood, and more studies needs to be quantified and validated to improve simulation models for such applications (Buchgraber et al., 2012).

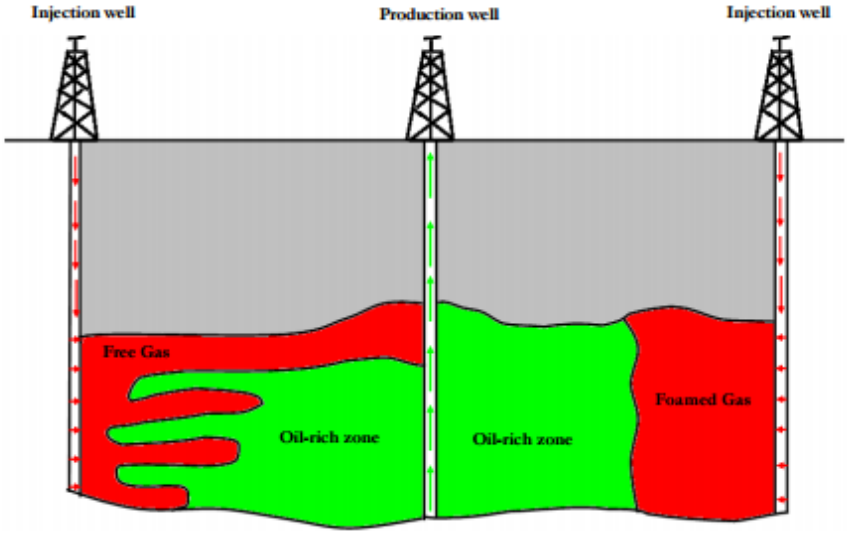

Figure 9: Schematic of a comparison between a regular gasflood and a foam assisted gasflood. Channeling of gas in high permeable layers results in a large volume of bypassed oil (thief-zones). Foam is introduced to mitigate the reservoir heterogeneities and front instabilities, hence improving the sweep efficiency (Farajzadeh et al., 2012) .

3.2.1 Mobility control

A foam intended for mobility control is one where the mobility of the foam is reduced to an approximate level that is comparable to the oil being displaced, with the aim to suppress channeling and fingering (Enick and Olsen, 2012). Studies by Kovscek et al. (1997) and Persoff et al. (1991) has shown that foam as a pseudo-phase may exhibit very low mobility in both porous media and fractures. This reduction in mobility is recognized as the mobility reduction factor (MRF) (Buchgraber et al., 2012). The mobility reduction factor is defined as the ratio of pressure drops across a porous medium or fracture, between the foam pseudo-phase and sing-phase gas flow:

$$MRF = \frac{\Delta p_f}{\Delta p_g} \tag{6}$$

High values of MRF indicate a more finely textured, hence stronger, foam, and vice versa for low values of MRF (Zhang et al., 2009). Foam reduce the flow of gas but does not reduce the relative permeability of the liquid phase as this remains continuous. Experimental studies by Casteel and Djabbarah (1988) has indicated that foam can reduce gas mobility more effectively in high permeable layers compared to that of Newtonian fluids, like water. Additionally, foam diverted the flow of the injected gas to the low permeable layer, and reduced viscous fingering and front instabilities often associated with gas injection into heterogeneous reservoirs.

Foam reduces the mobility ratio in two ways:

1) A flow of bubbles will encounter a significant drag force. The interfacial area of a flowing bubble is constantly adjusted by viscous and capillary forces as the bubble flow over pore walls and fracture surfaces, in addition to the presence of constrictions in the flow space (Hirasaki and Lawson, 1985).
2) Gas mobility in the presence of foam depends greatly on foam bubble size (Kovscek and Bertin, 2002). Generally, a fraction of the foamed-gas phase is stationary (Kovscek and Radke, 1993). Trapped gas restrict the gas flow and reduce the relative permeability of the gas phase accordingly (Kovscek and Radke, 1993). Consequently, the better the blocking ability of the foam, the greater the reduction in gas mobility.

3.2.2 Improved sweep efficiency

In order to improve sweep efficiency for conformance control, foams are designed to selectively generate strong and low mobile foam in high permeability zones and thief-zones. These foams are widely referred to as blocking and diverting foams, or injection profile improvement foams (Enick and Olsen, 2012).

Gases used in gas-flooding, such as nitrogen, carbon-dioxide, flue gas and hydrocarbon gas, are normally less viscous and less dense compared with both water and crude oil. This often results in gas channeling through the higher permeable zones and potential gravity override in heterogeneous reservoirs (Singh and Mohanty, 2016, Sunmonu and Onyekonwu, 2013). Some of the most reported problems associated with gas injection projects are the inefficient utilization of the gas due to poor volumetric sweep efficiency as a consequence of viscous instabilities like channeling or fingering and gravity segregation (Sunmonu and Onyekonwu, 2013). Foam is seen as a potential solution to mitigate this poor sweep efficiency.

In fractured reservoirs, foam acts as a blocking agent which slows and redirects the transport of the aqueous phase in high transmissibility fractures. Fluids always seek to flow the path of least resistance. The permeability contrast between fractures and matrix prohibits the performance and efficiency of common IOR techniques and can affect the oil recovery adversely (Farajzadeh et al., 2010). By increasing the saturation of the foam/surfactant solution in the matrix blocks (foam injection), and thereby aiding the imbibition of the system, the remaining oil will be drained (Buchgraber et al., 2012).

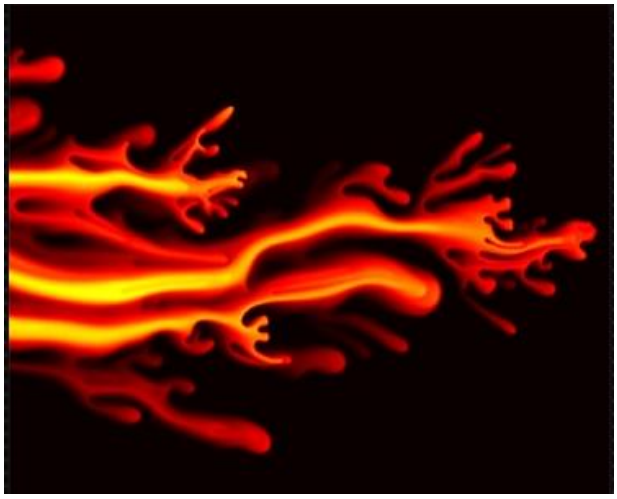

Figure 10: Illustration of viscous fingering due to an unfavorable mobility ratio. The figure shows an unstable displacement process of a more viscous fluid (dark) by a less viscous fluid (light). Figure from (Jha, 2011)

3.3 Field Reports/Literature Survey

Despite the fact that active research on foam as EOR has been on the rise the last decades, industry experience of foam enhanced oil recovery is still limited as relatively few field or pilot applications have been developed (Kapetas et al., 2015). The physics of foam behavior and foam flow both in porous media and fractures are very complex, and the mechanisms of foam EOR are still under investigation. Thus, development of predictive simulations models of foam processes is a big challenge (Masoudi et al., 2015).

Due date, the Snorre FAWAG (foam assisted water-alternating gas injection) project on the NCS is the world's biggest application of foam in the oil industry (Skauge et al., 2002). Two major problems in oil production on this field (sandstone reservoir with faults) was early gas breakthrough in some production wells and high gas production in terms of gas-oil ratio (GOR). Foam was injected both as a slug in front of a chasing gas phase and in combination with gas (co-injection). Co-injection provided the strongest foam, concluded from pressure build-up data and tracer analysis. Subsequently, injectivity was reduced immediately after surfactant injection indicating foam generation. Production well treatments experienced varying degree of success on foam duration/stability, where effects of foam lasted from only weeks to more than 6 months. The results from the field implementation were in overall positive: gas breakthrough was delayed and the GOR was considerably lower than prior to the foam treatment. The total expenses for the FAWAG project on one part of the field was estimated to 1M USD, and the value of the additional oil recovery was estimated to be ~25-40M USD at the current (2002) oil price during the project execution.

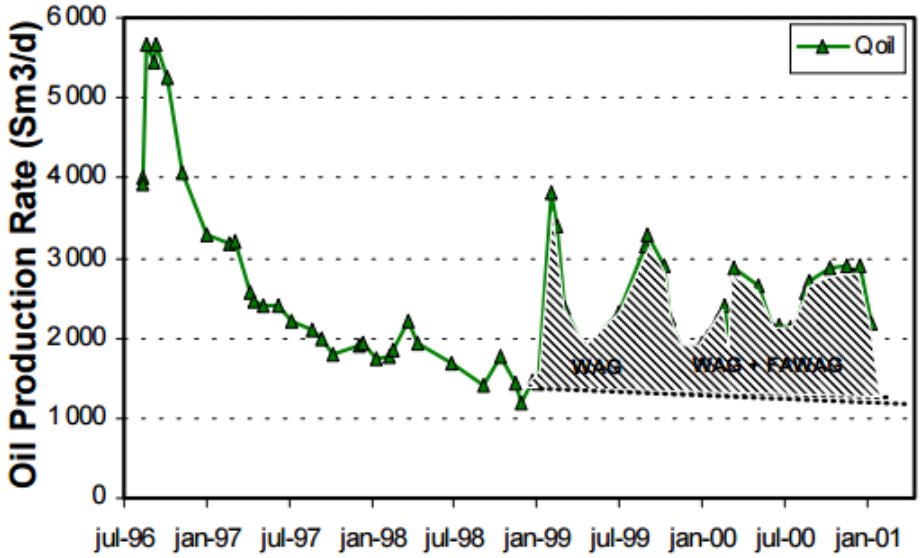

Figure 11: Production history from a well included in the FAWAG project on the Snorre field. The effects of WAG and FAWAG are shown as the dashed area in terms of increased oil production. The dotted linear line beneath the increased oil production is the predicted/simulated oil production if no EOR mechanisms were implemented (Skauge et al., 2002).

The first application of foam in the North Sea was to reduce the inflow of gas into a production well at the Oseberg field, where the recovery mechanism is gas injection (Surguchev and Hanssen, 1996). Foam was generated by a slug-injection of gas and surfactant dissolved in the brine. Results showed a reduction of GOR with about 50% compared to pre-foam production tests. The foam treatment effectively reduced inflow of gas during the whole test of 6 months. Based on the positive results, another well treatment was carried out. In this case GOR was reduced by approximately 30% for a two-week period. Friedmann et al. (1994) reports of issues regarding foam propagation and in-depth stimulation. In a pilot test observation wells were drilled at a certain distance from the injection wells. The first observation well (12m) observed foam at expected/predicted time. The second observation well however (20m), arrived several months after predicted arrival. Foam's lack of propagation into the reservoir compared to surfactant propagation is mentioned as a possible explanation. This is one of the oil industry's biggest concerns regarding foam field scale EOR implementation.

Another field test was run in Texas (US) to reduce CO_2 cycling. The effectiveness of the foam gradually decreased with time (in-depth) due to the foam drying out and the surfactant bank moving away from the wellbore. Foam was regenerated to its original effectiveness by injecting small slugs of water to rehydrate the foam, extending the life of the foam by a factor of two (Henry et al., 1996). The field test was a technical success. However, it was rated uneconomical due to the low cost of recycling CO_2 at the current (1996) gas price. In order to make the implementation more economical, better placement of the surfactant slugs was suggested along with larger volume of surfactant injected to better affect areal sweep

efficiency. An advantage with foam treatments is that they are not permanently affecting the reservoir. Large volumes of water can be used to flush the reservoir clean of foam and surfactant, except the surfactant lost to retention.

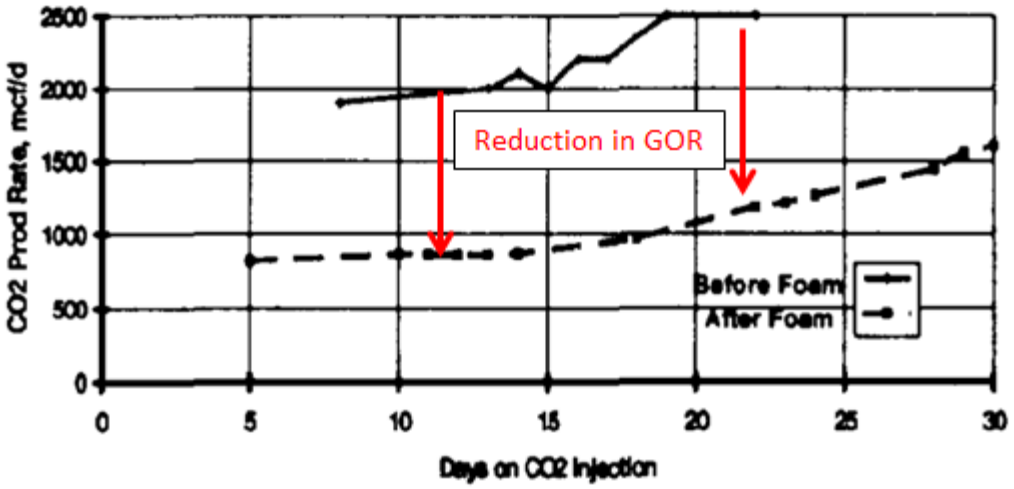

Figure 12: CO_2 production rates from a well involved in the foam treatment before (solid line) and after (dashed line) foam generation. The effects of foam are observed as the reduced gas inflow to the production well. Modified from (Henry et al., 1996).

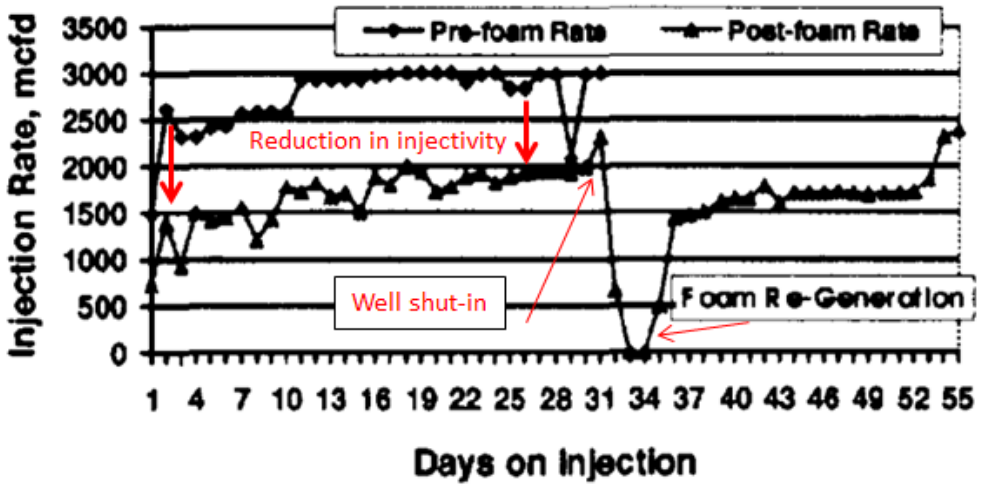

Figure 13: CO_2 injection rate at a well involved in the foam treatment. The circular point plot is the pre-foam rate, while the triangular point plot is the post-foam rate. After foam injection has commenced the injection rate decrease because the foam blocks fluid flow. The increase in injection rate indicates decreasing foam effectiveness. The effect of rehydration of the foam is observed as the stable plateau of the CO_2 injection rate after well shut-in. Modified from (Henry et al., 1996).

Technical feasibility of surfactant floods on a field scale has to some degree been established. However, the economic feasibility is a complex function of factors such as oil price, surfactant consumption and surfactant cost (Romsted, 2014). Whether the implementation environment is onshore of offshore also plays an important role in the economics of a potential project. If the project under consideration is an offshore environment the cost

significantly increases. Large shipments and the storage of extensive volumes of chemicals result in additional equipment needed. Generally, it is the surfactant itself which is the single most expensive item in the total cost of an EOR process involving surfactants. The surfactant expense is a combination of the initial investment in purchasing the surfactants along with the cost of replacing surfactant lost due to retention. Unfortunately, from a technical researcher's point of view, the contemporary low oil price makes oil companies reluctant on further research and potential field implementation of foam EOR. Paradoxically, the decline in discoveries of new petroleum reserves is not pushing the companies in the oil industry towards improved and necessary research on this topic.

Chapter II - Experimental Procedures

Chapter II presents an overview of the experimental part of the thesis, including rock material, fluids, experimental setups and procedures.

4 Fractured Systems and Fluids

A detailed description of the three fractured systems used in this thesis to study in-situ foam generation during co-injection of gas and surfactant will be presented in this section. **Table 1** gives an overview of experiments conducted. Experiments were performed both at the Department of Physics and Technology (IFT), University of Bergen (UiB) and at Haukeland University Hospital (HUH).

Table 1: Overview of number of experiments performed on the different fractured systems.

Fractured system	Number of completed experiments	Number of incomplete experiments	Total experiments performed
Fractured block system (m^{-1} scale)	4	5	9
Fractured marble core (2 inches)	14	7	21
Fractured marble core (4 inches)	2	1	3

18 out of 20 experiments reported in this thesis were conducted in collaboration with fellow master student Sigbjørn Aasheim Johansen. A detailed overview of the experiments conducted is given in **Appendix B**. Some experiments had to be aborted as a result of one or more defects related to the experimental setup, leading to invalid measurements. Although the data from these experiments will not be presented for scientific discussion in this thesis, they provided valuable knowledge of how to improve and streamline the experimental setup together with familiarizing with the constraints of the setups used and evaluating system sensitivities. Some examples of aborted experiments include too significant effects of gas compressibility, and backflow from the core due to low contrast in drive pressure delivered from the mass flow controller compared to system pressure.

4.1 Fractured Block System

An experimental setup was used in order to visualize foam flow and propagation, shown in **Figure 14** below. The construction of the system is detailed further in (Fernø et al., 2016). **Table 2** lists properties of the fractured block system. The block system was used to relate pressure to bubble size distribution, foam texture and foam flow, in addition to figure as an upscaling from core scale.

Table 2: Fractured block network properties. Data obtained by (Fernø et al., 2016).

Length [cm]	Height [cm]	Width [cm]	Fracture porosity [%]	Permeability [D]
31.20	31.20	1.00	7.0	3.64

Foam was generated by co-injection of gas (nitrogen) and surfactant solution. The fracture network consisted mainly of narrow fractures and vugular open fractures with open space varying from 0.4- and 2.2-cm aperture (discussed more detailed in **Section 8.3**). The vugs were used to 1) observe the advancement of the foam front during co-injection, and 2) observe changes in bubble texture with varying injection conditions. Six sectors were defined and used as reference points when evaluating foam generation and propagation.

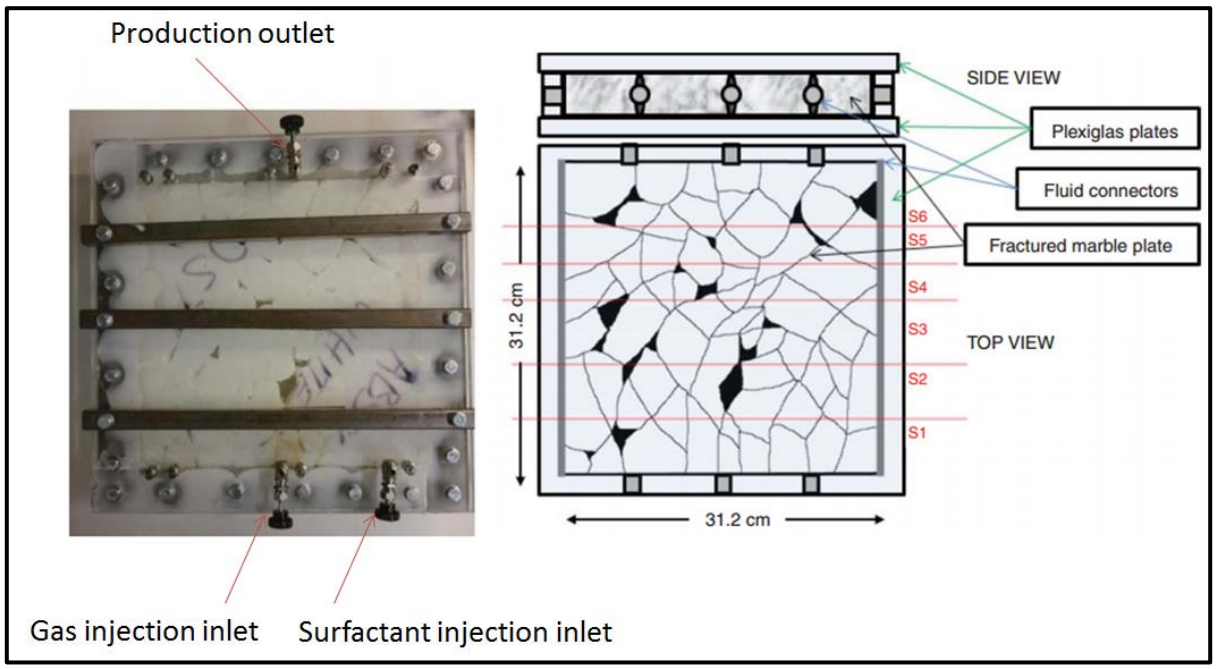

Figure 14: Image (left) and schematic (right) of the fractured block system between two Plexiglas plates. Note that the three aluminum bars are not included in the schematic for visualization purposes. During the experiments gas and surfactant was coinjected in separate injection points/inlets and produced from a single outlet point, shown on the left. The schematic on the right defines six sectors that are used as reference when evaluating local sweep efficiency. Figure modified from (Fernø et al., 2016).

4.2 Fractured Marble Cores

Cylindrical marble cores were drilled and cut from a large rectangular marble block. The homogeneous marble block is impermeable and without porosity (characterized as Type I fractures, cf. **Section 2.1**) was ideal to study foam generation in fractures after the fracturing process. About 30 cores were drilled, and one arbitrary 2-inch core and three 4-inch cores were chosen for experimental use. Previous work with foam generation in fractured cores used a saw to generate fractures (Hjartnes, 2015, Horjen, 2015, Lie, 2013), where the cores were cut longitudinally and a plastic spacer (on the millimeter scale) maintained a smooth, open fracture with a constant aperture. To generate more realistic and rough-walled fractures a new methodology was developed in this thesis based on the Brazilian test principle. A

crushing tool was made and designed with support and modification from the mechanical workshop at the department. The crushing tool was thoroughly tested using cores with varying length and diameter of different rocks, including limestone, sandstone, chalk and marble. This initial testing was a key to provide knowledge of which core length that produced the most complex and realistic fractures, and which applied load that caused the rock material to break/fracture sophistically. The created fractures can be characterized as shear fractures, cf. **Section 2.1**.

Figure 15: Drilling of marble core material. 1) Drilling machine with 2-inch bit. 2) The rectangular marble block after the drilling procedure was finished. The red arrow to the left points at the hole from 4-inch bit, whereas the arrow to the right points at a hole from the 2-inch bit. 3) The table where core material were stored during the drilling procedure

Core preparation consisted of two main steps: 1) generation of fractures with new methodology and 2) core reassembling and wrapping. In "**the fracture generation process**", the cores were placed in the new crushing tool and a vertical stress/load was applied until the core fractured. After the cores were fractured one could observe fine loose rock grains/particles and smaller pieces of rock that used to fill the space prior to the created fractures. Only the larger rock parts were targeted for reassembling. The "**core reassembling**" consisted of carefully puzzling the fractured rock pieces together into a single system and

tightly wrapping it in aluminum foil. Shrinking sleeve was used to improve stability and wrapping. To ensure that flow from the inlet end-piece went through the core and not around it (between the core and rubber sleeve in the core holder) aluminum tape was used to link/connect the end-pieces at both inlet and outlet to the core itself, shown in **Figure 17** below.

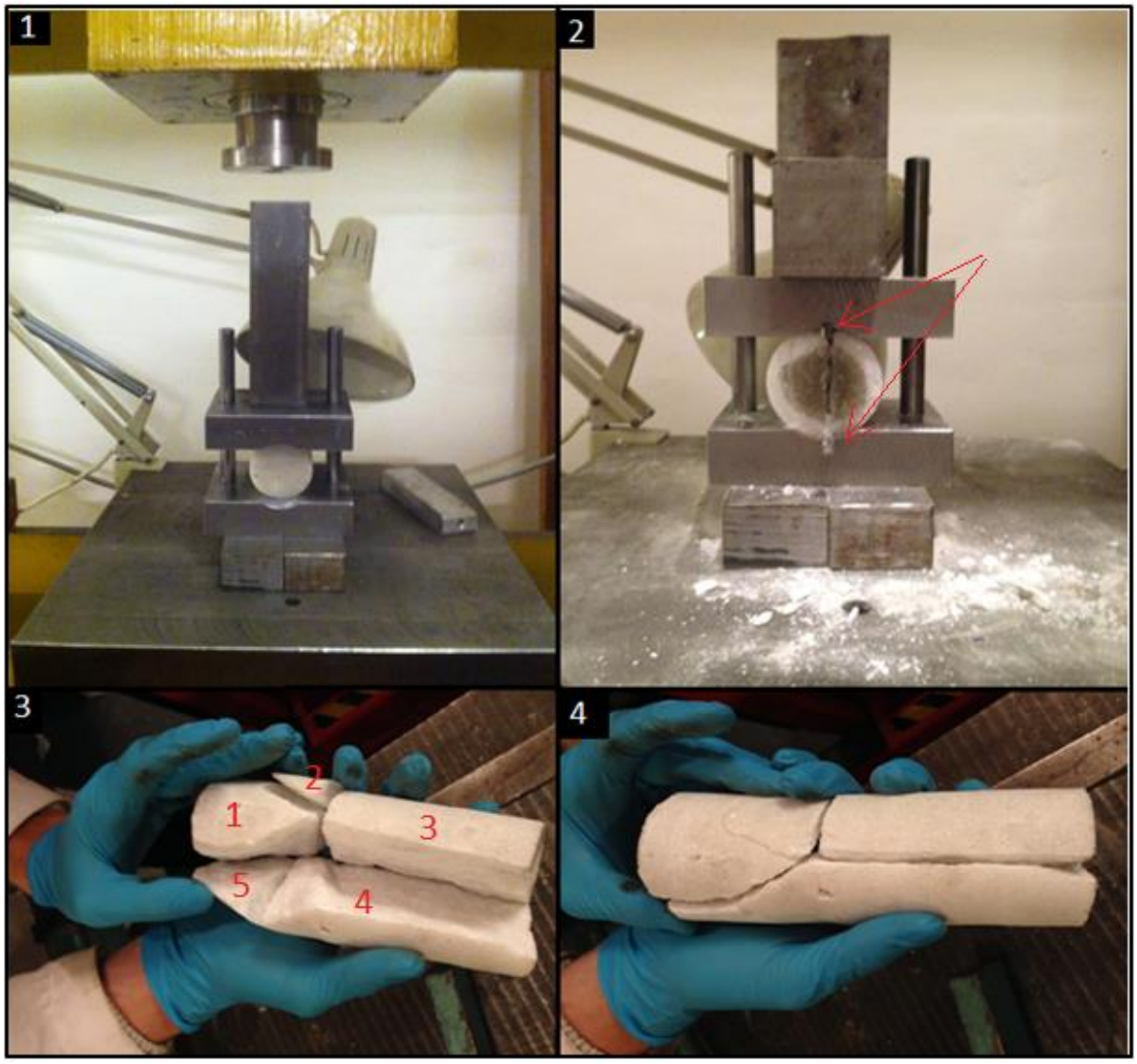

Figure 16: Crushing/Fracture generation procedure. 1) Crushing tool with core material. Vertical stress was applied from a hydraulic press. 2) Compressive forces (load) was generated from the hydraulic press until the core fractured. The arrows points at two identical elongated rails that provided the contact area between the core and the fracture tool. 3) A typical result from a core fracturing. Loose rock particles were removed and only the larger pieces were considered for reassembling (5 pieces in this picture). 4) The large pieces were reassembled by hand and held thightly prior to wrapping.

Figure 17: Wrapping procedure. 1) A – fractured core thightly wrapped in aluminum foil. B – shrinking sleeve. C – heating pistol. 2) Aluminium foil was used to wrap the core and keep the pieces in place. 3) Shrinking sleeve is used as additional wrapping stability. A heating pistol was used to shrink the sleeve so that it would attach to the aluminum wrapped core. It was important to evenly distribute heat to the entire shrinking sleeve to prevent it from folding or any other shrinking irregularities. 4) Inlet and outlet endpieces of the coreholder was connected to the prepared cored with aluminum tape before placing the core into the core holder to ensure that injected fluids flow through the core and not around it (on the outside). The red arrow points at the open space between an endpiece and the core that potentially could cause fluid flow around the core if not connected with aluminum tape.

Additional steps in core preparation were taken for the 4-inch. The drilled 4-inch core material was too short to fill the entire length of the rubber sleeve of the 4-inch core holder. Several 4-inch space fillings in polyoxymethylen (POM) was therefore made by the mechanical workshop. The space fillings were designed with an identical flow pattern as the inlet and outlet end-pieces. Additionally, the fracturing process of the 4-inch core material originated such a significant amount of loose rock particles and smaller rock pieces that the core diameter after reassembling was reduced by ~0.76 cm. To avoid accumulation of fluids in small pockets at the start and end of the core, duct-tape was tightly wrapped at both ends of the core to prevent the rubber sleeve of the core holder to bend considerably at these key areas.

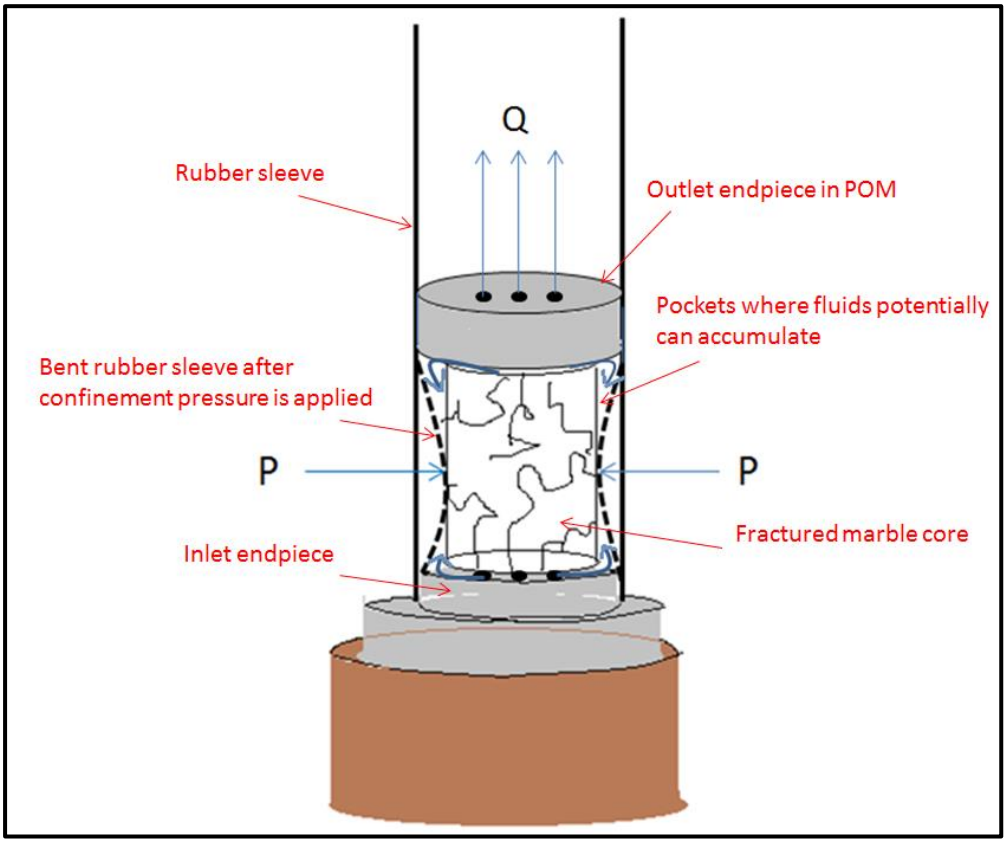

Figure 18: Schematic illustration of a potential problem of the abrupt transition in width between the 4-inch inlet endpiece, 4-inch POM space fill and the ~3.7-inch fractured core material. P abbreviates pressure [Pa] and Q abbreviates fluid flow [m^3/s]. To compensate for the difference in width duct tape was wrapped in several rounds until the transition was insignificant/negliable. Note that the transition is exaggerated for visualization purposes.

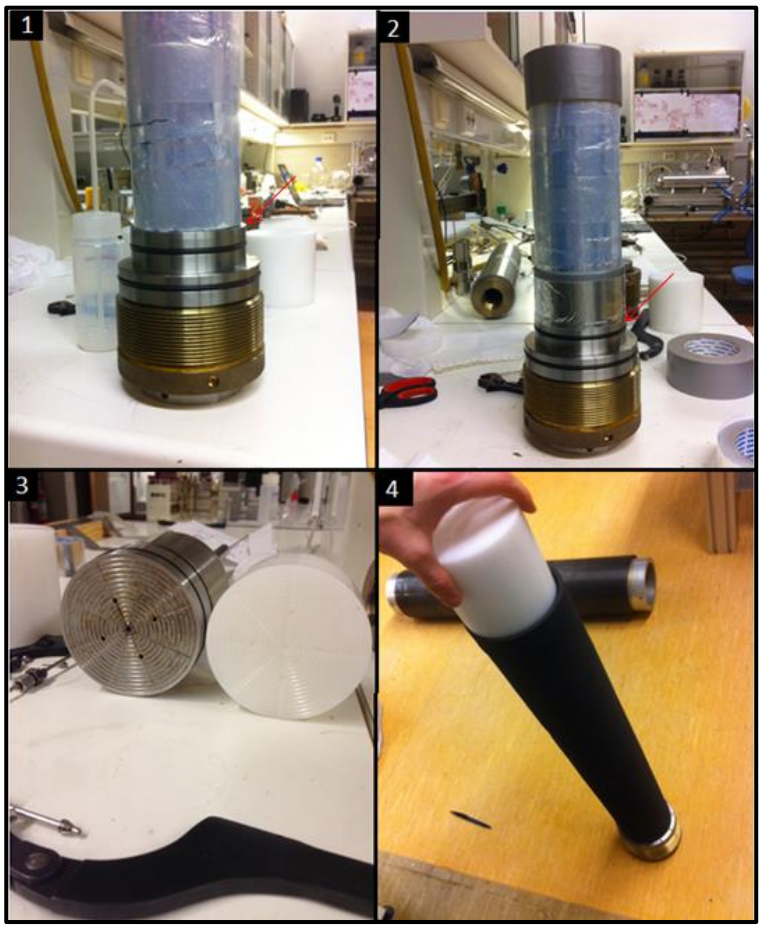

Figure 19: Preparation of 4-inch core material. 1) After similar wrapping procedure as in *Figure 17* the core's width at inlet and outlet had to be increased with duck tape. The red arrow points at the difference in diameter between the core material and the core holder's inlet endpiece. It is clear that the difference could lead to fluid flow around the core itself. 2) After wrapping several rounds of duct-tape around the core at inlet and outlet, aluminum tape was used to cnnect the core to the inlet endpiece. The red arrow shows the space that is now filled using duct-tape and aluminum tape. 3) The endpieces in POM used for space filling due to lack of 4-inch core material were made identical to the endpices of the core holder. 4) The entire open space of the rubber sleeve was filled by stacking POM endpieces. The core holder's outlet endpiece was attached with force to the last POM endpiece in the sleeve. After the sleeve was succsessfully filled with core material, POM endpieces and core holder endpieces, the entire sleeve, with attached endpieces, was placed in the core holder (laying at the floor in the background).

Fractured marble cores with different diameters (2- and 4-inch) were used to study foam generation by co-injection of gas and surfactant solution. **Table 3** below gives an overview of core properties. Note that measured core properties of the 4-inch core is scarce because the main focus of this work is the 2-inch core. The total length of the 4-inch core was 26.6 cm, and consisted of 3 stacked cores (2 x 8.8 cm and 1 x 9.0 cm). The fracture volume was calculated using the saturation method: The core was vacuumed and weighed dry before it was saturated with synthetic brine and weighed again. The density of the synthetic brine was assumed equal to that of distilled water.

$$FV = \frac{m_{saturated} - m_{dry}}{\rho_{brine}} \quad (7)$$

where FV [ml] is fracture volume, $m_{saturated}$ [g] is the total mass of the saturated core, m_{dry} [g] is the total mass of the dry core and ρ_{brine} [g/ml] is the density of the brine that saturates the core. Fracture porosity was calculated as the ratio between the fracture volume and bulk volume. Note that these properties will not be included in further discussion. However, they are essential parameters when quantifying data. Recommendations and suggestions for future work include quantitative analysis, for instance oil recovery by foam. This will be further discussed in 'Future Work' in **Section 12**.

Table 3: Geometric properties measured for the various marble cores.

Core ID	Length [cm] ± 0.02	Diameter [cm] ± 0.02	Bulk volume [cm^3][1]	Fracture porosity [%][2]	Fracture volume [ml][3]	Permeability [D][4]
2i-1	14.90	5.08	301.99 ± 1.02	5.95 ± 0.02	17.97 ± $2.40*10^{-3}$	3.9436 ± 0.11
4i-3S	26.60	9.39	-	-	-	-

[1] Uncertainties are calculated based on **Equation A3, Appendix A**
[2] Uncertainties are calculated based on **Equation A3, Appendix A**
[3] Uncertainties are calculated based on **Equation A3, Appendix A**
[4] Uncertainties are calculated based on **Equation A3, Appendix A**

4.3 Fluids

Fluid compositions and properties used in this thesis to experimentally study foam generation in fractured systems are listed in **Table 4**.

Table 4: Fluid overview at experimental conditions. All values are obtained from

Fluid	Composition	Density [g/cm^3]	Viscosity [cP]	Conditions	
				Temperature [^{o}C]	Pressure [bar]
Distilled water	100 % H_2O	0,997	0,890	25,0	1,0
Synthethic brine	H_2O 1 wt.% NaCl	-	-	25,0	1,0
Huntsman Surfonic L24-22[5]	Distilled water 1 wt.% NaCl 1 wt.% L24-22	-	-	25,0	1,0
Petrostep C1	Distilled water 1 wt.% NaCl 1 wt.% C1	-	-	25,0	1,0
Nitrogen	> 99,999% N_2	-	-	25,0	1,0
Compressed Air	100% dry air	-	-	25,0	1,0

L24-22 contained fatty (or long-chain) alcohols C_{12}-C_{14} and is a non-ionic surfactant. The surfactant was solid phase (wax-like) and had to be mixed in the synthetic brine for several hours in order to be completely dissolved. Petrostep C1 was in liquid phase, and was relatively viscous. Co-injections with Petrostep C1 as surfactant did not require as extensive mixing as L24-22. 1 wt.% of surfactant was used in all experiments. Looking into how concentration of surfactant affected foam stability was beyond the scope of this thesis.

[5] From this point on, this surfactant will be referred to as L24-22 in the text.

5 Foam Generation and Visual Inspection of Foam Flow in Fractured Block System

In-situ foam generation by co-injection of gas and surfactant solution and visualization of foam flow/propagation were studied at standard condition temperature and pressure (25 ^{o}C, 1 bar). The experimental setup was inspired from (Fernø et al., 2016) and built together with fellow master student Sigbjørn Aasheim Johansen.

5.1 Setup and Equipment

A schematic illustration of the experimental setup is shown in **Figure 20**. All experiments on the fractured block system were performed using this setup. Vertical experiments were conducted by tilting the fracture network 90 degrees.

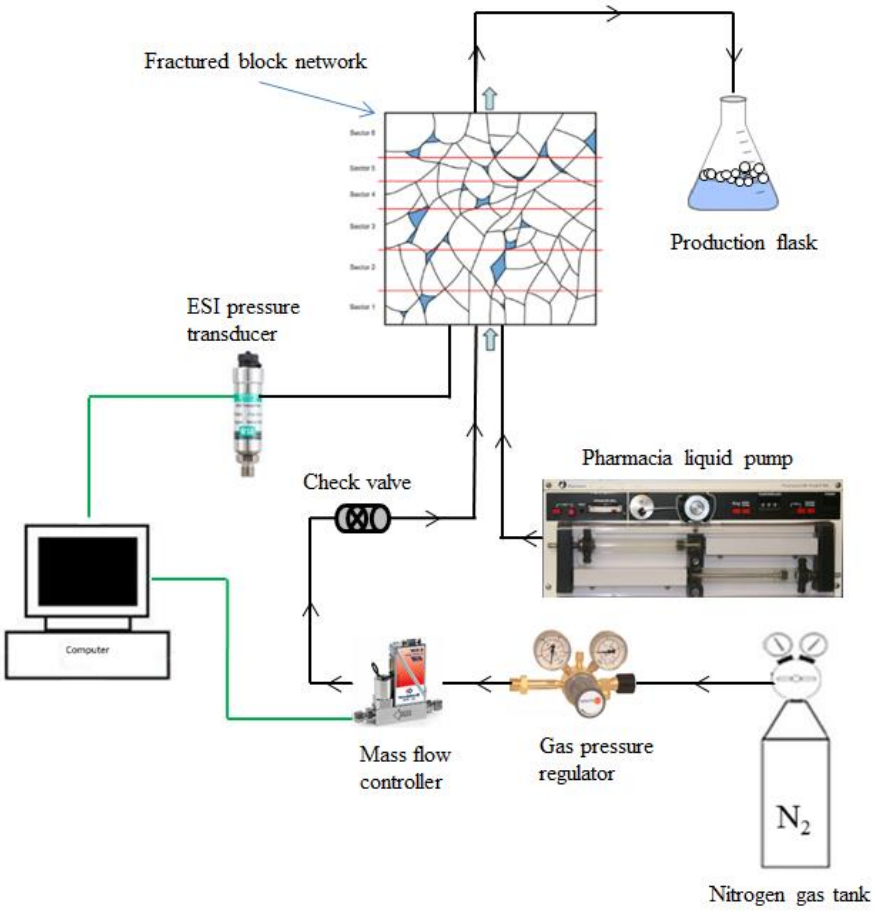

Figure 20: An illustration of the experimental setup used for foam generation by co-injection of nitrogen gas and surfactant solution in the fractured block network. The black lines are tubing, and the black arrows indicate fluid flow direction. The green lines represent data cables that connect the pressure transducer and mass flow controller to the computer. The computer logs pressure and delivers digital information and commands to the mass flow controller.

5.1.1 List of Equipment

- Fractured block network
- Pharmacia LKB P-500 pump
- ESI Digital USB Pressure Transducers, range 0-10 bar (±0,05 % FS)
- Computer for pressure logging and command delivery to mass flow controller
- 1/16" tubing and Swagelok fittings
- Nitrogen tank (P_{max} = 200 bar)
- Bronkhorst EL-FLOW® Mass Flow Controller
- Swagelok Gas Pressure Regulator, Pressure-Reducing/Spring-Loaded
- Swagelok Fluid Flow Check Valve
- 1 liter transparent production flask

5.1.2 Detailed Component Description

The fractured block network was placed horizontally on a custom-made rack. This provided observation points on both ends of the fracture network. Both foam generation and foam flow/propagation was easy to observe. The six defined sectors of the fracture network was used as reference when evaluating sweep efficiency and foam flow/propagation. Each sector had a known number of bigger open vugs and fractures. These were regularly checked during co-injection tests and compared with fractures and open vugs within their own sector, and the other sectors. The left- and right-hand side of the fractured network was sealed with epoxy resin and remained no-flow boundaries. The Pharmacia pump with two synchronized syringes was used for continuous injection of liquid surfactant solution. The injection rate was varied with gas fraction accordingly. An ESI USB pressure transducer was connected directly to the fracture network on the inlet side next to the injection ports used for co-injection, and pressure was logged on the computer. Outlet pressure in the production flask was atmospheric. The gas pressure regulator was used to regulate the high pressure coming from the nitrogen gas tank to a lower delivery pressure that was sent to the mass flow controller. Additionally a check valve was connected to the tubing from the mass flow controller in case of liquid backflow from the fracture network.

5.2 Laboratory Procedures

Co-injection tests using the fractured block network was performed in collaboration with fellow master student Sigbjørn Aasheim Johansen. Before every co-injection commenced, the fracture network was flushed and fully saturated with brine. Nitrogen gas injection rates were controlled with a mass flow controller, whereas injection rates of the aqueous surfactant solution was regulated with the Pharmacia pump. Pressure was logged on the computer and injection rates were varied with gas fraction accordingly. Produced fluids accumulated in an open production flask. Foam was visually observed both in the system and in the production flask.

6 Foam Generation in Fractured Marble Cores

Foam generation by co-injection of gas and surfactant solution into the fractured marble cores were studied at standard temperature (25 ^{o}C) and varying pressures. The foam was not pregenerated before injection through the fractured system, and reported results describe in-situ foam generation only. The experimental steup was built together with fellow master student Sigbjørn Aasheim Johansen. Note that the experiments performed on the 4-inch core used an identical experimental setup (improved version) as presented in this section.

6.1 Setup and Equipment

A schematic illustration of the experimental setup is shown in **Figure 21**. All co-injections in the fractured cores were performed using this setup. However, two versions of the setup were used. The fractured cores are described in detail in **Section 4**. Results from initial tests on the 2-inch core were difficult to discuss due to large fluctuations in the recorded pressures. To reduce pressure fluctuations from gas compressibility effects, backpressure was installed at the outlet to elevate the system pressure. This provided a better control of the foam quality and evidently reduced the fluctuations in differential pressure. Without the installed backpressure, produced fluids accumulated in an open production flask. With backpressure, produced fluids accumulated in a closed production tank with elevated pressure. The backpressure was maintained using compressed air connected at the top of the production tank at the outlet. The production tank had a large volume compared with the system volume so that the increased pressure from the produced fluids into the bottom of the tank had a negligible effect on the experiment. The pressure in the production tank was logged on the computer with the use of an ESI USB pressure transducer.

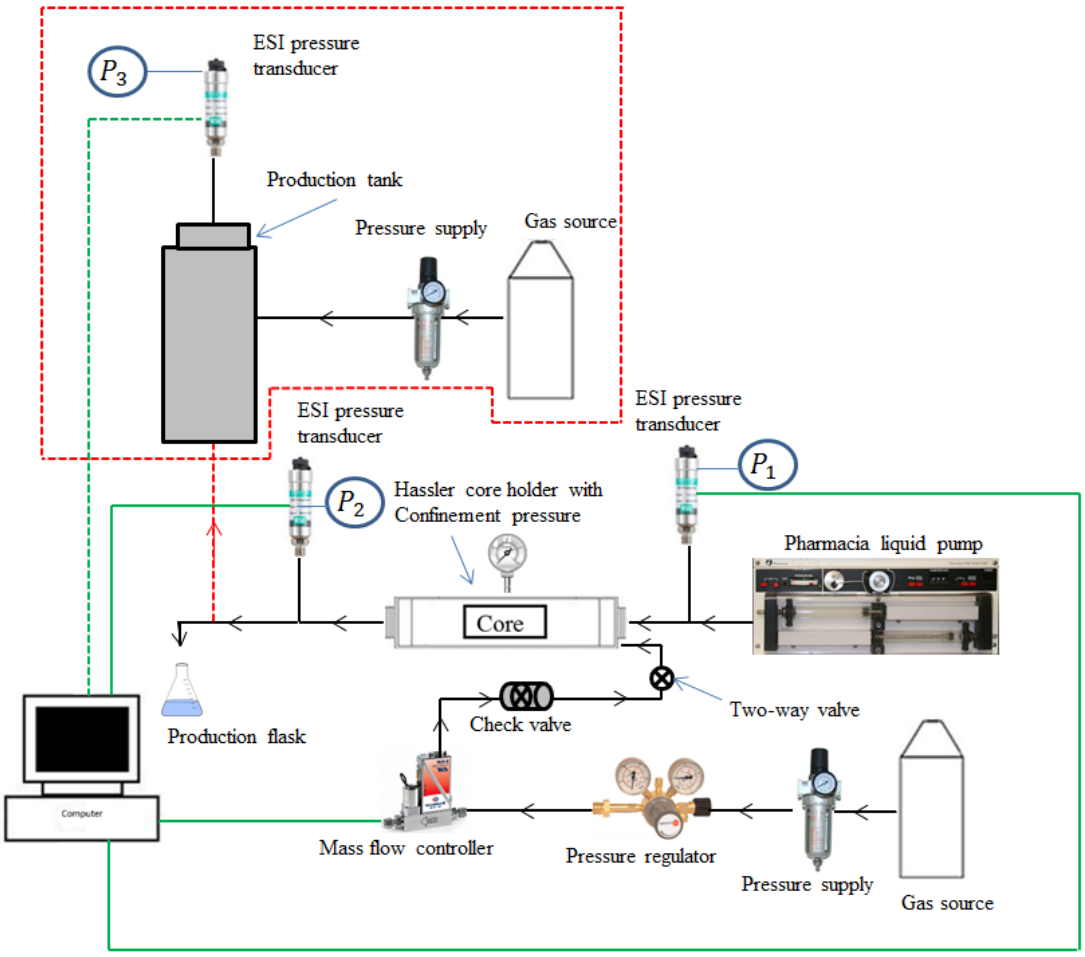

Figure 21: Schematic of the experimental setup used for foam generation during co-injection of gas and surfactant solution in the fractured cores. The black lines are tubing, and the black/red arrows indicate fluid flow direction. The red dashed lines indicate the added equipment in order to improve the setup by reducing the fluctuations in pressure. The green lines represent data cables that connect the pressure transducer and mass flow controller to the computer. The computer record pressure and controls the mass flow controller. P_1, P_2 and P_3 measures inlet, outlet and back-pressure/production tank pressure, respectively.

6.1.1 List of Equipment

- 2-inch fractured marble core
- 4-inch fractured marble core
- Pharmacia LKB P-500 pump
- ESI Digital USB Pressure Transducers, range 0-6 bar (±0,01 % FS)
- Computer for pressure logging and command delivery to mass flow controller
- 1/16” tubing and Swagelok fittings
- Gas source (compressed air)
- Pressure supply, range 0-8 bar
- Bronkhorst EL-FLOW® Mass Flow Controller

- Swagelok Gas Pressure Regulator, Pressure-Reducing/Spring-Loaded
- Swagelok Fluid Flow Check Valve
- Hassler RCHR-Series (2-inch core holder)
- Core Lab X-Ray Core Holder FCH-Series (4-inch core holder)

6.1.2 Experimental Conditions

Table 5 below gives an overview of the conducted experiments performed with the setup shown in **Figure 21**. Note that the experiments were not conducted chronologically.

Table 5: Overview of experiments conducted using the experimental setup in *Figure 21*. The temperature was at standard conditions (25 ^{o}C) in all experiments.

Core ID	Surfactant	Gas	Q_{tot} [cm^3/min]	Backpressure [bar]	Gas fraction	Experiments	Comments
2i-1	-	Compressed Air	3	-	Increasing and decreasing	2	Baseline. No backpressure
2i-1	-	Compressed Air	1	2	Increasing	1	Baseline. With backpressure
2i-1	LS 22-24	Compressed Air	0.5	-	Increasing	1	No backpressure.
2i-1	LS 22-24	Compressed Air	1	-	Increasing	1	No backpressure
2i-1	LS 22-24	Compressed Air	1	2.5	Increasing	1	With backpressure
2i-1	LS 22-24	Compressed Air	2	3.2	Increasing	1	With backpressure
2i-1	LS 22-24	Compressed Air	3	4.2	Increasing	1	With backpressure
2i-1	LS 22-24	Compressed Air	1	3.6	Increasing	1	With backpressure
2i-1	LS 22-24	Compressed Air	2	3.6	Increasing	1	With backpressure
2i-1	LS 22-24	Compressed Air	2.5	3.6	Increasing and decreasing	2	With backpressure
2i-1	LS 22-24	N_2	2.5	3.6	Increasing and decreasing	2	With backpressure
4i-3S	LS 22-24	N_2	5	3.6	Increasing	1	With backpressure
4i-3S	LS 22-24	N_2	8	4.2	Increasing	1	With backpressure

6.2 Laboratory Procedures

Prior to every co-injection, the fractured core was fully saturated with surfactant solution. Prior to the co-injections with backpressure, the core was saturated with surfactant during the pressurization of the system. The pressurization consisted in a stepwise procedure (typically 3 steps) where the compressed air pressure was increased in the production tank during surfactant solution injection at a fixed rate, equal to the first liquid injection rate of the co-injection. The confinement pressure of the core holder was set to be at least 10 bar higher than the system pressure to ensure that fluid flow went through the core.

Gas injection rates were controlled with a mass flow controller, whereas injection rates of the aqueous surfactant solution was regulated with the Pharmacia pump. A key step in the experimental procedure was to equilibrate the inlet and outlet pressure. This was done by injecting gas from the mass flow controller into the tubing with the two-way valve closed. This caused the pressure in the tubing to increase towards the fixed supplied drive pressure, which would eventually equilibrate. If this step was skipped, the large pressure difference between the production tank and tubing would have caused a pressure gradient towards the mass flow controller, which potentially could destroy the delicate equipment. Consequently, always ensuring that the drive pressure delivered to the mass flow controller was higher than what the backpressure potentially could increase to was important. Pressure was logged on the computer and injection rates were varied with gas fraction accordingly. Produced fluids accumulated in a sealed tank where pressure was measured with an ESI USB pressure transducer. To shut down an experiment the two-way valve was closed and both the Pharmacia pump and mass flow controller was disconnected. The system was gradually depressurized in a stepwise procedure, much like the pressurization. This was also a very effective way to produce any gas still left in the core. Finally, the confining pressure was removed.

7 Visualization of Fractures and Foam Flow in Fractured Cores Using PET/CT

To gain knowledge of local surfactant distribution within the fracture network during co-injection, a PET/CT visualization experiment was conducted at Haukeland University Hospital in Bergen. The scanner operates both CT- and PET examinations at the same time. By merging CT with PET, a 3D visualization of the core sample and the injected fluid can be computed. The PET/CT-scanner is used for patients undergoing cancer treatment in weekdays, so our experiments were conducted during weekends. The CT-scans were used to characterize the fractures in the 2- and 4-inch fractured marble cores. Co-injection for in-situ foam generation by surfactant solution and gas (nitrogen) was conducted on both the 2- and 4-inch cores. Fluorodeoxyglucose (^{18}F - FDG) was used as a radioactive tracer labeling the liquid surfactant solution phase. The experiment on the 2-inch core was conducted single-handedly, whereas the experiment on the 4-inch was conducted in collaboration with fellow master student Sigbjørn Aasheim Johansen. A radiologist employed at Haukeland University Hospital operated the PET/CT scanner's settings. The experimental setup is nearly identical to the setup explained in **Section 6** (except for the PET/CT scanner). Additionally, the majority of laboratory components are similar in all experiments conducted in this thesis. For a detailed component description, the reader may review **Section 5.1** and **Section 6.1**.

List of Equipment

- 2-inch fractured marble core
- 4-inch fractured marble core
- Pharmacia LKB P-500 pump
- ESI Digital USB Pressure Transducers, range 0-6 bar (±0,01 % FS)
- Computer for pressure logging and command delivery to mass flow controller
- 1/16" tubing and Swagelok fittings
- Gas source (compressed air)
- Nitrogen tank (P_{max} = 220 bar)
- Pressure supply, range 0-8 bar
- Bronkhorst EL-FLOW® Mass Flow Controller
- Swagelok Gas Pressure Regulator, Pressure-Reducing/Spring-Loaded
- Swagelok Fluid Flow Check Valve
- Hassler RCHR series (2-inch core holder)
- Core Lab X-Ray Core Holder FCH-Series (4-inch core holder)
- Simens Biograph™ TruePoint™ medical PET/CT scanner

7.1 Laboratory Procedures

CT dry-scans were obtained to visualize and characterize the fractured cores. The core holder was placed horizontally and aligned with laser in the PET/CT scanner and all the equipment was set up in the PET/CT room, shown in **Figure 22** below. CT scans of both the 2- and 4-inch cores 100% saturated with surfactant solution was obtained at experimental conditions (P = 3.6 bar, T = 25 ^{o}C) to be used in a merge with the PET imaging, before the co-injection commenced. The laboratory procedure was identical to that described in **Section 6.2**. However, the number of measured gas fractions (for the co-injection on the 2-inch core) was reduced from 7 to 4. Instead of having 14 measured gas fractions (7 each way), this co-injection used 8 gas fractions (4 each way). Generation of ^{18}F, a water soluable tracer, takes place in a cyclotron controlled by a radiologist. A certain volume (~a few ml) of radioactive ^{18}F with a specific activity[6] of approximately 350MBq was delivered in a special case of lead. By the use of a regular syringe, a small volume of the radioactive isotope was extracted and injected with liquid surfactant solution, where it was mixed using a small metallic stick. The liquid injection pump was then filled with ^{18}F-labelled surfactant solution, and the co-injection was started. The co-injection and entire PET run lasted for about eight hours. The imaging was organized in 16 sequences: 10 minutes with imaging followed by a 20-minute intermission equaled one sequence. This procedure progressed continuously throughout the experiment.

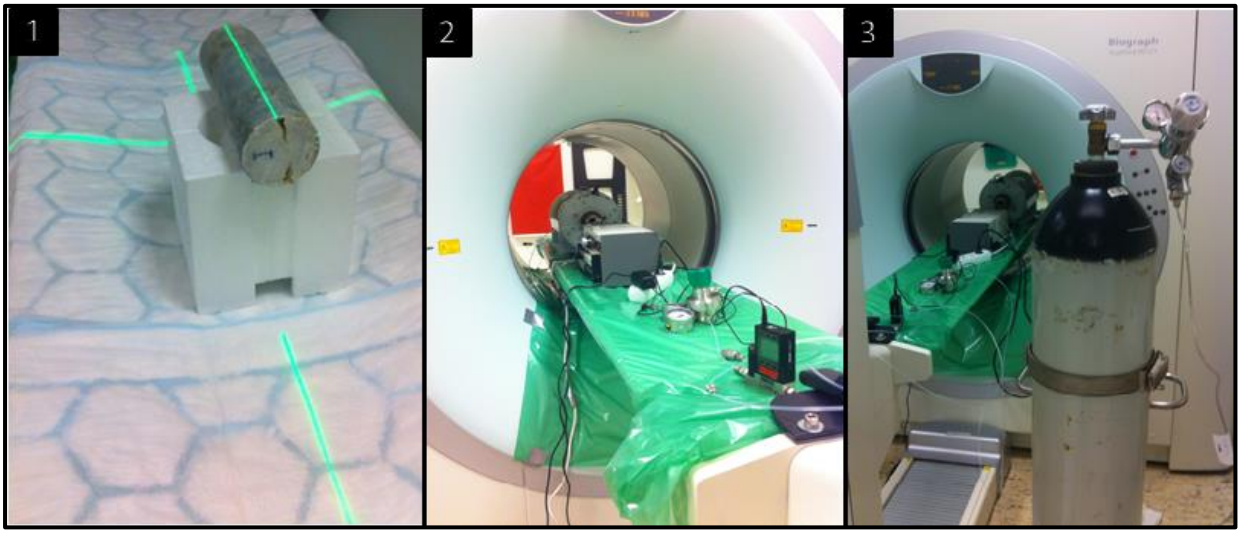

Figure 22: CT-scan and overview of the experimental setup. 1) A laser function on the PET/CT machine was used to perfectly align the coreplug for scanning (dryscan). Both 2) and 3) display how the components were distributed/aligned on the patient table, except for the highly pressurized nitrogen tank (shown in the second image). The patient table was adjustable in both longitudinal and vertical direction. During the CT scan that was run prior to the PET/CT experiment to characterize the fractures of the core, the patient table was required to move in the longitudinal direction. Having flexible and sufficient length on the tubing was therefore necessary.

[6] Specific activity is the activity (radioactivity) per quantity (unit mass) of a radionuclide

Chapter III – Results and Discussion

Chapter III presents results, analysis and discussions from the experiments performed in this thesis, starting with the characterization of the fracture networks, before the investigation of foam generation by in-situ co-injection of surftactant solution and gas in the fracture networks is presented. Then, the visualization of foam generation and flow in the 2- and 4-inch fractured cores using PET/CT technology is presented, and finally visualization analysis of the fractured block network. The main focus of this thesis is results obtained from the 2-inch fractured marble core. The 4-inch fractured core and block are investigated as side-studies to supplement discussion and possible conclusions, in addition to function as an upscale-evaluation.

8 Characterization of Fracture Networks

Characterization of the fractured systems used in this thesis will be presented in individual sections below: starting with the 2-inch fractured core, before including the 4-inch fracture core and fractured block network. The objective was to investigate whether variations in differential pressures could be explained by differences in the fracture networks identified and characterized in this section.

8.1 Fracture System in 2-inch Core

The 2D spatial fracture distribution using CT is shown in **Figure 23**. Only selected images are shown to demonstrate the variation in size, orientation and intensity along the system length. These fractures represent the 2-inch core where all the co-injections were performed. Normalized positions (X_D) are added to each slice, where 0 is inlet and 1 is outlet. The high-resolution X-ray computed tomography (CT) provides 2D sequential images of a given thickness (0.6 mm) which can be stacked together to create a 3D visualization model (shown in **Figure 25** below) of the core. High density regions are observed as brighter areas such as the dense rock material (marble), whereas darker areas reflect regions of lower density such as the fractures. Each image has been processed individually, and greyscale and brightness has been slightly adjusted for visualization purposes to accentuate the fracture topography in the core. Hence, the greyscale in one image cannot necessarily be directly compared (visually) to the greyscale in another image to determine relative rock densities.

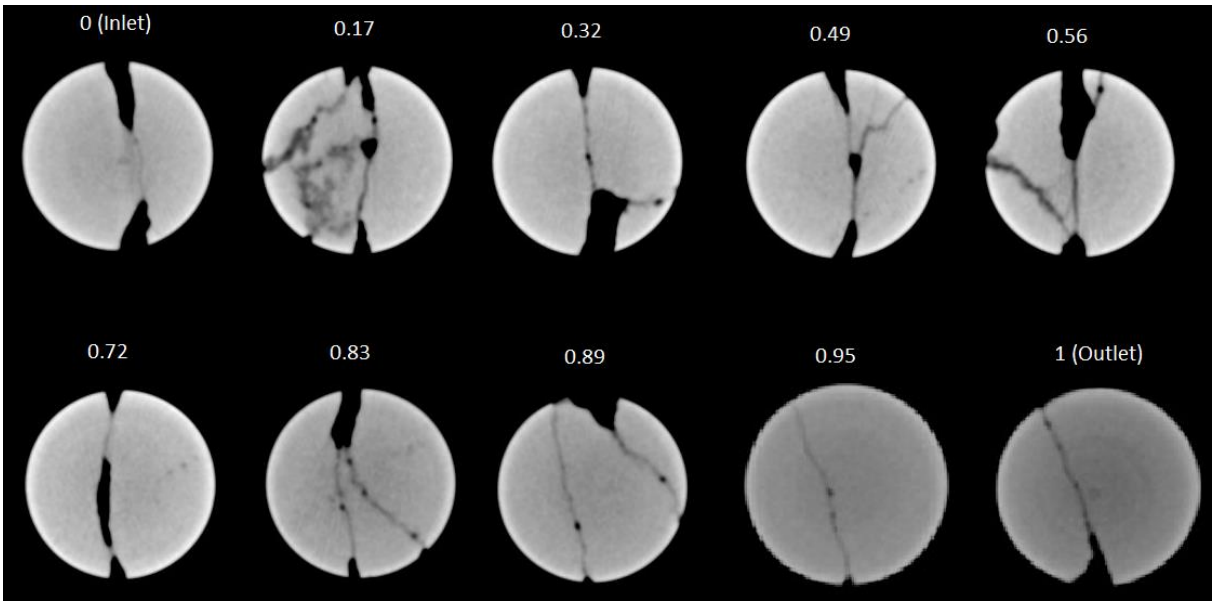

Figure 23: 2D (XY-direction) image montage from the CT-dryscan of the 2-inch fractured core. Above each image is a number fraction relating the slice to its dimensionless position from the end (outlet). It is fascinating to see the large variations in the fracture network across the length of the core.

The core was drilled from a marble block, and considered homogeneous. This was confirmed by the CT images which has a uniform brightness across the entire core length and height both at a core and microscopic level. Both the 2D xy-slices in **Figure 23** and 3D model in **Figure 25** and **Figure 26** shows two large parallel fractures in the longitudinal direction along the top and bottom across the entire core (except ~X_D=0.95-1 for the top). These fractures are likely to be responsible for the highest transmissibility of fluids through the core. In case of fluid segregation, gas will rise to the fracture located at the top, whereas the liquid surfactant solution will flow along the fracture at the bottom. When the gas and surfactant solution mixes and generates foam in-situ in the large transmissibility fractures, this will divert the flow to lower transmissibility fractures, hence improving the mobility control by mitigating fluid segregation and promote foam generation in these fractures. Additionally, large open vugs are located in the horizontal cross-section, as shown in **Figure 24** below. It is likely that fluid can accumulate and mix in such vugs to generate foam.

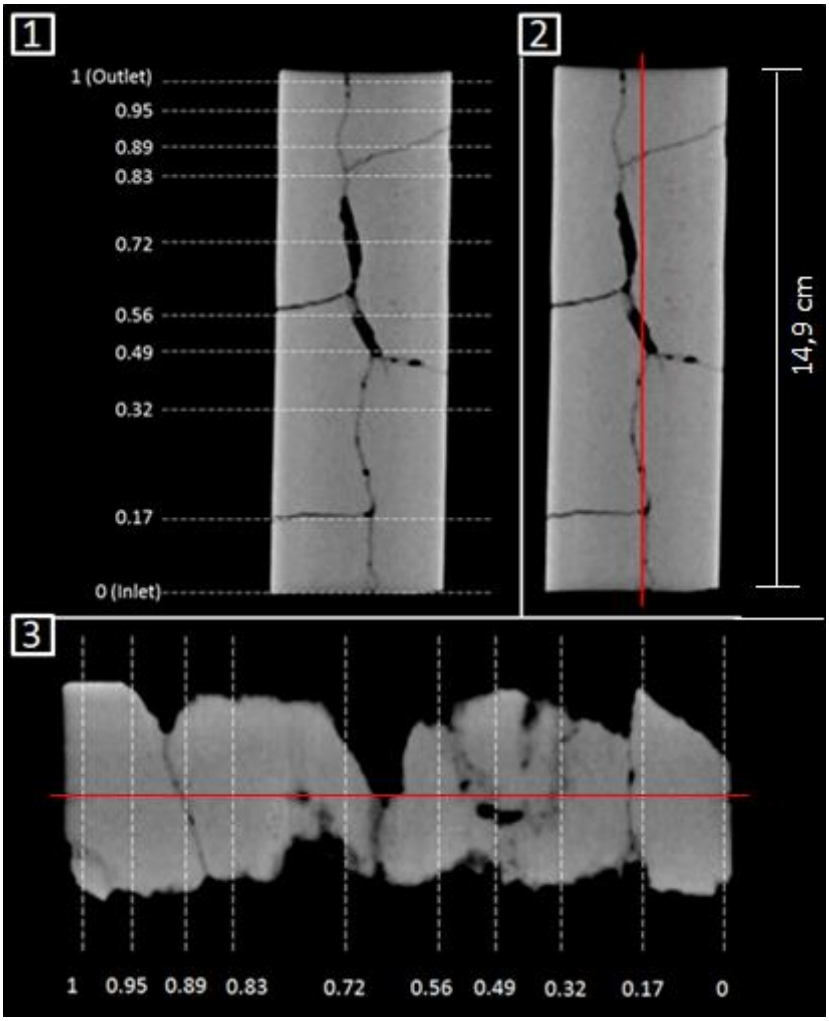

Figure 24: 2D images from the CT-dryscan of the 2-inch fractured core. 1) Bird's view of the horizontal slice (XZ-direction) from the center of the core. The white dashed lines and their respective numbers represent each XY-slice shown in *Figure 23* and their dimensionless position. 2) Horizontal slice (XZ-direction). Note that the horizontal slice is from the middle of the core. The red line represent the length of the vertical cross-sectional slice shown in 3). 3) Vertical cross-sectional slice (YZ-direction) of the core. The white dashed lines and their respective numbers represent each XY-slice and their dimensionless position. The red line show the horizontal slice in 1) and 2)

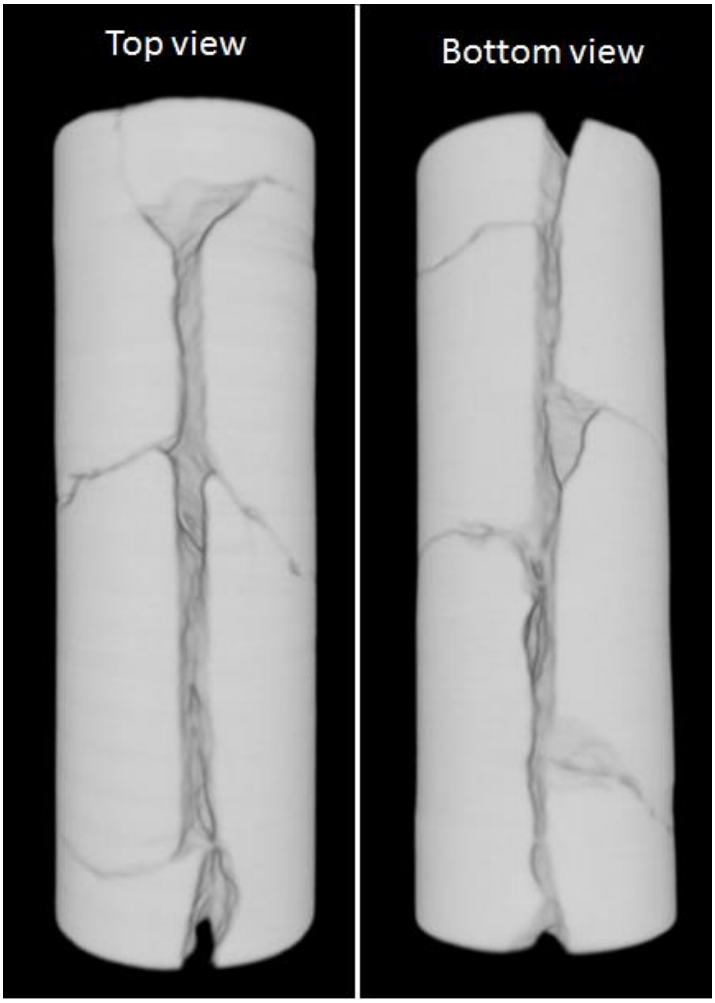

Figure 25: 3D images from the CT dryscan of the 2-inch fractured core. To the left is a top view (bird's perspective) of the core, whereas the image on the right is a bottom view. The 3D model had a high definition/resolution, and the fractures were detailed and easy to observe.

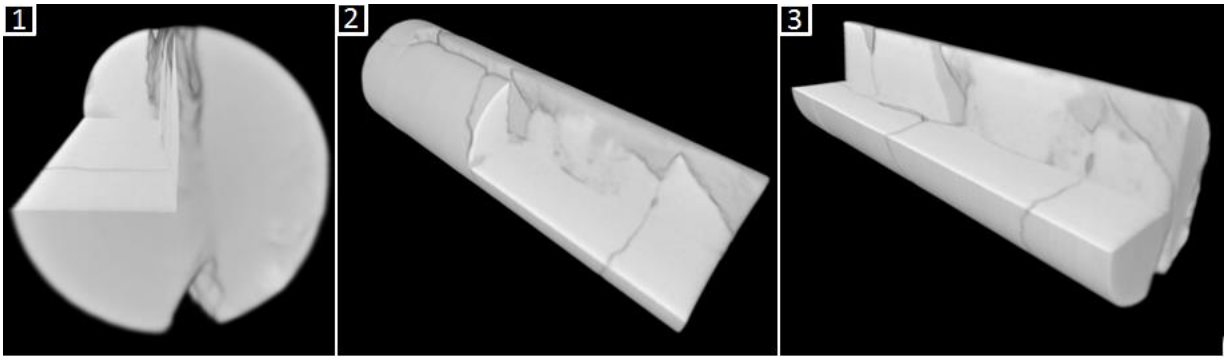

Figure 26: Cropped 3D images from the CT dryscan of the 2-inch fractured core. The figure is intended to try to replicate the fascinating fracture network in the 3D model. The cropping function provided a unique perspective inside the core itself. The x-, y- and z-axis could be regulated individually to slice/crop into the core and give highly detailed view of the fractures. 1) Front view of the core with a cropped corner. Staring down the length of the 3D core gives a feeling of being inside the fractures of the core itself. 2) Side-view with a corner crop to the middle of the core. The vertical cross-section in this image is the upper half of the vertical cross-section shown in *Figure 24 - 3)*. 3) Slide-view with a corner crop of the entire length of the core. The horizontal slice in the center is the leftmost half of the horizontal slice shown in *Figure 24 - 1*) and *2)*.

8.2 Fracture System in 4-inch Core

The 4-inch core material consisted of three stacked cores (2 x ~8.8 cm and 1 x 9 cm). The 2D spatial XZ (horizontal slice) fracture distribution using CT is shown in **Figure 27**. The images are obtained at two different heights: one slightly below the center of the core, and one slightly above the center. The images demonstrate variation in size, orientation and intensity along the system length. A 3D visualization model is shown in **Figure 28** below. Both the 2D XZ-slices in **Figure 27**and 3D model in **Figure 28** shows two large vertical parallel fractures perpendicular to the bulk flow direction (from right to left), which are the open fractures that separate the stacked core units. These highly transmissible fractures with constant aperture are likely to be responsible for a large accumulation of fluids. Additionally, each of the core has two major fractures and the top and bottom due to the available contact area of the fracture tool (discussed in **Section 4**), but the core units were intentionally stacked and oriented as shown in **Figure 28** to increase the roughness and complexity of the fracture network. In case of fluid segregation by gravity prior to foam generation, gas will rise to the top in the highly transmissible fractures, whereas the liquid surfactant solution will flow along the bottom of the fractures. When the gas and surfactant solution mixes and generates foam in-situ in the large transmissibility fractures, this will divert the flow to lower transmissibility fractures (and cross-flow), hence improving the mobility control by mitigating fluid segregation and promote foam generation in these fractures.

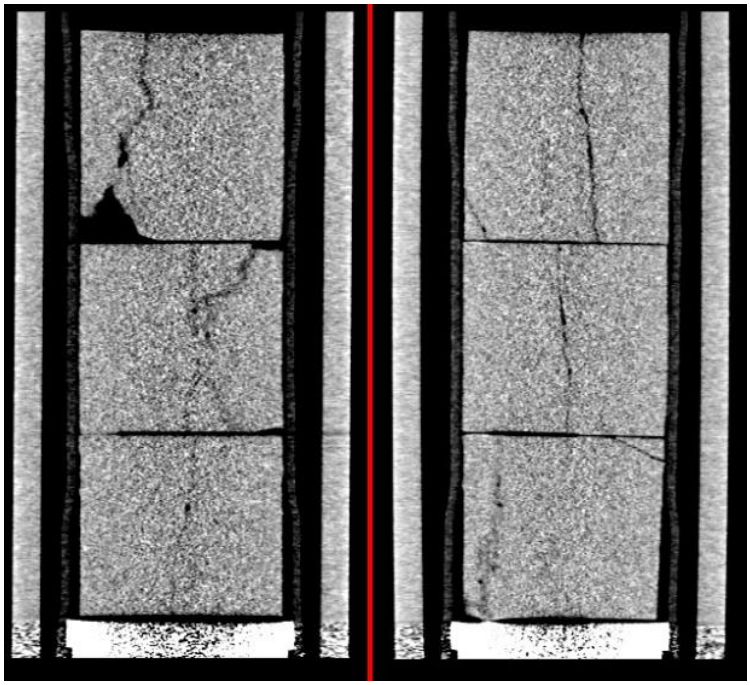

Figure 27: 2D XZ images from the CT-dryscan of the 4-inch fractured core. Bird's view of the horizontal slice (XZ-direction) from slightly below (left) and sligthy above (right) the center of the core.

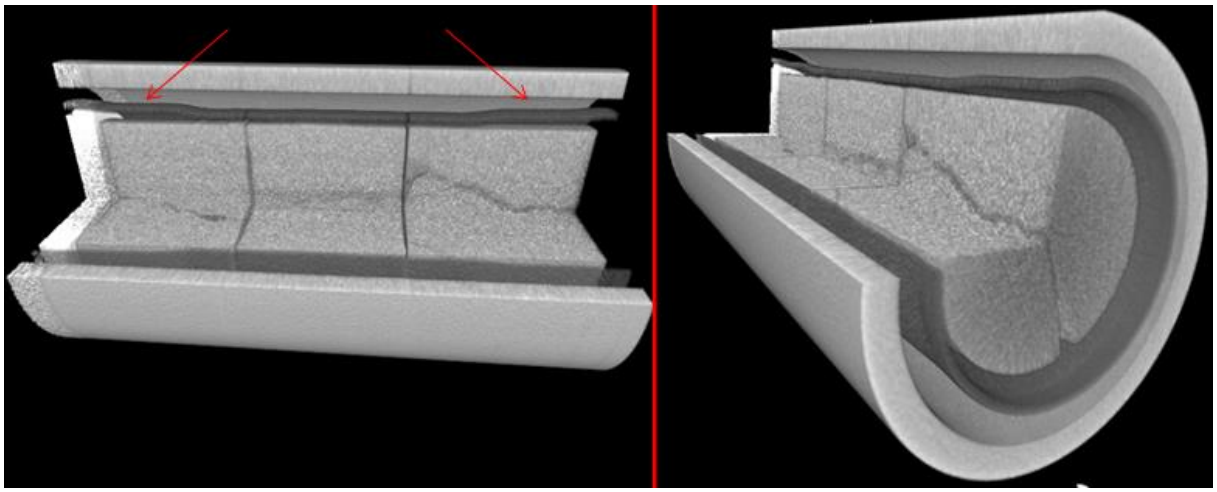

Figure 28: Cropped 3D images from the CT dryscan of the 4-inch fractured core. The figure is intended to try to replicate the fascinating fracture network in the 3D model. The cropping function provided a unique perspective inside the core itself. The x-, y- and z-axis could be regulated individually to slice/crop into the core and give highly detailed view of the fractures. To the left is a side-view with a corner crop of the entire length of the core. The red arrows points at two bumps in the rubber sleeve. These are the sections where duct-tape was wrapped around the core to extend the width in order to prevent fluid flow around the core, as discussed earlier (cf. *Figure 18*). To the right is a slightly tilted frontal view of the core.

8.3 Fracture System in Rectangular Block

The fractured block system shown in **Figure 29** below consisted mainly of narrow fractures and 12 large fractures. The open, vugular fractures were larger bodies of open space and had a variation in aperture ranging from 0.4-2.2 cm. These 12 vugs were used as reference points when evaluating foam propagation and development of foam texture during co-injection. Injected fluids are likely to be dictated by the high transmissibility in the open fractures in the longitudinal direction (from inlet to outlet), but once foam is generated here, an increased cross-flow to smaller fractures perpendicular to the bulk flow direction is likely to take place as a result of fluid diversion and blocking. Additionally, under the assumption that the system is water-wet, gas will preferentially flow in the largest fractures due to more favorable capillary pressure than in small fractures. In case of snap-off, the gas phase will therefore be capillary trapped in large fractures. The majority of fractures in sector 4 and 5 have fairly consistent aperture. Thus, less contrasts in permeability is expected to exist in this region.

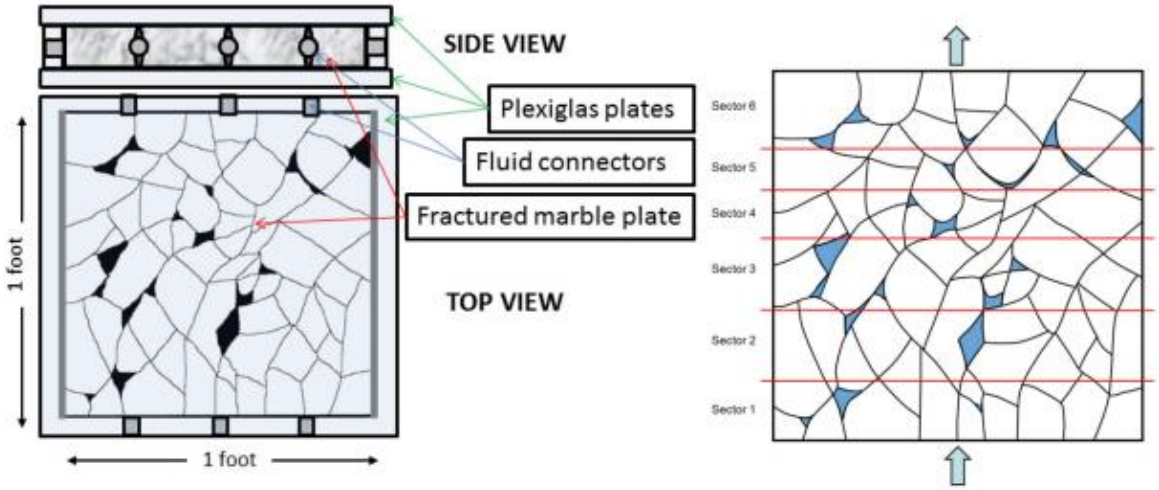

Figure 29: Schematic of the fractured block system, sealed between two Plexiglas plates (left). 6 sectors (right) were defined and used as reference points when evaluating foam propagation through the fracture network and the largest open fractures/vugs were regularly checked to observe the development of foam texture during the co-injection and as gas fraction varied. Figure from (Fernø et al., 2016).

9 Foam Generation by Co-Injection in Fractures

Foam generation during co-injection of surfactant solution and gas with variable fractional flow at various constant injection rates was evaluated using three different scaled fracture networks. The results are presented individually in the sections below: starting with the 2-inch fractured core, before including the 4-inch fractured core and fractured block network.

9.1 2-inch Fractured Marble Core

Co-injections of surfactant solution and gas were performed to study foam generation in a 2-inch diameter fractured marble core saturated with surfactant solution. 14 co-injections were performed and foam generation was evaluated by analyzing the differential pressure as a function of gas fraction when injection rates and outlet pressure conditions were varied.

9.1.1 Baselines – Increasing and Decreasing Gas Fraction

Three baseline tests established reference differential pressure curves that were compared with the pressure regimes in the foam generation experiments: Two experiments were conducted at the same conditions that were used during foam generation experiments *without* backpressure, with synthetic brine as the liquid injection phase. A single baseline experiment was conducted *with* backpressure to reduce pressure fluctuations from gas compressibility. Because no foam can be generated without foaming agent, it was assumed that any increase in differential pressure over the core originated from the injected gas that reduced the relative permeability of the brine and gas, and potential trapped gas that would decrease the overall transmissibility of the fracture network.

Increasing and Decreasing Gas Fraction Without Backpressure

Figure 30 shows the differential pressure as a function of gas fraction during baseline tests with co-injection of gas (air) and brine (1 wt% NaCl). Gas fraction was changed when the differential pressure was stable. Because the pressure transducers measured pressure from two phases (gas and liquid) the pressure would always fluctuate a little, but the trends were distinctive. Prior to each baseline test, the core was flushed and fully saturated with brine. Both experiments had a total injection rate of 3 cm^3/min. The baseline test with increasing gas fraction had a stable differential pressure before it started to increase at f_g=0.6 and peaked at f_g=0.7. Gas will presumably rise to the fracture located on the top half of the core because of gravity segregation and density difference. The high transmissibility of the fractures is therefore likely to account for a rapid increase in gas mobility already at low gas saturations, ie. low gas fractions ($<f_g$=0.5). Thus, effective permeability of both water and gas is high at low gas fractions, effectively contributing to a flow resistance between the two phases, and hence an increase in differential pressure. The steep decline in differential pressure after f_g=0.7 may be explained as the following: The large contrast in viscosity between gas/water

makes it reasonable to assume that the largest variations in differential pressure is governed by water. Thus, as gas displaces water to a critical water saturation (apparently near f_g=0.7), the differential pressure decrease drastically because water is nearly (if not entirely) immobile. Further assuming that water is wetting to gas in the core, gas will flow in the center of the fractures with low resistance to flow, hence the low differential pressure. As gas fraction increase from f_g=0.7 to f_g=1 the fractional flow and hence mobility of gas increase, and is likely flowing through the highly conductive fractures with low resistance to flow. The baseline test with decreasing gas fraction has a slightly higher differential pressure compared with increasing gas fraction. This is because of the higher gas phase resistance to flow at the initial stages of the test when the saturation of brine is still high (much like an immiscible gas injection). The differential pressure increase ~133% from f_g=1 to f_g=0.7. As gas fraction decrease from f_g=0.7 the differential pressure remains stable. A disparity in differential pressure between the co-injection with decreasing gas fraction compared with increasing gas fraction is observed. Trapped gas was likely the reason for this "differential pressure hysteresis". An explanation to why more gas is trapped in the baseline with decreasing gas fraction is that the fractional flow of gas is high in the initial stages of the co-injection (high gas fraction). With the assumption that water is wetting to gas on the marble rock surface, gas would displace the water in the center of the largest fractures. As gas fraction decreases, water will start to flow in the fracture films and eventually snap-off the gas phase. A large fraction of the trapped gas is therefore most likely to be encapsulated in the largest fractures, hence leading to a considerable trapped gas saturation. Thus, the relative permeability of water will be reduced due the water now having to flow along the films because trapped gas is blocking the flow path in the center of the fractures, hence causing an increased resistance to flow, leading to a larger differential pressure.

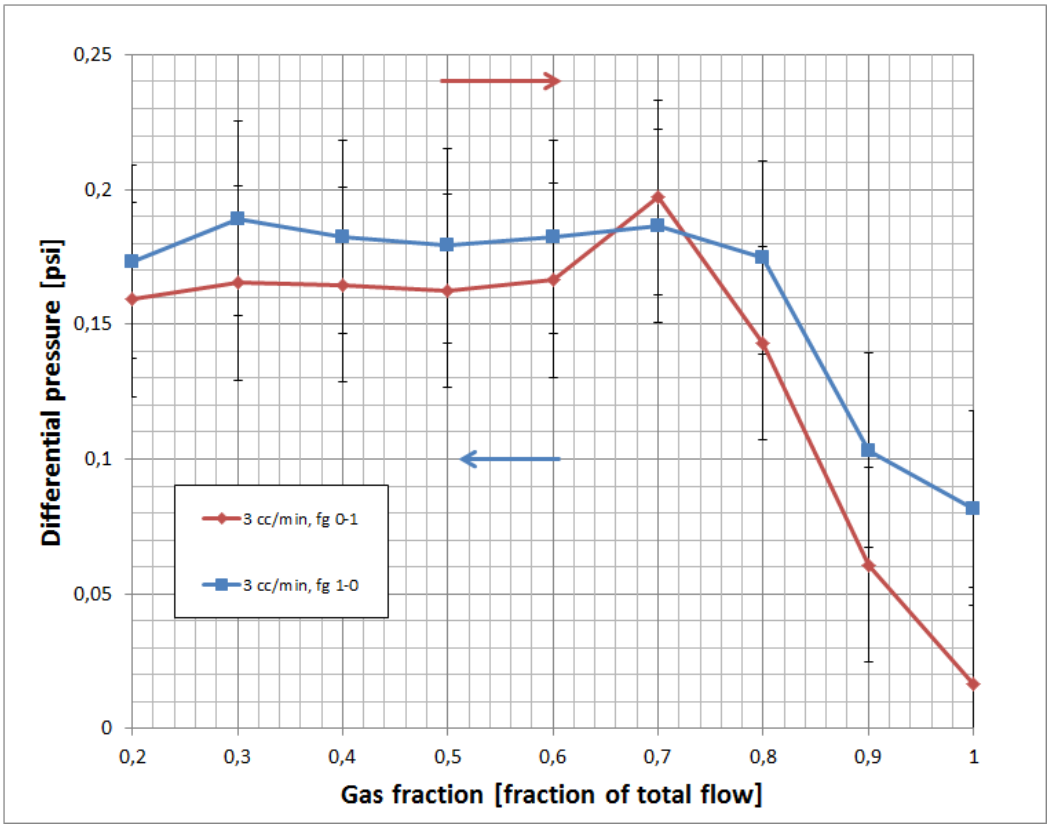

Figure 30: Differential pressure [psi] as a function of gas fraction for both baseline tests without backpressure. f_g: 0-1 denotes increasing gas fraction and f_g: 1-0 denotes decreasing gas fraction. Both baseline experiments had a constant total injection rate of 3 cm^3/min. Each pressure point in the curve is an averaged value of all the pressures that was logged during each gas fraction interval/sequence. The gas fraction was changed when the differential pressure was stabilized. The blue and red arrow represent whether the gas fraction is increasing or decreasing.

Increasing Gas Fraction With Backpressure

Figure 31 shows the result from the baseline test with backpressure during co-injection of gas (air) and brine (1 wt% NaCl concentration). Gas fraction was changed when the differential pressure was stable. Prior to the co-injection, the core was flushed and fully saturated with brine. The experiment had a constant total injection rate of 1 cm^3/min and a backpressure of 2 bar (~29 psi). The behavior was not as expected, compared to the baseline *without* backpressure (cf. **Figure 30)**. The differential pressure increased as gas fraction increased, and peaked at f_g=0.9 before it dropped. From start of co-injection to their respective peaks in differential pressure, the baseline *with* backpressure demonstrated an increase of ~416%, whereas the baseline *without* backpressure had an increase of ~25%. The substantial difference in pressure build-up may be explained as a consequence of surfactant retention. Prior to the baseline experiment with backpressure, two-digit foam generation experiments had been conducted on the core. It is likely that during these experiments, some surfactant retention has occurred. The accumulated surfactant concentration due to retention in the core is probably sufficient for a minor foam generation. The decrease in pressure from the peak at f_g=0.9 to f_g=1 was ~9%. The lack of decline in differential pressure compared to the baseline *without* backpressure may be explained as a combination of the following factors: 1) Low

total injection rate (1 cm^3/min) can lead to inadequate viscous drag on the water by the injected gas, hence leading to a higher irreducible water saturation, and thereby a higher flow resistance of the gas phase. Additionally, the backpressure is likely to elevate the overall resistance to flow. 2) Capillary end-effects results in an accumulation of the wetting phase (liquid) at the outlet of the core. Thus, gas encounter a high resistance to flow near the outlet even at high gas fractions, hence increasing the differential pressure. Capillary end-effects will be further addressed in **Section 10.1** below. 3) Assuming a significant surfactant retention, the lack of decline in differential pressure may be explained as a considerable fraction of stable foam. Considering these factors, it is strongly recommended that a new baseline is reproduced to verify assumptions made here.

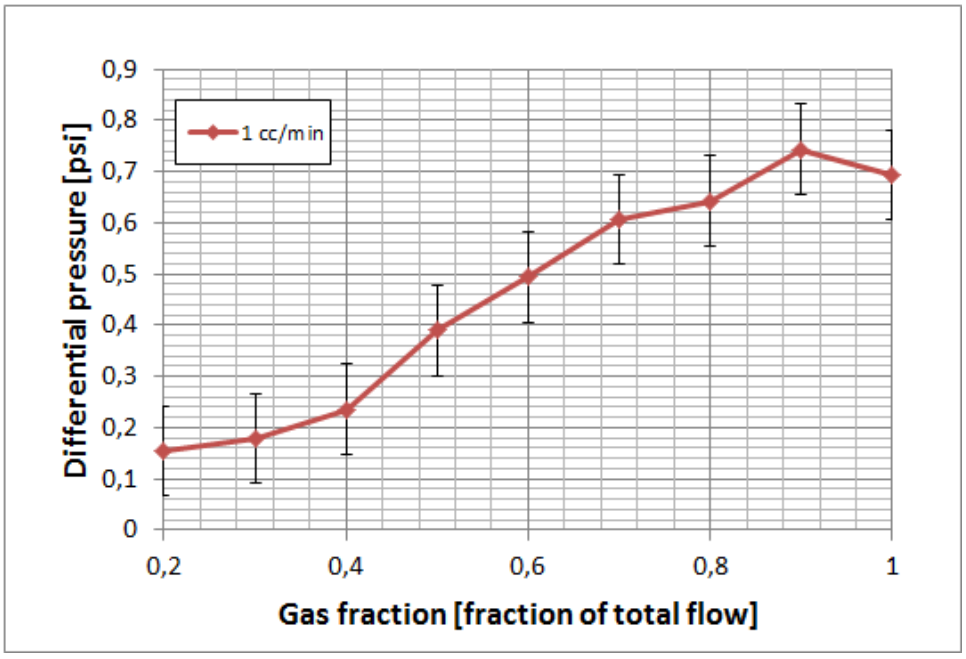

Figure 31: Differential pressure [psi] profile as a function of gas fraction for the baseline test with backpressure (2 bar / ~29 psi). f_g: 0-1 denotes increasing gas fraction. The baseline experiment had a constant total injection rate of 1 cm^3/min. Each pressure point in the curve is an averaged value of all the pressures that was logged during each gas fraction interval/sequence. The gas fraction was changed when the differential pressure was stabilized.

9.1.2 Varying Injection Rate and Outlet Conditions

After conducting the baseline tests, foam generation experiments was performed by coinjecting gas (compressed air) and surfactant solution into the fractured marble core initially saturated with brine. The objective was to investigate how foam generation was affected by varying the co-injection rates and outlet conditions. Differential pressure as a function of gas fraction was analyzed and the results were compared for discussion.

Co-injections Without Backpressure

A series of co-injections without backpressure were conducted. **Figure 31** below shows an example of the differential pressure-rawdata. The large scatter in differential pressure was observed in every experiment without backpressure, and is an effect of gas compressibility, which increase the rate of bubble coalescence (also at lower gas fractions, ie. $<f_g=0.5$). Gas compressibility makes bubbles contract and expand as they flow towards the lower pressure at the outlet, which prevents bubbles from changing from polyhedral foam (thin film) to round/spherical foam (strong foam) throughout the fracture. Therefore, both bubble shapes are flowing through the fracture over a range of fractional flows, hence making the differential pressure fluctuate/unstable (Kovscek et al., 1995). Subsequently, most lamellae are in positions, such as pore throats/bodies or in zones where the cross-sectional boundary changes (like a converging fracture), where they increase the resistance to flow (Rossen, 1989). The change in bubble shape can disrupt the capillary pressure gradient, hence making bubbles "jump" from one region to another to equilibrate the change in pressure gradient (Rossen, 1990). Already at the first gas fraction, gas compressibility effects was observed with irregular production rates associated with larger fluctuations in pressure. This happened repeatedly throughout every experiment without backpressure. The overall pressure increased with increased gas fraction until it peaked around $f_g=0.6$ in all experiments, cf. **Figure 33** below. The steep decline in differential observed from $f_g=0.6$-1 is generally characterized as "weak foam", and demonstrate the adverse effects of gas compressibility on the balance between foam generation, stability and coalescence at high gas fractions. As the foam became more dry (higher foam quality/gas fraction), the fluctuations decreased (cf. **Figure 32**). The evident decrease in fluctuations together with decline in pressure suggests a very limited presence of foam. The obvious change in fluctuations at high gas fractions indicate that gas (which has the highest fractional flow) encounter low resistance to flow from other phases such as water and foam (pseudo-phase) and/or trapped gas bubbles. The experiments performed without backpressure provided valuable knowledge of the adverse effects of gas compressibility on foam stability, and demonstrated the ability to generate foam when a foaming agent was present. To improve the control of flow out of the core and reduce gas compressibility effects a backpressure was installed at the outlet. Similar scatter in differential pressure as shown in **Figure 32** has been reported in the literature, and Buchgraber et al. (2012) connected a backpressure regulator at the downstream end of their flowing model in order to elevate the system pressure and thereby reduce gas compressibility effects and provide better control of the foam quality. This was later implemented in the experimental setup used in this thesis (see the following under-sections).

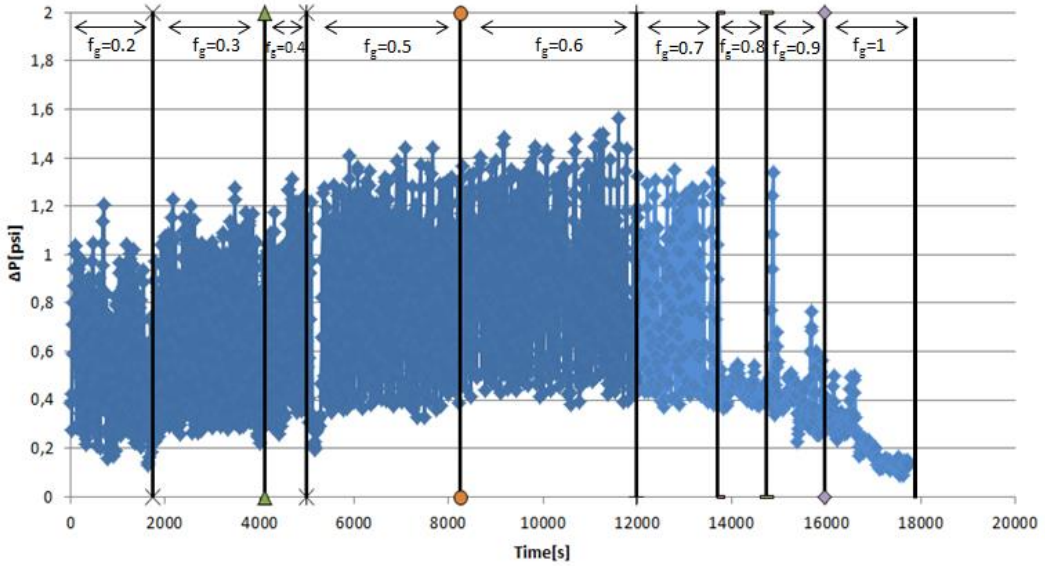

Figure 32: The differential pressure [psi] as a function of time during a foam generation experiment in the 2-inch fractured core, with a total flow rate of 1 cm^3/min. The black vertical lines represent gas fractions. Despite the large scatter in the pressure, there is an evident trend in which the average differential pressure increases with gas fraction until it peaks at f_g=0.6. 3 out of 3 experiments conducted without backpressure had a scatter in differential pressure, but similar trends as a function of gas fraction. The highest average differential pressures was reached in the gas fraction range of f_g= 0,6-0,7 for all experiments without backpressure.

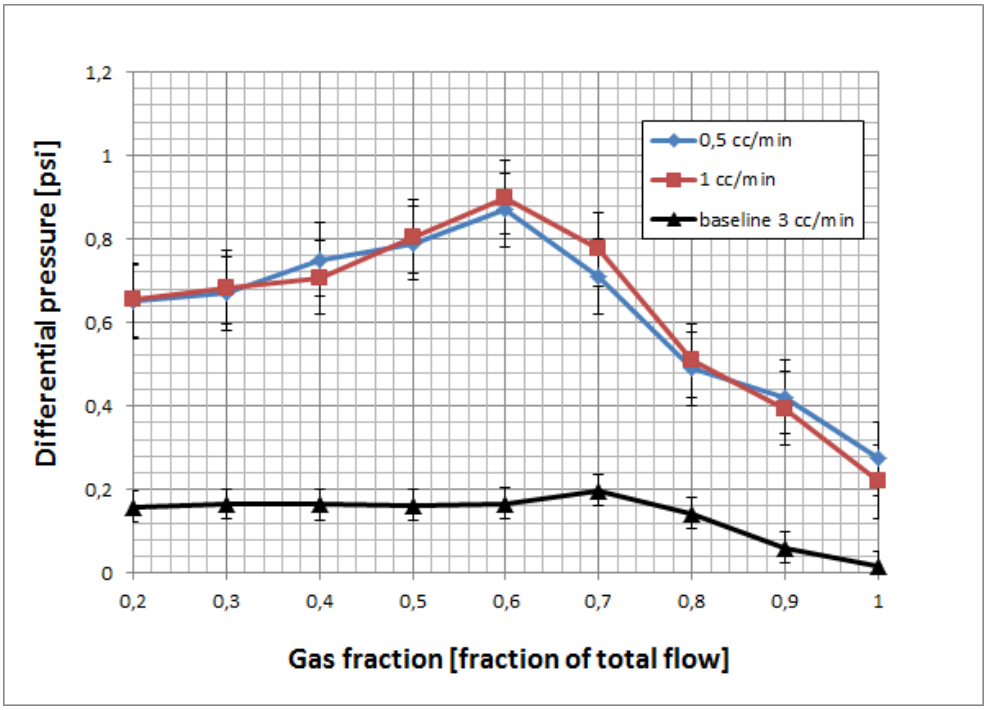

Figure 33: Differential pressure [psi] as a function of gas fraction during co-injection of surfactant solution and gas (air) using 2 constant total rates in the fractured 2-inch core. All curves are based on co-injections conducted with an increasing gas fraction (f_g=0-1) . Each point is an averaged value of every differential pressure logged in the time span each gas fraction was run. The gas fraction was changed when the average differential pressure was stablilized. All total injection rates (0.5, 1 and baseline 3 cm^3/min) show correlative behavior: increasing differential pressure with increasing fractional flow until a sudden drop at high fractional gas flow. The largest differential pressure was observed for f_g=0.6 for the co-injections with surfactant and gas, and f_g=0.7 for the baseline. All co-injections were conducted without backpressure.

Co-injections Varying Backpressure

Figure 34 shows a series of co-injections of surfactant solution and gas (air) was conducted while varying outlet conditions (backpressure) and total injection rate. The core was fully saturated with surfactant solution in every experiment. This step was performed to streamline the experiments (with respect to time) as this was analogously to flushing the core with surfactant at f_g=0, and the co-injection of gas and surfactant could commence instantly. By saturating the core with surfactant solution prior to every experiment (f_g=0) the foaming ability was enhanced, especially at lower gas fractions. This is presumably one argument to why the differential pressure increase quite rapidly at low gas fractions, compared to what is reported in earlier work on foam mobility in fractured systems (Fernø et al., 2016, Kovscek et al., 1995).

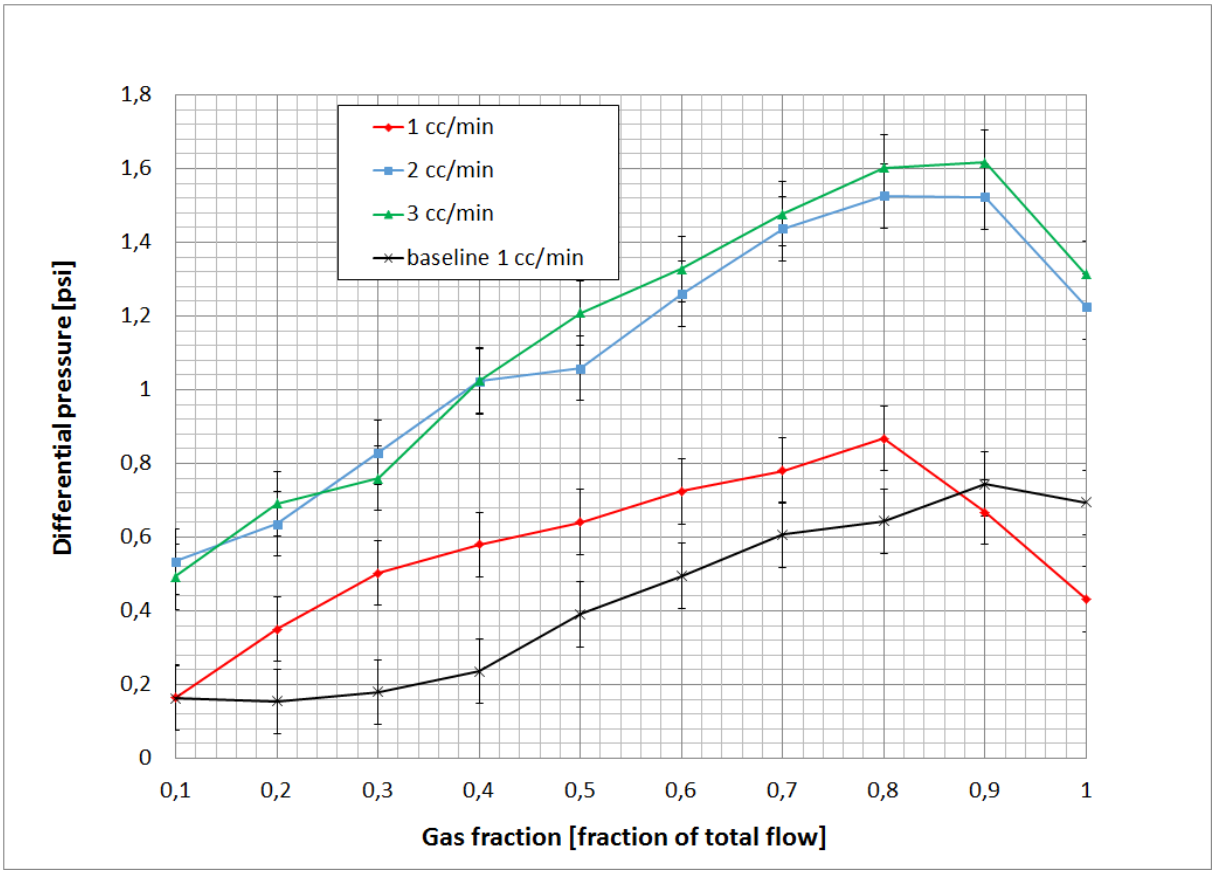

Figure 34: Differential pressure [psi] as a function of gas fraction during co-injection of surfactant solution and gas (air) using 3 constant total rates in the fractured 2-inch core. The curves reflect foam generation ability in the 2-inch fractured core at different outlet conditions (varying backpressure) and different total injection rate. All curves are based on experiments conducted with an increasing gas fraction (f_g=0-1). Each point is an averaged value of every differential pressure logged in the time span each gas fraction was run. The gas fraction was changed when the differential pressure was stabilized. All total injection rates (1, 2 and 3 cm^3/min) show the similar/correlative behavior: increasing differential pressure with increasing fractional flow until a sudden drop at high fractional gas flow. The largest differential pressure was observed for f_g=0.8 (for 1 and 2 cm^3/min) and f_g=0.9 (for baseline 1 and 3

The foam generation experiment was performed with a backpressure of 2.5 bar (~37 psi). It was expected that the 1 cm^3/min baseline should be monotonically lower than the co-injection of surfactant solution and gas with the same injection rate. However, above f_g=0.9 the baseline measured a higher differential pressure, due to reasons discussed in **Section 9.1.1**. Interestingly, the co-injection with total injection rate of 1 cm^3/min *without* backpressure showed a different behavior compared to the co-injection with same injection rate *with* backpressure, cf. **Figure 33**. The differential pressures for the co-injection *without* backpressure is monotinically higher until it peaked at f_g=0.6. The higher differential pressure at gas fractions up to f_g=0.6 may be explained by the effects of gas compressibility: high gas velocities and frequent variations in lamellae shape and curvature can increase the local viscous pressure gradients and amplify local generation of foam (Nguyen, 2011).

The differential pressure across the fractured core increased with increasing gas fractional flow until a sudden drop a high gas fractional flow. The largest differential pressure for the lowest injection rate (1 cm^3/min) was observed for f_g=0.8 and demonstrated the highest relative increase in differential pressure from start to its peak (disregarding the baseline): a ~483% increase in differential pressure was observed when increasing the gas fractional flow from f_g=0.1-0.8. The foam generation experiment with a constant total injection rate of 2 cm^3/min was performed with a backpressure of 3.2 bar (~47 psi). The differential pressure across the fractured core increased with increasing gas fractional flow until a sudden drop at high gas fractional flow. The largest differential pressure was observed for f_g=0.8 and demonstrated the lowest relative increase in differential pressure from start to its peak: a ~279% increase in differential pressure was observed when increasing the gas fractional flow from f_g=0.1-0.8. The foam generation experiment with a constant total injection rate of 3 cm^3/min was performed with a backpressure of 4.2 bar (~62 psi). The differential pressure across the fractured core increased with increasing gas fractional flow until a sudden drop a high gas fractional flow. The largest differential pressure was observed for f_g=0.9 and demonstrated the second highest relative increase in differential pressure from start to its peak: a ~320% increase in differential pressure was observed when increasing the gas fractional flow from f_g=0.1-0.9. All backpressures were adequately high to suppress the adverse effects of gas compressibility: the differential pressure was distinctly improved, and the produced fluids were observed to have a stable and continuous flow.

Co-injections With Equal Backpressure

To enhance the comparability between the experiments they were redone with an equal backpressure of 3.6 bar (~53 psi). The only difference was that the experiment with a constant total injection rate of 3 cm^3/min was scaled down to a constant total injection rate of 2.5 cm^3/min, to ensure that contrast in differential pressure and system pressure/backpressure was sufficient to avoid any gas compressibility effects. Additionally, the measured gas fractions were changed from 10 to 7 steps to reduce experimental time. Subsequently, an experiment with decreasing gas fractional flow was conducted to investigate the effect of hysteresis on foam generation and differential pressure.

The differential pressure across the fractured core increased with increasing gas fractional flow until f_g=0.9 at all constant injection rates. **Figure 35** show that the maximum differential pressure was similar (~0.95±0.05 psi) for three injection rates (1, 2 and 2.5 cm^3/min) and that the differential pressure increased with increased injection rate. Which injection rate that has the most stable foam and the highest saturation of trapped gas can be evaluated by comparing each curve's decrease in differential pressure from its peak (f_g=0.9) to f_g=1.0. The lowest relative decrease in differential pressure (~7%) was observed with the lowest injection rate (1 cm^3/min). A 35% and 26% decrease was observed by 2 and 2.5 cm^3/min, respectively. Because the impact of viscous drag force increases with increased injection rate, it was anticipated that the lowest injection rate would result in the highest saturation of trapped gas and that the highest injection rate would result in the lowest. Mass transfer between flowing and trapped gas can slow the displacement of non-stationary bubbles and thus over-estimate the fraction of trapped gas bubbles if not accounted for (Kil et al., 2011). Thus, it is possible that steady state flow conditions was assumed too early, and that the differential pressure could have decreased even more if the co-injection would have lasted longer.

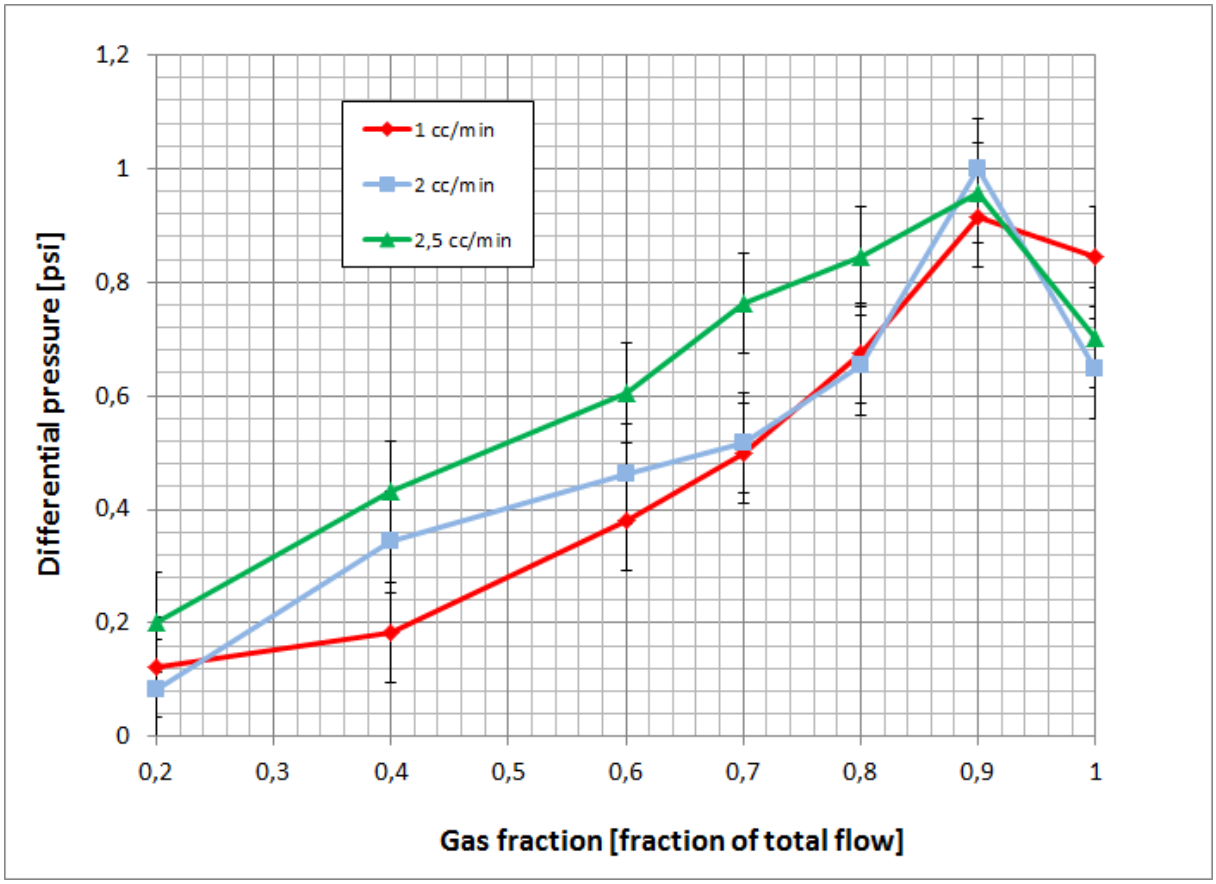

Figure 35: Differential pressure [psi] as a function of gas fraction during co-injection of surfactant solution and gas (air) using 3 constant total rates in the fractured 2-inch core. The curves reflect foam generation ability in the 2-inch fractured core at equal outlet conditions (identical backpressure) and different total injection rate. All curves are based on experiments conducted with an increasing gas fraction (f_g=0-1). Each point is an averaged value of every differential pressure logged in the time span each gas fraction was run. The gas fraction was changed when the differential pressure was stabilized. All total injection rates (1, 2 and 2.5 cm^3/min) show the similar/correlative behavior: increasing differential pressure with increasing fractional flow until a sudden drop at high fractional gas flow. The largest differential pressure was observed for f_g=0.9 for all injection rates.

Comparing the results in **Figure 34** and **Figure 35** shows that the maximum differential pressure is lower in the experiments with an equal backpressure than in the experiments with varied backpressure. The lack of a pressure build-up could be a consequence of reducing the measured gas fraction (from 10 to 7). In the experiments with varying backpressure, where all 10 gas fractions were run, the pressure build-up was evident, also for low gas fractions (<f_g0.5). Another interesting question is whether the maximum differential pressure peak at f_g=0.9 is a result of equal backpressure or reduced measured gas fractions. Kovscek et al. (1995) reports that a shift from polyhedral to cylindrical, hence stronger, foam occurs near gas fractions around f_g=0.9, which corresponds with the theoretical transition predicted by Princen (1983). Maximum flow resistance occurs near this transition, and is validated by the co-injections with equal backpressure. Simulations of foam in fractures with constant aperture and atmospheric outlet conditions showed that the finest foam texture (high flow resistance) occurs at gas fractions above f_g=0.9 (Pancharoen et al., 2012). The 1D linear fracture model

also assumed end-point relative permeabilities of 1 for both gas and water, hence excluding the influence of trapped water and gas saturations. Considering the rough-walled and complex fracture network of the 2-inch core used in this thesis, it is reasonable to suggest that foam may be generated differently than in smooth, constant fractures. Thus, the highest foam texture may occur at gas fractions different from previous studies, like in the co-injection with varying backpressure, where some differential pressures peaked at f_g=0.8. Additionally, Kovscek et al. (1995) states that the pressure drops for in-situ generate foams are less than pregenerated foam because foam generated in-situ are coarser than the pregenerated foam. Research by (Haugen et al., 2012) confirms that the differential pressure in fractures are higher for pregenerated foams than the foams generated in-situ. Increased total injection rate led to a higher starting pressure, but the peak in differential pressure seemed to be inconsequential on injection rate. This is consistent with the results of (Fernø et al., 2016), who reports that increased total injection rates led to a less steep and more stable increase in differential pressure, but that the pressure gradients of all injection rates peaked around the same value.

An experiment with decreasing gas fraction was conducted immediately after an experiment with increasing gas fraction under identical conditions (rate and backpressure). Unlike the two baseline experiments without backpressure, the core was not re-saturated (with surfactant solution, in this particular case). The aim was to investigate the effect of hysteresis on foam mobility and differential pressure. The result is presented in **Figure 36** below. During the experiment with decreasing gas fraction, foam with fine texture (strong foam) was observed in the transparent production tubing for all gas fractions that was run (except for f_g=1.0), and is likely the primary explanation to why the differential pressure remains high and stable despite the reduction in gas fraction. Additionally, the stable behavior of the differential pressure suggests that the changes in configuration of fluids in the fracture network as gas fraction decreases is insignificant. By not resaturating the core with surfactant solution before the experiment, a high gas saturation would remain in the core as the decreasing gas fraction co-injection commenced. This could potentially cause increased trapped gas saturation. Trapped gas saturations in carbonate rocks are reported to be substantial, varying from 23-68% of the total pore space (Keelan and Pugh, 1975). The scope of trapped gas saturation is also a function of initial gas saturation. In this particular case, the initial gas saturation was equal to the gas saturation after the co-injection with increasing gas fraction (f_g:0-1), and more gas is trapped after the co-injection with decreasing gas fraction (f_g=1-0), hence an increase in differential pressure. This is further confirmed when comparing these results to the experiments (block network) where the core was flushed and fully saturated with brine: less trapped gas (initial gas saturation) leads to a different and, in general, lower average in differential pressure. Subsequently, the hysteresis effect is less prominent when the core is flushed with surfactant solution prior to the decreasing gas fraction experiment, as the trends in differential pressure are more similar and comparable. The hysteresis effects observed in the fracture network and 2-inch core corroborates earlier work and documented experiences with foam generation by in-situ co-injection of surfactant solution and gas (Sanchez et al.,

1986). However, other researchers have reported absent effects of hysteresis (Persoff et al., 1991). Research by Yaghoobi (1994) suggested that one of the main parameters affecting hysteresis was type of surfactant used as a foaming agent. The overall roughness on the rock surface in the fractured core may lead to an effective advancing contact angle that differs from the receding angle, hence influencing contact-angle hysteresis. Substantial surface roughness and contact-angle hysteresis increase the pressure gradient required for mobilization considerably (Rossen, 1989).

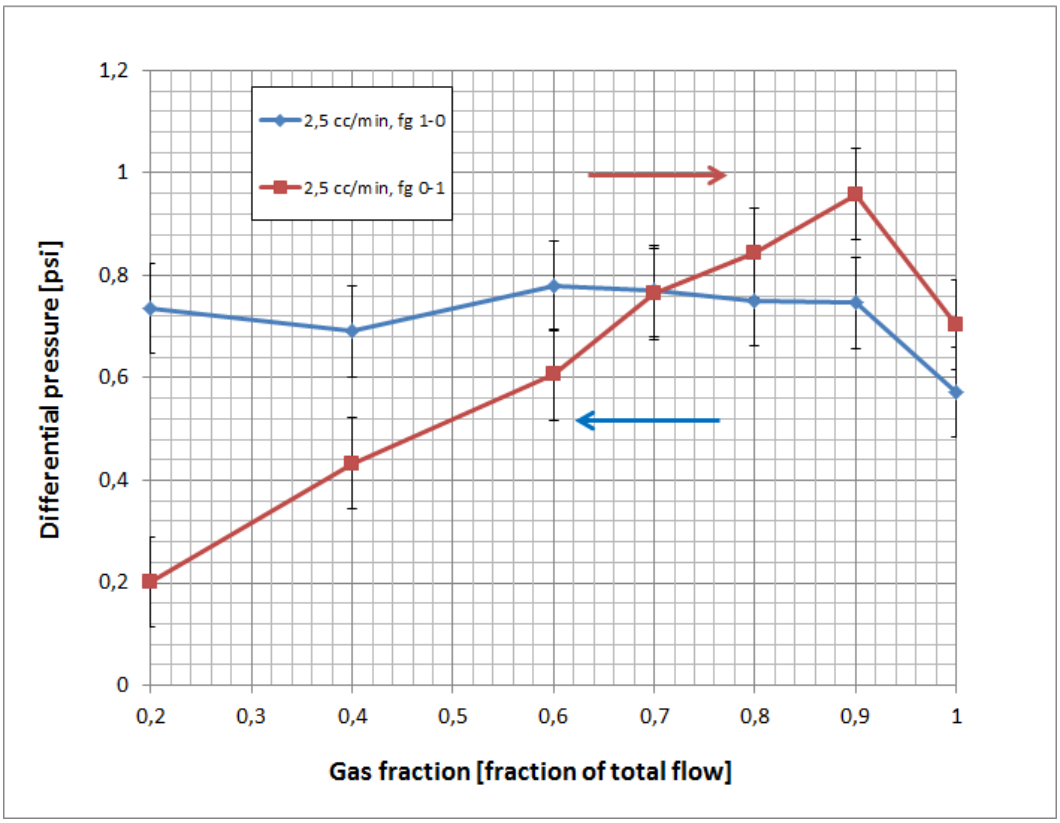

Figure 36: Differential pressure [psi] profile as a function of gas fraction for two experiment under identical conditions (rate and backpressure). Surfactant solution and gas was coinjected in both experiments at a constant total injection rate of 2.5 cm^3/min. f_g: 0-1 denotes increasing gas fraction and f_g: 1-0 denotes decreasing gas fraction. However, note that the experiments started and ended at f_g=0.2 and not f_g=0/f_g=1. Each pressure point in the curve is an averaged value of all the pressures that was logged during each gas fraction interval/sequence. The blue and red arrow represent whether the gas fraction is increasing or decreasing.

9.2 4-inch Fractured Marble Core

Co-injections of surfactant solution and gas (nitrogen) were performed to study foam generation in a 4-inch diameter fractured marble core saturated with surfactant solution. 2 experiments were conducted and foam generation was evaluated by analyzing the differential pressure as a function of gas fraction when injection rates and outlet pressure conditions were varied. The curves are obtained from lab partner Sigbjørn Aasheim Johansen. Experimental setup and procedures are elaborated in (Johansen, 2016).

Figure 37 shows the differential pressure as a function of gas fraction during co-injections of surfactant solution and gas (nitrogen). The core was fully saturated with surfactant solution prior to both co-injections, but backpressure and total injection rate was varied. The co-injection with 5 cm^3/min as constant total injection rate started at f_g=0.4 and was measured at every 0.1 gas fraction chronologically up to f_g=1. The co-injection with constant total injection rate of 8 cm^3/min started at f_g=0.4 and was measured at 0.6, 0.8, 0.9 and 1, chronologically. The foam generation experiment with a constant total injection rate of 5 cm^3/min was performed with a backpressure of 3.6 bar (~53 psi). Additionally, this particular co-injection was visualized using PET/CT. This will be further addressed in **Section 10.2** below. The differential pressure across the fractured core increased with increasing gas fractional flow until a sudden drop at high gas fractional flow. The largest differential pressure was observed for f_g=0.8 and demonstrated a relative increase in differential pressure from start to its peak of ~225%. The co-injection with a constant total injection rate of 8 cm^3/min was performed with a backpressure of 4.2 bar (~62 psi). As anticipated, the total injection rate of 8 cm^3/min started at a higher pressure gradient than 5 cm^3/min, which was observed for the first two measured gas fractions (0.4 and 0.6). However, when the gas fraction was increased from f_g=0.6 to f_g=0.8 the system pressure increased rapidly towards the same level as the drive pressure. If the contrast in drive pressure and system pressure was reduced too significantly, the mass flow controller would struggle to deliver the demanded gas rates. A decision was made to reduce the backpressure from ~62 to ~56 psi, hence the decline in differential pressure from f_g=0.6 to f_g=0.8. It is reasonable to assume that the trends in differential pressure would be more similar if not for this experimental error. The steeper decrease in differential pressure from f_g=0.9-1 for the co-injection with total rate 8 cm^3/min compared to 5 cm^3/min is expected because of the increased contribution of viscous drag/forces.

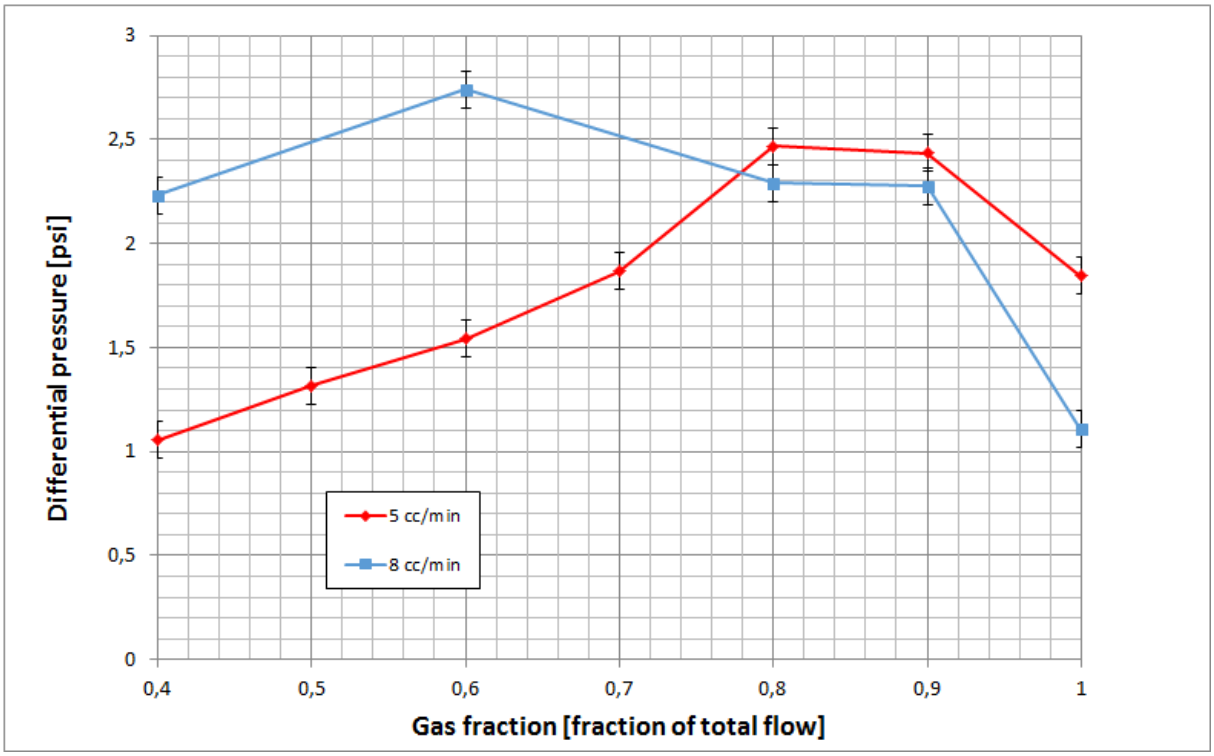

Figure 37: Differential pressure [psi] as a function of gas fraction during co-injection of surfactant solution and gas (nitrogen) using 2 constant total rates in the fractured 4-inch core. The curves reflect foam generation ability in the 4-inch fractured core at different outlet conditions (various backpressure) and different total injection rate. Both curves are based on experiments conducted with an increasing gas fraction. Each point is an averaged value of every differential pressure logged in the time span each gas fraction was run. The gas fraction was changed when the differential pressure was stabilized.

9.3 Fractured Block System

Two scenarios of foam generation of foam flow/propagation were investigated on a fractured block network/system (horizontally). The first set was based on a co-injection of surfactant solution and nitrogen gas with an increasing gas fraction (f_g: 0-1), and the second set was based on a similar co-injection with decreasing gas fraction (f_g: 1-0). Subsequently, the two scenarios were examined when the fractured block network was placed vertically in an identical experimental procedure. The following section describes the results from the foam generation by co-injection of surfactant solution and nitrogen gas.

Figure 38 shows the results from foam generation by co-injection of gas (nitrogen) and brine (1 wt% NaCl) in the fractured block system using a range of gas fractional flows (f_g: 0-1 and f_g: 1-0). The applied gas fraction was changed when the differential pressure measured across the network was stable. A total injection rate of 3 cm^3/min was used for all co-injections, and the fracture network was always initially water (brine) filled. Two different injections strategies were applied: increasing gas fraction and decreasing gas fraction, at two different scenarios: horizontal and vertical setup. In the experiments with increasing gas fraction, the differential pressure increased as gas fraction increased, and peaked at f_g=0.7 and f_g=0.9 for the vertical and horizontal setup, respectively, before it suddenly dropped. In the experiments

with decreasing gas fraction, the differential pressure increased as gas fraction decreased, and peaked at f_g=0.6 and f_g=0.7 for the horizontal and vertical setup, respectively, before it dropped. The higher differential pressure obtained at low gas fractions during injection with decreasing gas fraction (f_g:1-0), compared to injection with increasing gas fraction (f_g:0-1), makes it reasonable to assume that an injection strategy with decreasing gas fraction promotes the trapping of gas. The differential pressures with decreasing gas fractions spent more time stabilizing than co-injection with increasing gas fractions. The vertical experiments demonstrated an overall reduced differential pressure compared to the horizontal experiments for both increasing and decreasing gas fraction scenarios. This may be explained as reduced foam generation due to fluid segregation by gravity, hence inhibiting the mixing of gas and surfactant solution. At higher foam qualities, where the liquid fraction is small, there is not enough surfactant solution to maintain the lamella, and it is therefore more likely to coalesce. Additionally, liquid drainage of the lamellae by gravity is an adverse effect on foam stability and likely present in the vertical co-injections. To enhance foam stability, the foam can be regenerated by injecting slugs of liquid phase (Henry et al., 1996).

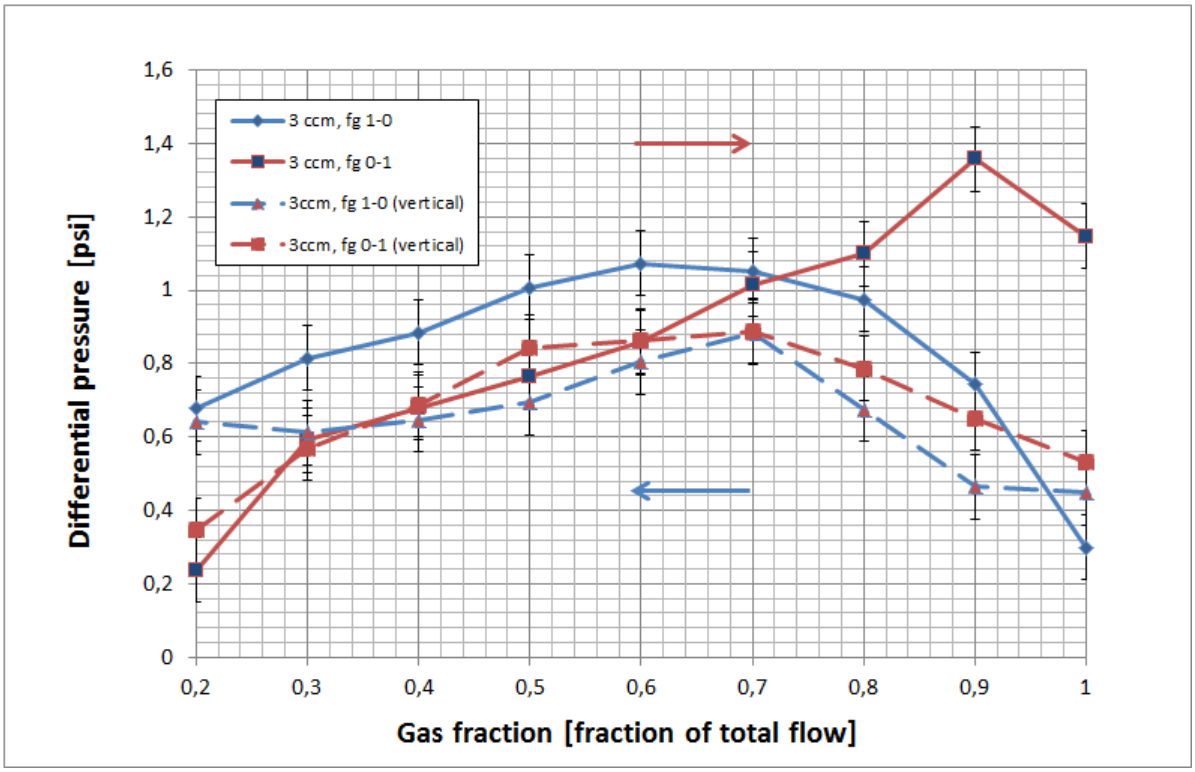

Figure 38: Differential pressure [psi] as a function of gas fraction during co-injection of surfactant solution and gas using a constant total rate of 3 cm^3/min in the fractured block network. Two main variations were made: sample orientation (horizontal or vertical) and injection strategy (increasing or decreasing gas fraction). The curves reflect foam generation ability in the fracture network at different injection strategies. The solid curves represent horizontal injections, and dashed curves represent vertical injections. Co-injections with increasing gas fraction (f_g:0-1) are shown in red, whereas results using decreasing gas fraction (f_g:1-0) are shown in blue. Each point represent an average value of every differential pressure recorded during each gas fraction. All curves show signs of similar/correlative behavior. In the experiments with increasing gas fraction the differential pressure increased as gas fractional flow increased until a sudden drop at high fractional gas flow. In the experiments with decreasing gas fraction the differential pressure increased as gas fraction decreased until a sudden drop. However, the maximum differential pressure seemed to occur in the same gas fraction region, independent of injection strategy or vertical/horizontal conditions. In the increasing gas fraction experiments the largest differential pressures was observed for f_g=0.9 (horizontal) and f_g=0.7 (vertical). In the decreasing gas fraction experiments the largest differential pressure was observed for f_g=0.7 (both horizontal and vertical). The blue and red arrow represent whether the gas fraction is increasing or decreasing.

Figure 39 below compares the pressure gradients [psi/ft] as a function of gas fraction for all fractured systems in a single plot. All curves show correlative behavior but differences in pressure gradient intensity, indicating that the generated foam had different foam texture. The observations of foam texture and pressure gradients were ambiguous: extremely small and finely textured foam was generated in the complex fracture network of the 4-inch core, indeed coherent with the large pressure gradient observed during the co-injection. The texture of the foam generated in the 4-inch core was much like the texture of foams generated in porous media, and was evident even at low gas fractions ($<f_g$=0.5). Bigger bubbles and less finely textured foam was observed in the fractured block network. Finally, the biggest bubbles, and thus least strong foams, were observed during the co-injections in the 2-inch fractured core. This emphasizes the necessity of variation in fracture aperture, intensity and roughness to generate strong foams in fractures. Based on the observation of foam texture, one would

expect that the pressure gradient of the fractured block network should be continuously higher than the pressure gradient of the 2-inch core. However, the results in **Figure 39** show the opposite. This may be explained as 1) the total injection rate during the co-injections on the block were not properly scaled to radius, and 2) the horizontal orientation of the block during co-injection may have influenced (mitigated) the contribution in pressure by gravity. The relative decline in pressure from peak to f_g=1 was ~49%, ~31% and ~64%, for the 2-inch, 4-inch and block network, respectively. Thus, the most stable foam was generated in the 4-inch core.

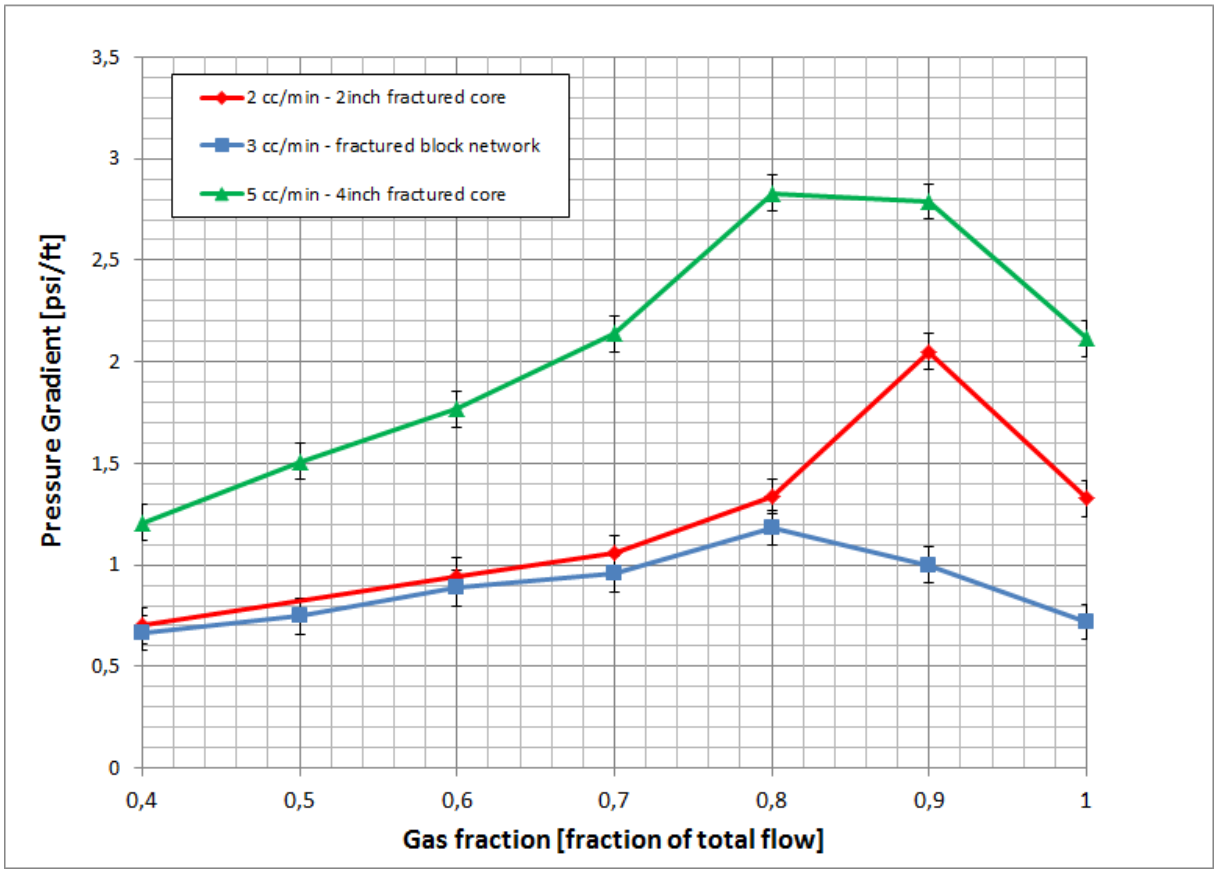

Figure 39: Pressure gradient [psi/foot] as a function of gas fraction during co-injection of surfactant solution and gas in 3 different fracture systems. The curves reflect foam generation ability in the fractured 2-inch, 4-inch and block at different outlet conditions and different total injection rate. All curves are based on experiments conducted with an increasing gas fraction. Each point is an averaged value of every differential pressure logged in the time span each gas fraction was run. The gas fraction was changed when the differential pressure was stabilized. All total injection rates show the similar/correlative behavior: increasing differential pressure with increasing fractional flow until a sudden drop at high fractional gas flow. The largest differential pressure was observed at f_g=0.9 for the 2-inch core, and f_g=0.8 for the 4-inch core and block.

10 Visualization of Foam Flow/Propagation in Fractures

Results presented so far in this thesis have proved that foam can be generated in the fractured systems presented and indicated the scope of trapped gas on fluid flow. Visualization techniques of fluid flow presented in this section give a unique insight into processes on the core and block scale. The usage of direct visualization enables for interpretation and accurate description of foam generation and displacement, and evaluate how these affect fluid distribution and fluid flow capacity.

10.1 Visualization of Foam Flow in The 2-inch Fractured Core Using PET/CT

An experiment involving ^{18}F as a nuclear tracer in the liquid surfactant solution during foam generation by co-injection was conducted at Haukeland University Hospital. The experiment was performed on the 2-inch fractured marble core and was digitally visualized using software processing and analysis. Information regarding the PET/CT process is briefly explained in **Section 1.5** (theory), and the experimental procedure is explained in **Section 7**. Liquid surfactant solution (labeled with ^{18}F) and nitrogen gas was coinjected into the fractured core with the purpose of generating foam in-situ. The objective was to perform an experiment where the gas fraction first increased from a low gas fraction to 100% gas injection (f_g=1), followed by a run with decreasing gas fraction back to the starting gas fraction. Due to the structure/organization of the PET imaging sequences, the visualization data and results in this section does not necessarily represent data obtained at stable pressure conditions. **Figure 40** shows *absolute* system pressure as a function of time, and indicates at what pressure and time intervals the imaging was obtained.

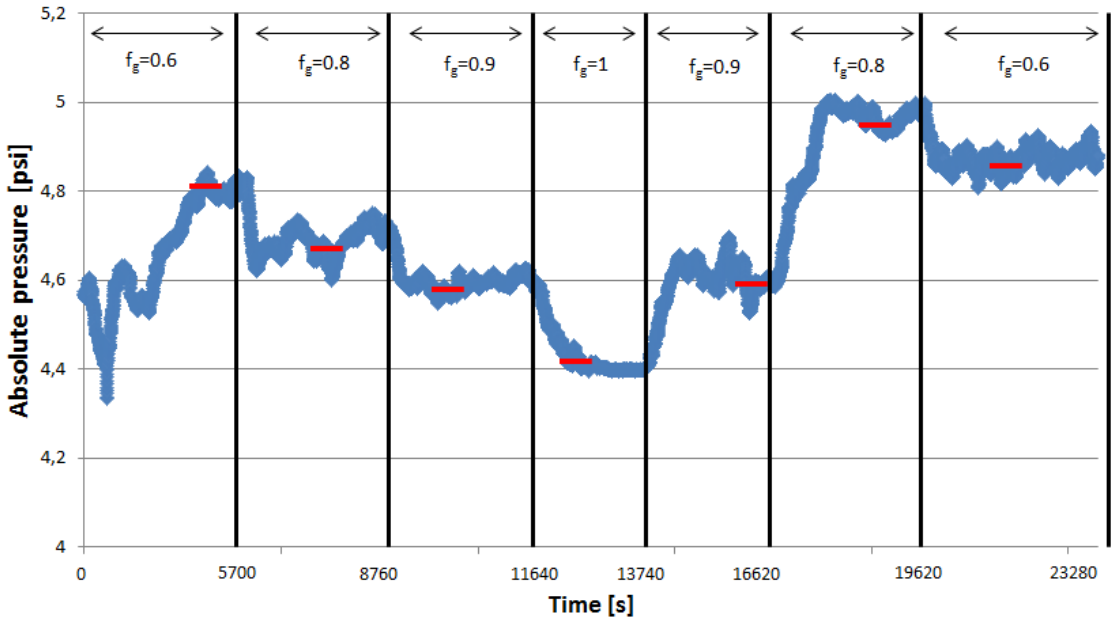

Figure 40: Absolute system pressure [psi] as a function of time. The vertical lines represent start/end of gas fraction, and the specific gas fractions are listed in the top of the figure. The red lines represent the pressure and time intervals where PET imaging of the system (2-inch fractured core) was obtained.

PET profiles as a function of the fractured core's normalized length (dimensionless position) were obtained at various times during the co-injection and are directly related to saturation of the labelled phase (in this work surfactant solution). This provides information about the fluid distribution in the fractures as gas fraction changes, and helps characterize in what fractures and at which gas fractions that promotes phase trapping/trapped saturations of either liquid and/or gas. Note that the CT resolution (the core material) is better than the PET resolution (surfactant solution). In some images, the liquid surfactant may therefore appear to be located in the rock matrix. This is, however, inconsistent with actual fluid distribution.

Figure 41 compares PET intensity as a function of normalized length for a single gas fraction (f_g=0.9) with increasing (blue) and decreasing (red) gas fraction. The curves can be compared to determine differences in fluid distribution in the fractures across the core. The higher the average surfactant saturation, the higher the detection (intensity) of the emitted photons. Five dimensionless positions have been defined as A, B, C, D and E, at which 2D XY-slices for each curve will be compared (cf. **Figure 42**) with normalized lengths of 0.06, 0.46, 0.59, 0.82 and 0.95, respectively. B, D and E has approximately the same surfactant saturation for both the increasing and decreasing gas fraction case, but the 2D XY-slices in B show local variations in fluid distribution (cf. **Figure 42**), contradictive to the PET profile. This may be explained as the trapped gas and foam changing the flow pattern of the liquid phase in the fractures so that it accumulates/concentrates in specific areas with favorable local capillary pressure gradients, and where the resistance to flow is least and. Subsequently, the initial saturation conditions prior the each of the runs were different, and are alone likely to sufficiently affect the fluid flow, and thereby fluid distribution. A and C has a higher average surfactant saturation during co-injection with decreasing gas fraction than increasing gas fraction, and the shape of the curve around C was different when comparing the co-injections. These observations indicate that not only is the saturation of liquid larger in these fractures for the co-injection with decreasing gas fraction, but, additionally it shows that in the region near C (X_D: 0.5-0.65), liquid appears to uniformly occupy fractures that was previously filled with a variation of fluids (foam, gas, liquid). Comparing the differential pressure at f_g=0.9 in **Figure 47** to the PET intensity in **Figure 41** show that the differential pressure is lower and that the PET intensity is slightly higher for the co-injection with decreasing gas fraction (26040 accumulated counts) relative to increasing gas fraction (25705 accumulated counts). This correspondence suggests that less foam has been generated in the co-injection with decreasing gas fraction (lower pressure) and thus a slightly higher liquid fraction is present, hence the higher average PET intensity throughout the core. Considering that the PET intensity is highly correlative, apart from regions X_D:0.15-0.25 (~37% increase in liquid saturation) and X_D:0.5-0.65 (~26% increase in liquid saturation (near C)), it is likely that the foam and/or trapped gas bubbles that constitutes the variation in differential pressure is located in these regions.

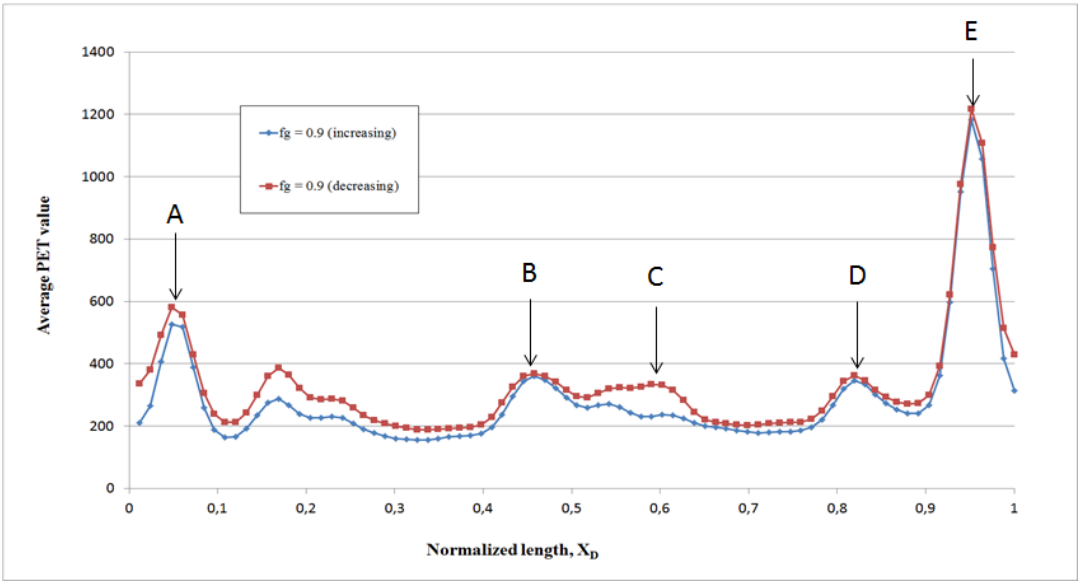

Figure 41: PET profiles for the 2-inch fractured core as a function of normalized length. Each point in the plot represents the average PET value for the respective dimensionless length fraction. High PET values reflect a high detection (high intensity) of emitted photons, whereas low PET values reflect a low detection (low intensity) of emitted photons. All values are obtained at the same gas fraction (f_g=0.9). However, the blue graph indicates values obtained as the gas fraction increases, whereas the red graph indicate values obtained as the gas fraction decreases. The letters A, B, C, D and E defines the normalized lengths at which the 2D XY-slices between PET profiles will be compared. The image montage in found in *Figure 42* below.

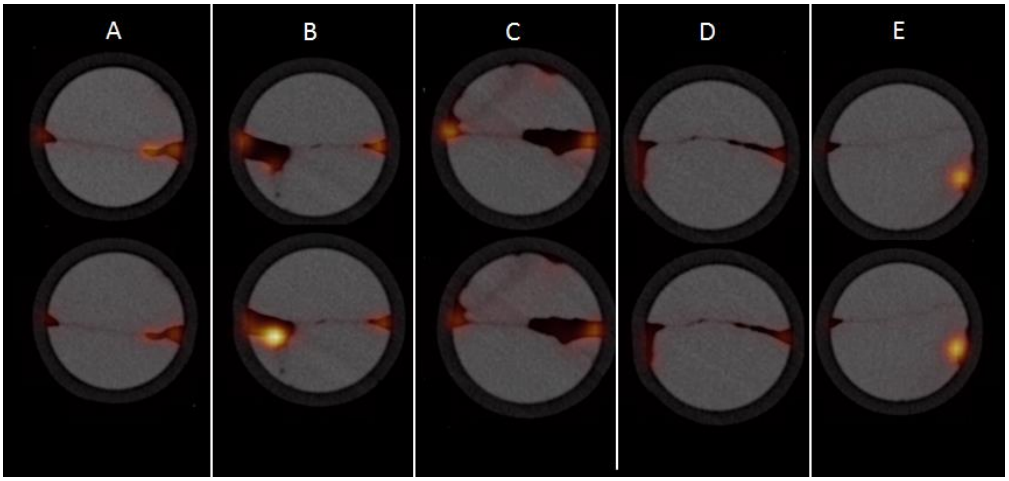

Figure 42: 2D XY-slices from the fixed normalized lengths defined as A, B, C, D and E. The labeled (radioactive) surfactant solution emits photons that the PET machine detects and processes as glowing colors: the brighter the glow, the higher the intensity of the emitted photons. This can be interpreted as fluid distribution in the fractures. The upper row represents 2D slices from the imaging sequence where the gas fraction increased, whereas the lower row represents 2D slices from the imaging sequence where the gas fraction decreased. The gas fraction was constant at f_g=0.9 for both imaging sequences.

Figure 43 compares PET intensity as a function of normalized length for a single gas fraction (f_g=0.6) with increasing (blue) and decreasing (red) gas fraction. Accumulated counts for the co-injections were 31970 (increasing gas fraction) and 27469 (decreasing gas fraction). Hysteresis effects can be observed with the overall difference in fluid distribution. Positions B and C has a higher surfactant saturation with increasing gas fraction compared with decreasing gas fraction. This can be also be observed by comparing the 2D XY-slices in **Figure 44**. Foam and/or trapped gas were presumably occupying these fractures, which used to be filled with a larger fraction of surfactant. Hence, the local pressure in these fractures was probably larger during co-injection with decreasing gas fraction compared to increasing gas fraction. A, D and E has a higher saturation of surfactant for the co-injection with decreasing gas fraction, and may be due to foam and/or trapped gas in fractures near regions B and C, diverting liquid surfactant to these fractures. Comparing the differential pressure at f_g=0.6 in **Figure 47** to the PET intensity in **Figure 43** show that the differential pressure is nearly equal (slightly lower), which is counter-intuitive, and will be discussed in more detail below. The high saturation of liquid near the outlet, observed both in **Figure 41** and **Figure 43**, indicate the well-known capillary end effect in coreflooding. Capillary end effects arise because of the discontinuity of capillarity in the wetting phase (liquid in this case) at the outlet end of the core sample (Huang and Honarpour, 1996). This discontinuity in capillary pressure tends to make it more difficult for the preferentially wetting phase to leave the core compared to the non-wetting phase. Thus, an accumulation of the wetting phase saturation near the end of the system is common in corefloods, which can significantly influence multiphase flow parameters such as the end-point relative permeabilities (Hadley and Handy, 1956). These effects occur commonly when the wetting fluid is being displaced by a non-wetting fluid in a core, like gas displacing water (for a water-wet rock). The high saturation, and thus high relative permeability of liquid (surfactant) near the outlet, is likely to contribute to a significant flow resistance to gas. The lack of decline in pressure from peak at f_g=0.9 to f_g=1 (shown in **Figure 47**) compared to previous research on fractured systems (Fernø et al., 2016), is probably due to this capillary end effect.

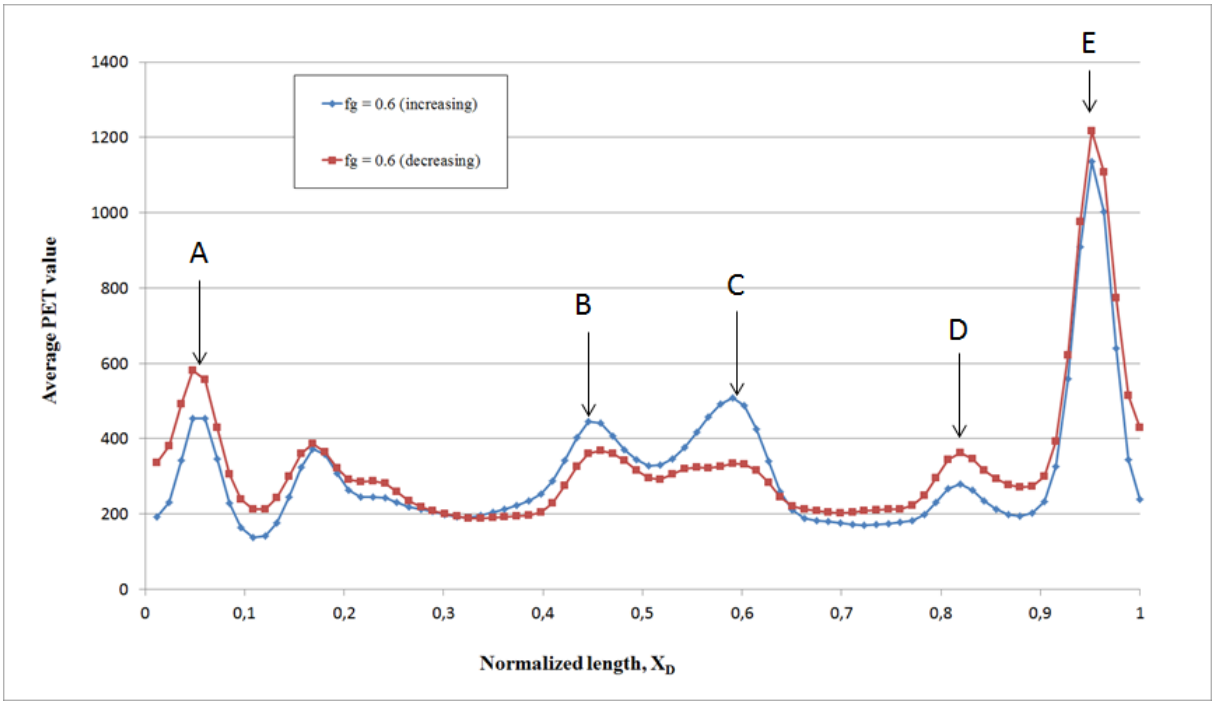

Figure 43: PET profiles for the 2-inch fractured core as a function of normalized length. Each point in the plot represents the average PET value for the respective dimensionless length fraction. High PET values reflect a high detection (high intensity) of emitted photons, whereas low PET values reflect a low detection (low intensity) of emitted photons. All values are obtained at the same gas fraction (f_g=0.6). However, the blue graph indicates values obtained as the gas fraction increases, whereas the red graph indicate values obtained as the gas fraction decreases. The letters A, B, C, D and E defines the normalized lengths at which the 2D XY-slices between PET profiles will be compared. The image montage in found in *Figure 44* below.

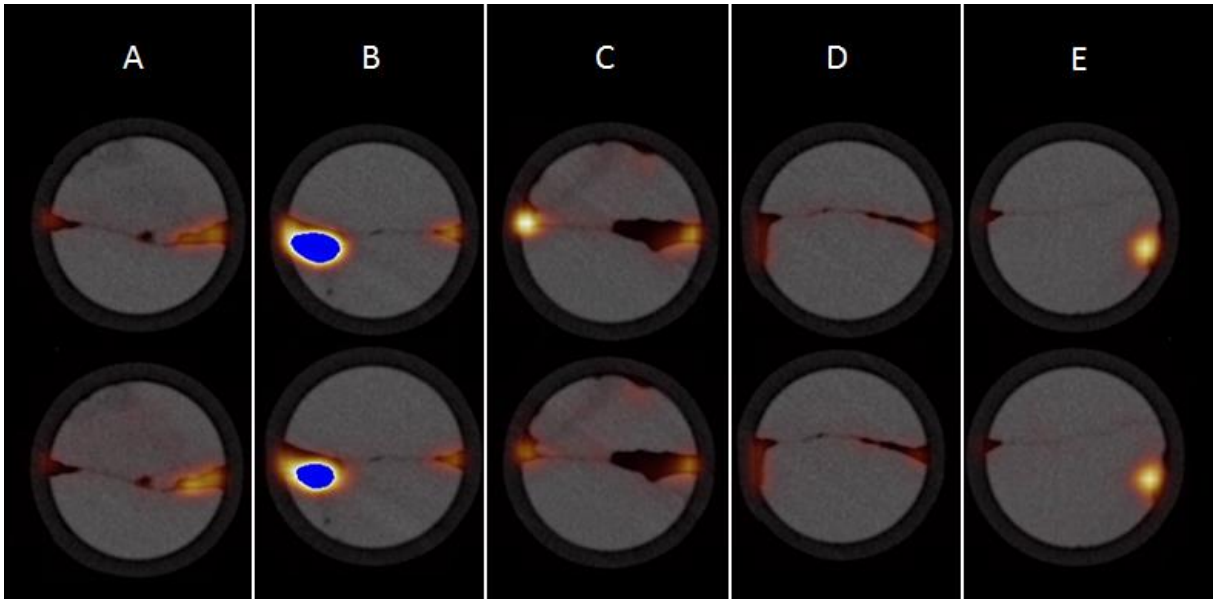

Figure 44: 2D XY-slices from the fixed normalized lengths defined as A, B, C, D and E. The labeled (radioactive) surfactant solution emits photons that the PET machine detects and processes as glowing colors: the brighter the glow, the higher the intensity of the emitted photons. This can be interpreted as fluid distribution in the fractures. The upper row represents 2D slices from the imaging sequence where the gas fraction increased, whereas the lower row represents 2D slices from the imaging sequence where the gas fraction decreased. The gas fraction was constant at f_g=0.6 for both imaging sequences.

Figure 45 displays the CT dryscan of the fractured core, consisting of 250 2D slices. The voxel sizes in each slice is 0.28 mm * 0.28 mm * 0,6 mm in x-, y- and z-direction, respectively. The PET images had lower resolution, with voxel sizes of 2mm * 2mm * 0.6 mm. From each PET sequence following images were obtained: a 3D image of the entire core (cropped), 5 2D XY-slices from different normalized positions and one 2D XZ (horizontal) cross-sectional slice from the center of the core along the entire core length (cf. **Figure 23**, **Section 8.1**). These images will be used to visualize and discuss the generation of foam and foam flow through the fractured core during the experiment.

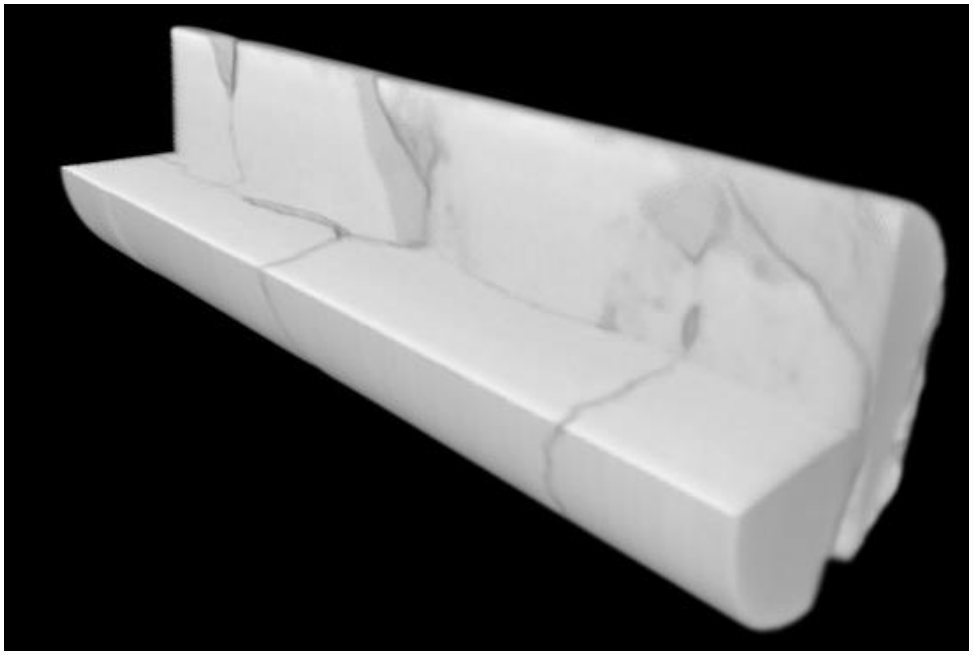

Figure 45: CT dryscan of the 2-inch fractured marble core used in the PET/CT experiment. During the dryscan the core was placed outside of the coreholder, and thus minimal interferes with the attenuation was measured, hence the image quality.

Figure 46 displays the PET signal from the fracture network at different time steps/gas fractions. The CT images are merged with the PET images to indicate where in the fracture network the fluids flow. Note that the 3D images are tilted 90 degrees for visualization purposes. A constant total injection rate of 2.5 cm^3/min was used throughout the experiment. The objective was to replicate the previous experiment with a constant total injection rate of 2.5 cm^3/min, where gas fraction first was increased and then decreased, without resaturating the core with surfactant solution. Because of the decay of the radioactive isotope ^{18}F in addition to the constraining timeframe at Haukeland University Hospital's PET lab, the number of gass fractions applied was reduced (from 14 to 8). The aim was to visualize foam generation and flow in addition to hysteresis effects. The backpressure was pressurized to 3.6 bar (identical to the other experiments), but due to a leakage (that was fixed before the experiment started) the pressure was ~3.2 bar during the co-injection. The system could not be repressurized due to lack of time. This may have influenced the foam generation ability, and hence the differential pressure, which will be discussed later. The experiment started at

f_g=0.6 and increased three times (0.8, 0.9 and 1, chronologically), before decreasing back at the same gas fraction steps (0.9, 0.8 and 0.6, chronologically). Gas fraction was changed when the differential pressure was stabilized. Note that the images in figure x does not necessarily visualize the flow at stable pressure conditions. It is evident that most of the flow occurs in the two largest fractures (highest transmissibility) which run parallel to the longitudinal axis regardless of gas fraction, but surfactant was also observed in less transmissible fractures. It is possible that foam has been generated in the highly transmissible fractures and diverted surfactant phase to other less transmissible fractures in the core. As expected, the liquid surfactant solution decreased as gas fraction increased. The image at f_g=1 suggest that most liquid is trapped in the highest conductive fractures, which is in line with the literature. It is interesting to see the difference in fluid distribution at the same gas fractions due to different injection strategy, cf. **Figure 46**. Trapped gas and hysteresis effects are believed to be one of the main factors controlling this difference in fluid distribution. As discussed earlier, initial gas saturations affect the extent of trapped gas saturations. Thus, with decreasing gas fractions (starting at f_g=1), it is likely that the fracture network would trap more gas than compared with increasing gas fractions. Comparing the fluid distribution during increasing gas fraction it is possible to observe the impact of trapped gas in the sense that the liquid surfactant solution was accumulating and distributed differently for the decreasing gas fraction case. It is especially evident when comparing f_g=0.6: the combined effects of an increased trapped gas saturation and foam is diverting liquid flow of surfactant solution into other fractures (cf. **Figure 42**, **Figure 44** and **Figure 46**). The blocking/diverting capacity of foam depends on not only the trapped gas fraction, but also on the pattern of foam displacement by liquid (Nguyen, 2011).

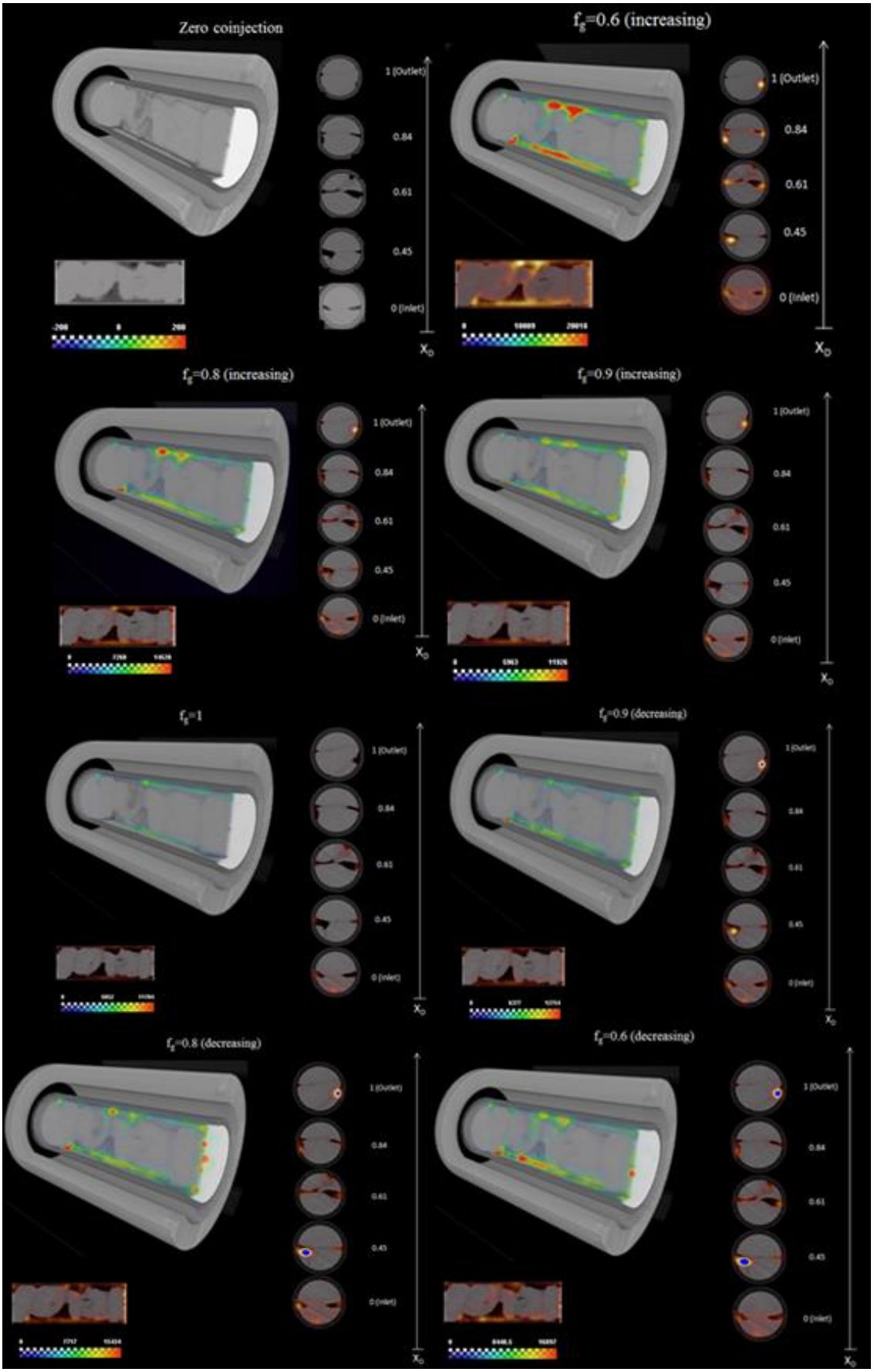

Figure 46: In-situ foam generation development in 2D (XZ-cross-section and XY-slices with normalized lengths) and 3D during co-injection of surfactant solution and nitrogen gas in the 2-inch fractured core. The surfactant is labelled with ^{18}F which emits radiation and is the only fluid that is possible to visualize in these images. The color specter in the lower left corner of each image indicates gamma intensity. Note that the 3D image is tilted approximately 90 degrees for visualization purposes. Larger individual images are found in *Appendix F*.

The differential pressure as a function of gas fraction, shown in **Figure 47**, display a different behavior compared to the experiment without imaging under identical conditions, cf. **Figure 36**. The differential pressure was overall lower in the PET/CT experiment. During the co-injections with increasing gas fraction, the peak in pressure occur at the same gas fraction (f_g=0.9) before declining for both experiments, although the differential pressure were ~67% lower in the PET/CT experiment. During the co-injection with decreasing gas fraction the differential pressure increased from f_g=1 to f_g=0.9, as expected. After the peak at f_g=0.9 the differential pressure was anticipated to remain stable as gas fraction decreased, assuming a considerable saturation of trapped gas. However, the differential pressure declined as gas fraction decreased, indicating either frequent foam coalescence or remobilization of trapped gas. Bubble shape and size of the foam is one of the main factors determining flow resistance of the system (Fernø et al., 2016). As mentioned earlier, bubble sizes of foam generated in fractures was 4 times larger compared to a porous media. Ettinger and Radke (1992) reports that smaller bubbles should result in larger pressure gradients and flow resistance. These observations make it reasonable to suggest that the average bubble size of trapped gas and foam at high gas fractions (>f_g=0.6) consist of large bubbles. Thus, the decline in differential pressure as gas fraction decrease may be explained as the frequent coalescence of large foam bubbles that previously occupied a considerable fraction of space in the fracture network.

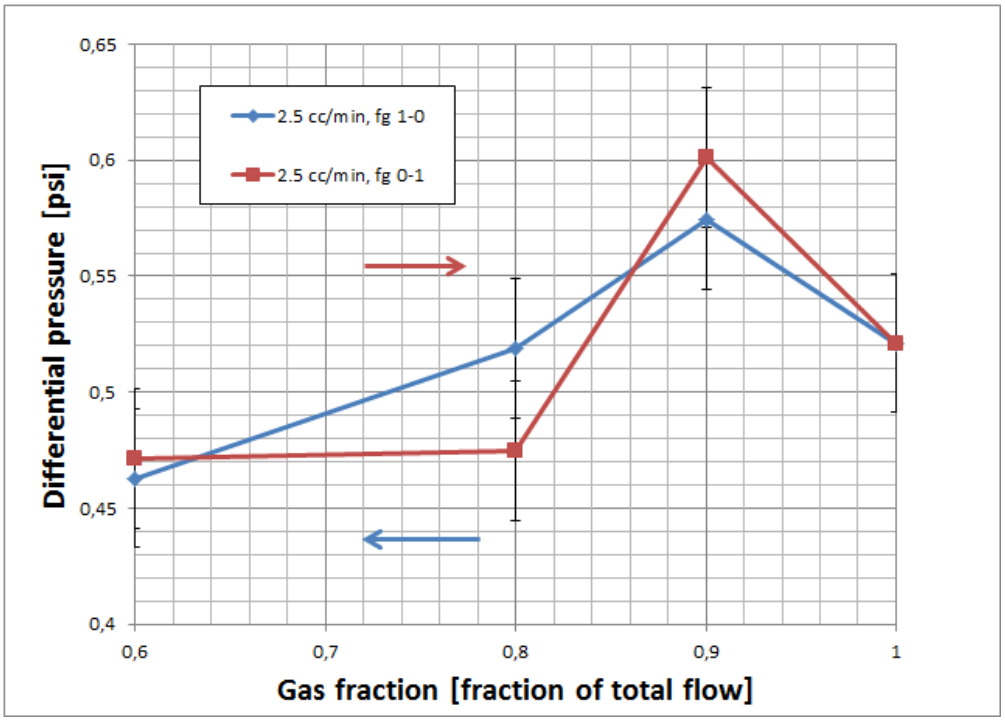

Figure 47: Differential pressure [psi] profile as a function of gas fraction for the PET/CT experiment at Haukeland University Hospital. Surfactant solution and nitrogen gas was coinjected at a constant total injection rate of 2.5 cm^3/min with a backpressure of ~3.2 bar. f_g: 0-1 denotes increasing gas fraction and f_g: 1-0 denotes decreasing gas fraction. However, note that the experiments started and ended at f_g=0.6 and not f_g=0/f_g=1. Each pressure point in the curve is an averaged value of all the pressures that was logged during each gas fraction interval/sequence. The blue and red arrow represent whether the gas fraction is increasing or decreasing.

The effects of hysteresis on pressure can be demonstrated by relating the differential pressure to the fluid distribution at different gas fractions and injection strategies (see **Figure 46**). For gas fractions 0.8 and 0.9, the total gamma intensity from the system (illustrated as the color specter with counts in each image in **Figure 46**) is higher for the co-injection with decreasing gas fraction (31970 and 26040 for f_g=0.8 and f_g=0.9, respectively) compared to increasing gas fraction (27489 and 25705 for f_g=0.8 and f_g=0.9, respectively), hence indicating a higher saturation of surfactant. At f_g=0.9, the surfactant solution is distributed differently, and can be observed as more concentrated in certain fractures, especially in dimensionless positions (2D XY-slices) 0.45 and 1 (outlet). The slightly lower differential pressure for the co-injection with decreasing gas fraction may be explained as less foam and more liquid surfactant phase. The effects of foam is more evident for f_g=0.8. From both the 3D representation and 2D XY-slices (increasing gas fraction), flow of surfactant is observed to divert from the highest transmissible fractures to less transmissible fractures. However, for the co-injection with decreasing gas fraction, it appears that flow favors one of the high transmissibility fractures, indicating that the surfactant has a higher resistance to flow in the other high transmissibility fracture, which can be validated with a higher differential pressure. The increase in differential pressure was possibly due to a combination of foam, hysteresis and trapped gas, which has altered the fluid distribution and changed the flow paths. Thus, surfactant solution has accumulated in different fractures during the co-injection with decreasing gas fraction compared to increasing gas fraction. Hysteresis effects are most prominent at f_g=0.6. This was the only gas fraction where total gamma intensity was larger for the co-injection with increasing gas fraction. The saturation of surfactant solution is overall significantly reduced, but it appears that the redistribution of fluids and trapped gas has led surfactant solution to preferentially flow in one of the high transmissibility fractures. Note that coalescence of a considerable amount of lamella may account for a certain (non-negligible) liquid saturation.

The substantial saturations of trapped gas is likely because of a high initial gas saturation (at f_g=1), and corroborates with other research (Keelan and Pugh, 1975). On the other hand, it is counter-intuitive that the differential pressure was slightly lower for the co-injection with decreasing gas fraction compared to increasing gas fraction, but less foam was observed in the transparent production tubing at the outlet during co-injection. Assuming the absence/negligible effects of gas compressibility, the difference in the foam generation ability between the PET/CT experiment and the results in **Figure 36** may be a consequence of differences in core orientation. The core was tilted 90 degrees and the two large parallel fractures in the longitudinal direction across the core were consequently changed from the core's vertical to horizontal axis. However, it is contradictive that the overall differential pressure is lower in the PET/CT experiment, assuming that the change in orientation mitigated the local gravitational effects on the foam stability (liquid drainage of lamellae films). Nguyen (2011) reports that when liquid is injected into a porous medium containing foam, the mobile bubbles are driven out which causes the pressure to drop. The gas contained in the trapped bubbles then slowly expands and may dissolve in the liquid, leading to a further decline of the pressure gradient. It is reasonable that similar behavior may be present in

fractures as well. This suggest that the overall lack of foam generation, combined with the redistribution of fluids due to hysteresis and increased liquid mobility as gas fraction decreased, may have increased the relative permeability of liquid (surfactant solution) in certain flow paths/fractures. Consequently, an increased viscous drag force on bubbles in these fractures may have contributed to the significant pressure drop from f_g=0.9 to f_g=0.6 during co-injection with decreasing gas fraction. Another explanation to the lack of foam generation may be that the rock surface has been alternated. It is likely that surfactants has adsorbed to the rock surface and smooth out surface roughness. Subsequently, numerous of co-injections consisting of water undersaturated on calcite may have absorbed calcite from the fracture surface in the core. Precipitation of calcite particles was observed in the production flask after multiple experiments, as shown in **Figure 48**. The combination of surfactant adsorption and absorption of calcite by the injected water may have alternated the fracture surface roughness, and thus possibly decreased possible snap-off sites. However, further investigation is needed to draw any conclusions.

Figure 48: Precipitation of calcite particles in the production flask. This was observed at the end of several experiments.

10.2 Visualization of Foam Flow in The 4-inch Fractured Core Using PET/CT

A PET/CT visualization experiment was conducted, identical to that described in **Section 10.1**. Liquid surfactant solution (labeled with ^{18}F) and nitrogen gas was coinjected into the 4-inch fractured core with the purpose of in-situ foam generating. Gas fraction was increased by 0.1 fractions from f_g=0.4 to 100% gas injection (f_g=1). The PET machine's field of view was constricted to ~16. cm, and the entire (stacked) core of 26.6 cm could therefore not be imaged. The chosen field of view is shown in **Figure 49** below.

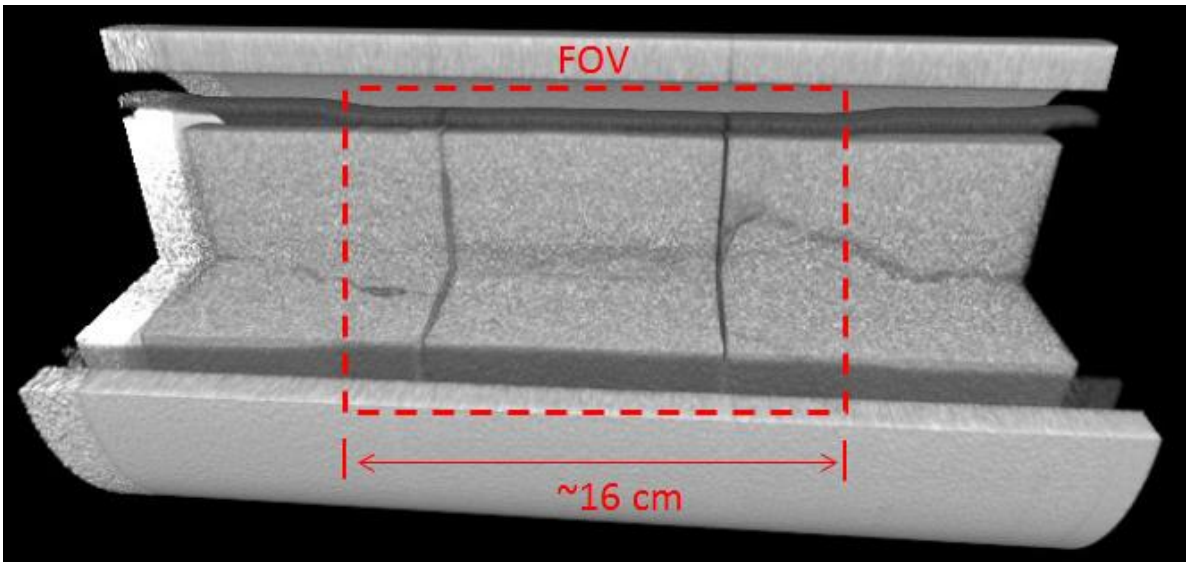

Figure 49: Field of view (16 cm) during PET/CT experiment. The entire core length was 26.6 cm. The field of view was fixed and determined to be placed at the area where fluid behavior was anticipated to be most complex.

Figure 50 and **Figure 51** displays the 2D XZ and 3D PET signal, respectively, from the fracture network at different time steps/gas fractions. The CT images is merged with the PET images to indicate in which fractures the fluids flow. The aim was to visualize foam generation and flow and investigate the effects of upscaling from 2-inch to 4-inch. A constant total injection rate of 5 cm^3/min was used throughout the experiment. Surfactant solution and nitrogen gas was coinjected into a fully surfactant-saturated core at a backpressure of 3.6 bar. The experiment started at f_g=0.4 and increased six times (0.5, 0.6, 0.7, 0.8, 0.9 and 1, chronologically. Gas fraction was changed when the differential pressure was stabilized. However, as mentioned in **Section 7**, the timing of the imaging was fixed, and does not necessarily visualize the flow at stable pressure conditions. Detailed experimental procedures are elaborated (Johansen, 2016). It is evident that most liquid flow occurs in the two largest fractures (highest transmissibility) which run perpendicular to the longitudinal axis regardless of gas fraction, but surfactant was also observed in less transmissible fractures. It is possible that these liquid pockets function as mixing zones for foam generation, and that foam bubbles propagates into smaller and less transmissible fractures. However, it is likely that the strongest foams (highest texture) are generated within the fractures of each core and not in the

two largest fractures ("stacking fractures), because of the enhanced surface roughness that provides more snap-off sites. The 3D model demonstrates foam's ability to mitigate gravity segregation by diverting and concentrating liquid flow in the vertical direction. This is especially evident in the "stacking fractures".

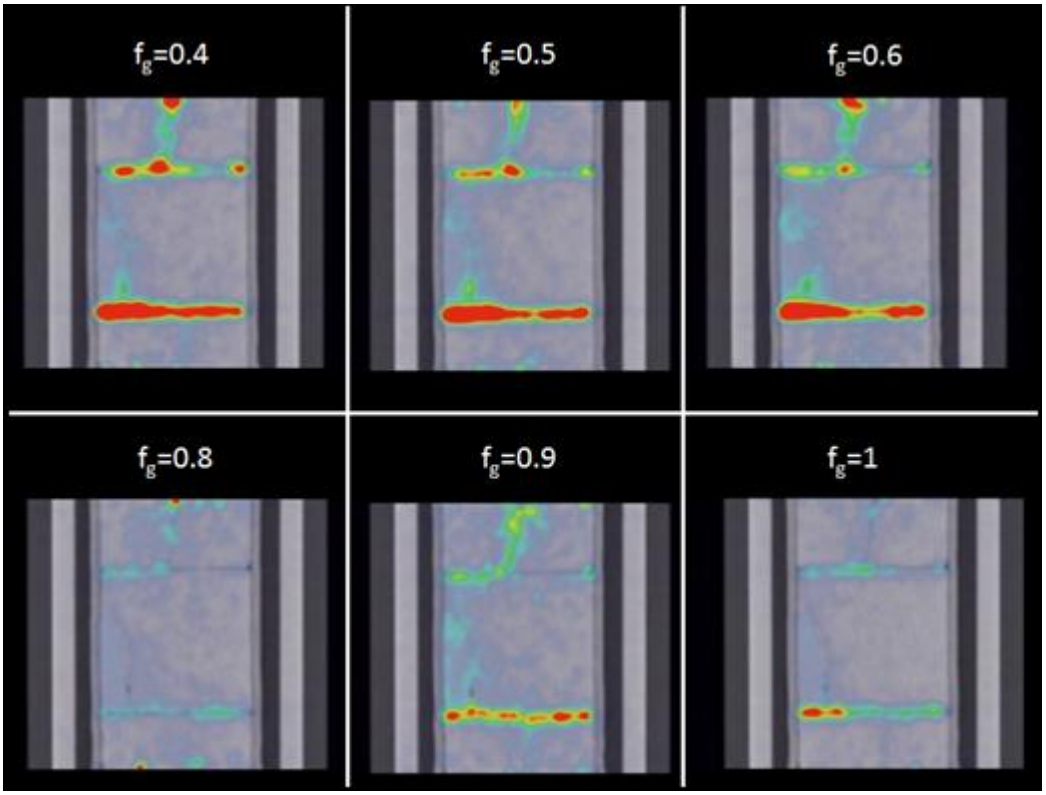

Figure 50: In-situ foam generation development in 2D (XZ-cross-section) during co-injection of surfactant solution and nitrogen gas in the 4-inch fractured core. The surfactant is labelled with ^{18}F that emits radiation and is the only fluid that is possible to directly visualize in these images. The warmer the color, the higher the saturation/concentration of surfactant solution. Note that f_g=0.5 and f_g=0.6 was obtained early in the gas fraction sequences.

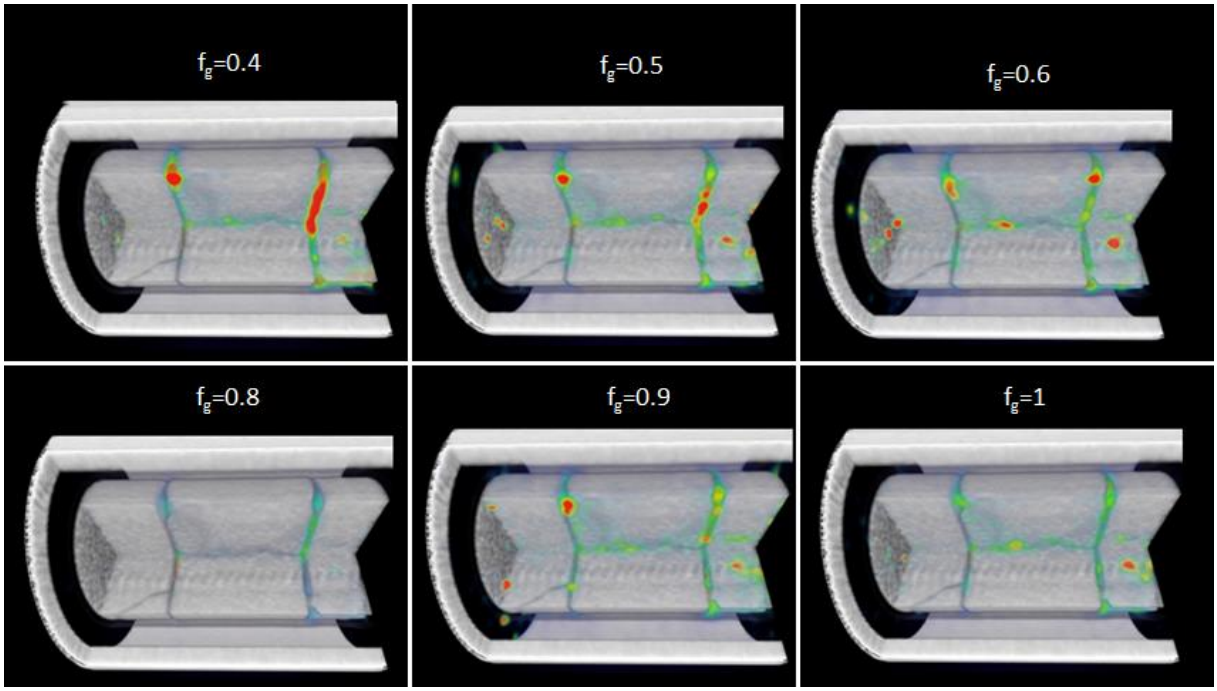

Figure 51: In-situ foam generation development in the 4-inch 3D model during co-injection of surfactant solution and nitrogen gas in the 2-inch fractured core. The surfactant is labelled with ^{18}F that emits radiation and is the only fluid that is possible to directly visualize in these images. The warmer the color, the higher the saturation/concentration of surfactant solution. Note that f_g=0.5 and f_g=0.6 was obtained early in the gas fraction sequences.

Differential pressure increase virtually linearly with gas fraction from f_g=0.4 to f_g=0.7, before a steep increase to f_g=0.8, where it peaks. The decline in pressure from f_g=0.8-0.9 is merely ~3.5%, indicating only small changes in foam texture and that the foam still remained stable. From f_g=0.9-1 the decline was ~27.5%. The observation of very small bubbles (fine foam texture) corroborates with the abated decline in differential pressure. Contrary to the 2-inch core where large foam and gas bubbles were observed at high foam quality (high gas fraction, ie. dry foam), the foam in the 4-inch core consisted of small bubbles. Thus, as high quality foam coalesces, the pressure declines less in the 4-inch core than the 2-inch core because of the (lower) difference in bubble size distribution. Interestingly, the saturation of liquid surfactant solution did not decrease gradually with increasing gas fraction, as observed for the 2-inch fractured core: Saturation of surfactant decreased from start (f_g=0.4) to f_g=0.8, before increasing again at f_g=0.9, and slightly decrease at f_g=1. This may seem counter-intuitive, but comparing the differential pressure, shown in **Figure 37**, to the fluid distribution shown both in **Figure 50** (2D) and **Figure 51** (3D) at f_g=0.8, suggests a large presence of foam.

10.3 Visual Inspection of Foam Flow/Propagation in Fractured Block System

Two scenarios regarding visualization of foam flow/propagation were investigated on a fractured block network/system (horizontally). The first set was based on a co-injection of surfactant solution and nitrogen gas with an increasing gas fraction (f_g: 0-1), and the second set was based on a similar co-injection with decreasing gas fraction (f_g: 1-0). Subsequently, the two scenarios were examined when the fractured block network was placed vertically in an identical experimental procedure. Foam generation during the co-injection process could be visualized and studied optically in both narrow and larger open space fractures. Local foam generation and propagation was studied during the injections. The foam structure (bubble size and shape) varied with gas fraction, in correlation with theory. Additionally, it was interesting to study mechanisms of foam stability and coalescence in detail. The following section describes the results from the visualization of foam flow/propagation.

Six sectors were defined, together with normalized length L, and used as reference points when evaluating foam propagation (see **Figure 52** below). Foam generation was observed during horizontal co-injection with increasing gas fraction 0.1-0.6. Predominantly bubble coalescence, and significantly less foam generation, was observed at gas fractions of 0.7-1.0. In the horizontal experiment where the gas fraction decreased foam generation was evident for all gas fractions (except f_g=1 and f_g=0.). In the vertical experiments, foam generation was observed from L=0 to L=1/2, and foam generation was reduced compared to the horizontal experiments. Fluid segregation due to density difference is most likely the predominant factor in the reduced foaming ability in this case. The injected gas will override the liquid surfactant solution which will flow along the bottom of the system, hence mitigating the mixing of gas and surfactant to generate foam. This is likely one explanation to why foam was generated from L=0 to L=1/2. The finest foam texture was generated in sectors 2-4 (around L=1/2) during co-injection with increasing gas fraction. For decreasing gas fraction, the finest foam texture appeared to be generated from L=1/2 to L=1 (ie. sector 4→sector 6).

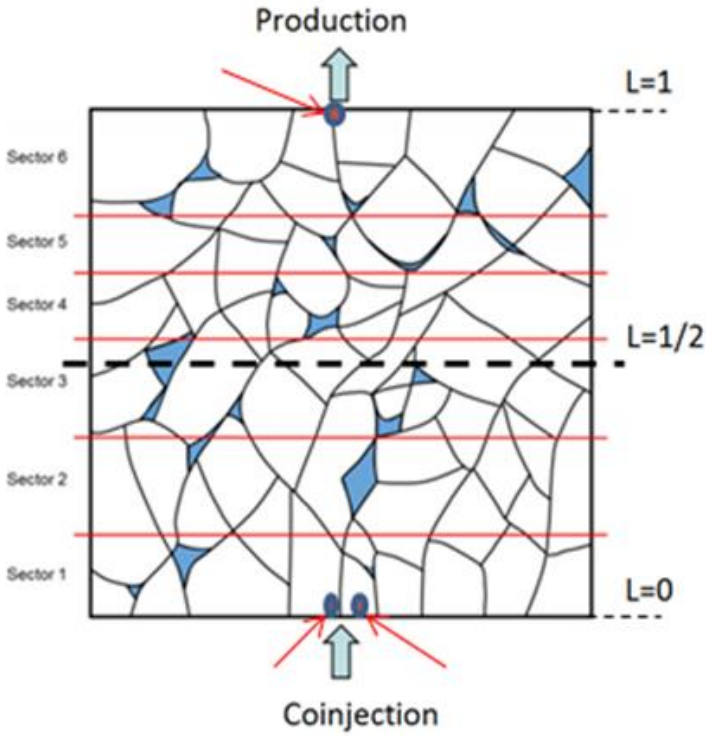

Figure 52: Schematic illustration of the fractured block network. To the left is a bird's perspective on the horizontal setup. The red arrows points at the co-injection-ports and the production port. The normalized length of the network is also defined, and used as a reference supplement to the six defined sectors when visually investigation foam generation. To the right is an illustration of the vertical setup. The fractured network was placed 90 degrees on the workbench, and the red arrows points at the co-injection- and production-ports, which are the same as in the horizontal setup. The red arrow that points at the middle-line indicate the height-equilibrium between the injection and production ports.

Figure 53 shows in-situ generated foam texture and bubble size in a large, open vug in the fractured marble block at two different gas fractions. Gas bubbles increased in size as gas fraction increased. Especially at gas fraction larger than f_g=0.7, coarsening in foam texture was evident, and the large gas bubbles are separated by thin lamellae. Subsequently, a larger distribution in bubble sizes was observed as gas fraction increased. This is consistent with earlier research on foam in fractures, where the bubble size increased with increasing gas fraction (Kovscek et al., 1995). However, previous studies on foam has shown that small bubbles should result in larger pressure gradients and flow resistance (Ettinger and Radke, 1992). This is counter-intuitive from the results of this particular visualization study, shown in **Figure 53**. An explanation is that foam with lower gas fractions is more mobile because of the availability of liquid surfactant solution, which thickens the lamellae separating gas bubbles and lubricates the rough fracture surfaces. Gas saturation was observed significantly lower in the smallest apertures, possibly due to capillary attraction of wetting surfactant solution. This corroborates with previous work on simulation in fractures (Pancharoen et al., 2012). Kovscek et al. (1993) reports of similar results in porous media, where the smallest pores are occupied solely by wetting fluid and the largest pores carry flowing foam. Hence,

bubble trapping occurred in the intermediate-sized and largest pore spaces. These observations were also made during co-injection in the fractured block network. In general, the ability of foam to propagate through the fracture network seemed to be independent of the geometrics and structure of the fracture network itself. However, foam generation was dependent on whether a minimum fluid saturation (gas and surfactant solution) was in the local fractures. In fractures where this critical saturation was reached (which could be visually determined because foam was being generated) foam had more similar flow behavior to gas than liquid.

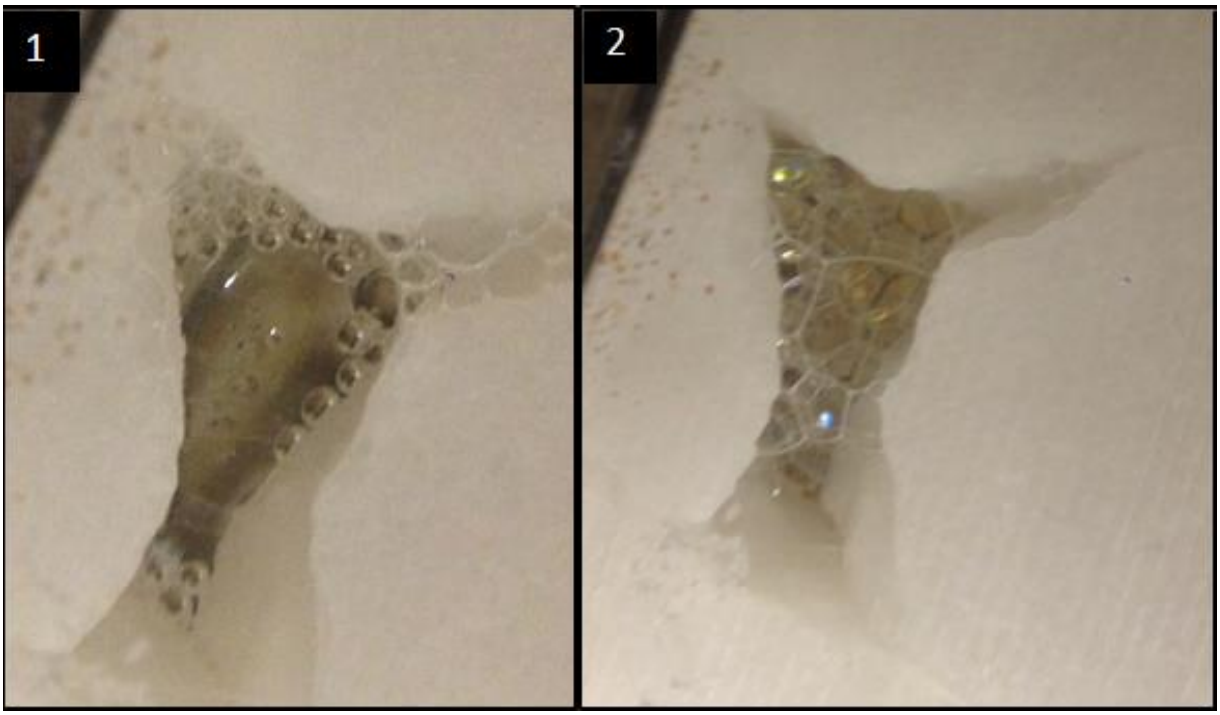

Figure 53: Close-up photo of bubble shape and distribution in an open space fracture in the fracture network. 1) A fine foam texture, and a low foam quality (f_g=0.4). This can be concluded because the bubble shapes are small and spherical. Additionally, the lamellae are observed to be relatively thick (high liquid fraction). It was also possible to observe some of the foam's stability criteria: gas diffusion was evident as larger bubbles grew on the expense of smaller ones, often referred to as foam coarsening in the literature. 2) The foam in this picture has a high gas fraction (f_g=0.8), large bubble shapes and a more coarse foam texture.

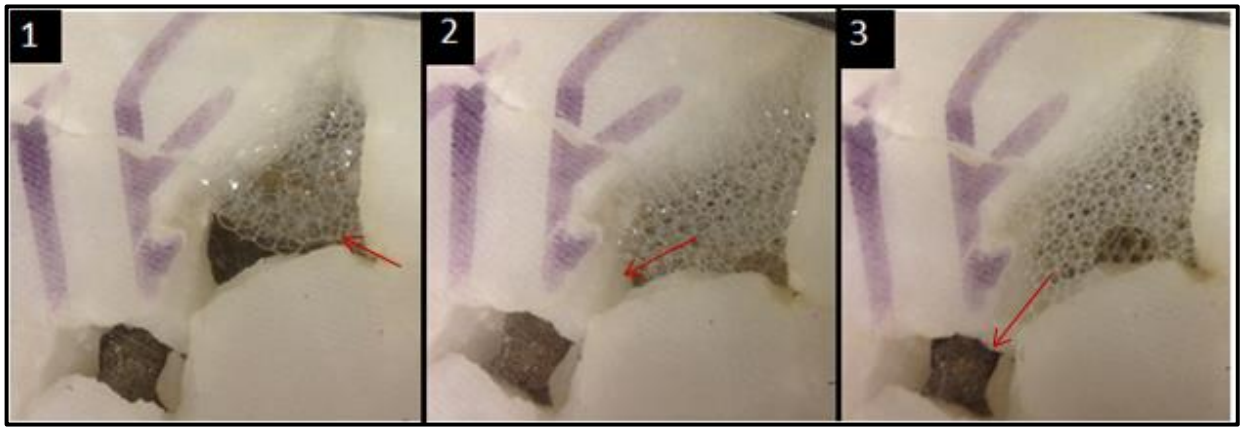

Figure 54: Close-up photo of foam propagation in an open vug in the fracture network during co-injection. The gas fraction was f_g=0.7 in all images. 1) The fracture has a saturation equal to or higher to than the minimum saturation of gas and surfactant to generate foam, and foam flow appears to have similar behavior to any other fluid. The red arrow indicate the direction of propagation. 2) Additional bubbles generate and almost occupy the open fracture. New foam was generated along the fracture surface and was pushed towards the center once new bubbles were created. 3) The open fracture is completely filled up with foam and the foam is now flowing towards new fractures where the pressure is lower. It is remarkably fascinating to see how the foam is structured, perfectly in line with theory.

Chapter IV – Conclusions and Future Work

11 Conclusions

Foam generation during co-injection in three differently scaled fractured systems was studied at various outlet conditions. The objective was to investigate which gas fractions and injection rates that favored the strongest foams under different outlet pressure conditions. Foaming ability was enhanced by initially saturating the systems with surfactant solution prior to co-injections. Our results indicate that surfactants has adsorbed to the rock surface, affecting co-injection quality/effectivity. Similar trends and behavior in differential pressure as a function of gas fraction, reflecting foam generation, was observed for all fracture systems: differential pressure increased as gas fraction increased, and peaked at a high gas fraction (as foam became dry) before a sudden drop. The highest relative increase in differential pressure, and thus strongest/finely textured foam was observed at f_g=0.8-0.9, produced by the lowest (relative) injection rates in all fracture systems. Despite the similar trends, it is likely that the variations in the fracture network geometry of the three fracture systems governed the main differences at which conditions the finest textured foams were generated. To assess the effects of upscaling on differential pressure, pressure gradients [psi/ft] as a function of gas fraction was plotted. The results were ambiguous: the finest textured foam was observed for the 4-inch core, fractured block network and 2-inch core, respectively. However, maximum pressure gradients of 2.83, 2.05 and 1.18 were demonstrated for the 4-inch, 2-inch and block, respectively. The total injection rate during the co-injections on the block were not properly scaled to radius for comparison with the 2- and 4-inch cores, and it is recommended to perform additional co-injections with increased total injection rate for a more accurate comparability. The results from the different fracture systems reflect the necessity of a complex fracture network to generate strong foams.

Adverse effects of gas compressibility on the balance between foam generation, stability and coalescence in experiments on the 2-inch fractured core led to an improvement of the experimental setup, where a backpressure was installed at the outlet end of the system. An adequately backpressure to reduce the effects of gas compressibility seemed to be key to maintain stable system conditions. Foam stability could be evaluated based on the relative decrease from pressure peak to end of co-injection (100% gas injection at f_g=1). Results from the co-injections suggest a negative influence of increased injection rates on foam stability. Higher injection rates increase the viscous drag, hence displacing non-stationary foam bubbles and thus a decline in pressure. The lowest relative decline (from peak to end) in differential pressure was observed by the co-injections with lowest (relative) total injection rate. Subsequently, factors such as the fraction of stationary bubbles/trapped gas and injection rate was believed to affect the rate of decline in pressure. Hysteresis was investigated in two of the fracture systems; the 2-inch core and the block network. Two main variations in the hysteresis experiments were made: 1) fully resaturating the core/network with surfactant solution (2-inch) or brine (block), and 2) no resaturation (2-inch). Effects of hysteresis regarding redistribution of fluids and trapped gas saturations were observed for both types of surfactant and in both fracture systems. The analyses validates the impact of initial gas saturation on trapped gas saturation in carbonate rocks reported in the literature.

Foam generation and flow/propagation was directly visualized in the fractured block network. Small foam bubbles with thick lamellae was observed at low gas fractions, and a coarsening of the foam occurred when gas fraction increased, hence drying the foam (thin lamellae). Additionally, foam generation by in-situ co-injection was visualized in the 2- and 4-inch fractured cores using PET/CT visualization techniques. The experiments provided imaging of local surfactant distribution within the fracture networks. The extent of foam generation, stability, coalescence together properties associated with foam such as blocking and fluid diversion could be interpreted from the correlation between differential pressure and PET/CT imaging. On the 4-inch core, gas fraction was increased during co-injection, whereas gas fraction was both increased and decreased during co-injection on the 2-inch. Our results suggest a substantial saturation of trapped gas, presumably due to a considerable gas saturation prior to the co-injection with decreasing gas fraction.

12 Future Work

Based on the presented results, discussions and conclusions, several extensions to the work in this thesis should be considered. Some of the following suggestions propose potential improvement to the experimental procedure used in this thesis, whereas others are plans for continuation on this work.

- To increase reproducibility of the data, a proper cleaning procedure should be considered to ensure minimal or no retention of surfactants. For optimal core recovery/preservation, Nguyen (2011) recommends flushing the core with at least 200 pore volumes/fracture volumes of distilled water in the presence of 40% ethanol. After flushing, remaining surfactant is removed using a cleaning mixture of chloroform, methanol and distilled water. Finally, the core is dried in an oven at 100 ^{o}C.

- The foam generation results demonstrated the importance of a complex fracture network in order to generate finely textured (strong) foam. Making more complex fracture networks can be created by crushing the cores to a greater extent, in addition to stacking.

- Elevated system pressure and temperature should be considered to replicate reservoir conditions. The core holder can be placed in a heating cabinet to achieve high temperatures analogous to reservoir temperature.

- At some point, oil should be introduced to investigate the aspects of oil recovery by foam in fractures, together with foam stability in the presence of oil.

- To learn more about the effects of hysteresis, experiments involving micromodels should be considered. This provides unique visualization of differences in fluid distribution and flow behavior. Variation in bubbles size distribution according to changes in gas fraction and the bubble size distribution of trapped gas are areas of interest.

- This thesis has focused on *qualitative* characterization of fractures, and paved way for a more quantitative approach in further work. Quantifying fracture aperture and intensity can provide a better utilization and discussion of the PET/CT-data (fluid flow and distribution). Subsequently, the PET/CT experiment for the 2-inch core should be reproduced to obtain a higher level of comparability in differential pressure to previous co-injections.

- On a longer time-perspective, when more experimental data has been quantified, a further upscale using numerical simulation should be considered.

Chapter V – Appendix and References

Appendix A – Uncertainties and Calculations

This appendix presents the calculations of uncertainties used in this thesis based on "Måling og behandling av måledata" by (Erdal, 2013).

Independent variables, *x, y, z, …, i* have arithmetic means $\bar{x}, \bar{y}, \bar{z}, \ldots, \bar{\imath}$. For a data set with *N* measured values that has produced the results $x_1, x_2, x_3 \ldots, x_N$, the arithmetic mean value $\bar{x}$ can be estimated as:

$$\bar{x} = \frac{x_1 + x_2 + x_3 + \cdots + x_N}{N} = \frac{1}{N}\sum_{i=1}^{N} x_i \tag{A1}$$

In general, a calculated value acquires the uncertainty from all input parameters. If a value *R* is calculated by either addition or subtraction of independent variables *x, y, z, …, i*, where each independent variable provides an additional uncertainty $S_x, S_y, S_z, \ldots, S_i$, then the accumulated uncertainty for the calculated variable *R*, S_R, can be estimated as:

$$S_R = \sqrt{(\frac{\delta R}{\delta x}S_x)^2 + (\frac{\delta R}{\delta y}S_y)^2 + (\frac{\delta R}{\delta z}S_z)^2 + \cdots + (\frac{\delta R}{\delta i}S_i)^2} \tag{A2}$$

If a value R is calculated either as a quotient or product of the independent variables *ax, by, cz, …, ni*, given that *a, b, c, …, n* are constants and *x, y, z, …, i*, are the independent variables, and each independent variable provides an additional uncertainty $S_x, S_y, S_z, \ldots, S_i$, then the accumulated uncertainty for the calculated variable *R*, S_R, can be estimated as:

$$\frac{S_R}{R} = \sqrt{(a\frac{S_x}{x})^2 + (b\frac{S_y}{y})^2 + (c\frac{S_z}{z})^2 + \cdots + (n\frac{S_i}{i})^2} \tag{A3}$$

A total uncertainty estimate of an experiment is generally a combination of uncertainty related to the instruments and uncertainty related to the experiment itself. Instrumental uncertainties are determined by the precision of the instrument in use. These errors are related to how well the instrument is calibrated and can be calculated using the listed equations above. All instrumental uncertainties in this thesis are listed in **Table A1** below. Experimental uncertainties are generally determined by errors that afflict experimental measures and is more difficult to quantify and less obvious. Examples may include the precipitation and adsorption of surfactant (retention) in the fractures, which can prevent the core or fractured block network to establish native conditions, undetected leakages and direct mistakes made by the observer. It is reasonable to assume that systematic experimental errors are larger than the calculated instrumental uncertainties. Hence, thoroughness in the experimental procedure

cannot be over emphasized, and is an essential part in the scientific approach in order to improve statistical quality of experimental data.

Table A1: Instrumental uncertainties of the measuring instruments used in this thesis.

Instrument	Parameter	Uncertainty	Unit
Weight	Mass	± 0,02	gram
Caliper	Length	± 0,02	millimeter
Pressure transducers	Pressure	± $6*10^{-3}$	bar
Syringe Pump	Flow rate	± 0,2%	ml/h
	Volume	± 0,2%	-
	Pressure	± 0,2%	-
Bronckhorst MFC	Rate	± 0,02%	cm^3/min

Appendix B – Experimental Overview

The collaboration partner for every experiment performed as a part of the experimental work reported in this thesis is listed in **Table A2** below.

Table A2: Overview of the collaborating partner during the experiments reported in this thesis.

Fracture System	Fluids in co-injection		Setup	Collaborating partner (initials)
	Surfactant	Gas		
Fractured block network	Petrostep C1	Nitrogen	Figure x	SAJ[7]
Fractured block network	Petrostep C1	Nitrogen	Figure x	SAJ
Fractured block network	Petrostep C1	Nitrogen	Figure x	SAJ
Fractured block network	Petrostep C1	Nitrogen	Figure x	SAJ
2i-1	-	Compressed Air	Figure x	SAJ
2i-1	-	Compressed Air	Figure x	SAJ
2i-1	-	Compressed Air	Figure x	SAJ
2i-1	LS22-24	Compressed Air	Figure x	SAJ
2i-1	LS22-24	Compressed Air	Figure x	SAJ
2i-1	LS22-24	Compressed Air	Figure x	SAJ
2i-1	LS22-24	Compressed Air	Figure x	SAJ
2i-1	LS22-24	Compressed Air	Figure x	SAJ
2i-1	LS22-24	Compressed Air	Figure x	SAJ
2i-1	LS22-24	Compressed Air	Figure x	SAJ
2i-1	LS22-24	Compressed Air	Figure x	SAJ
2i-1	LS22-24	Compressed Air	Figure x	SAJ
2i-1	LS22-24	Nitrogen	Figure x	None
2i-1	LS22-24	Nitrogen	Figure x	None
4i-3S	LS22-24	Nitrogen	Figure x	SAJ[8]
4i-3S	LS22-24	Nitrogen	Figure x	SAJ

[7] Sigbjørn Aasheim Johansen
[8] This experiment was conducted single-handedly by Sigbjørn Aasheim Johansen

Appendix C – Nomenclature

E_D	Microscopic displacement efficiency
E_{vol}	Volumetric sweep efficiency
E_R	Total recovery factor/Overall displacement efficiency
M	Mobility ratio
λ	Mobility
k_r	Relative permeability
μ	Viscosity [Pa*s]
σ	Interfacial tension [J/m^2]
P_c	Capillary pressure [Pa]
p_{nw}	Pressure in the non-wetting phase [Pa]
p_w	Pressure in the wetting phase [Pa]
ρ	Density [kg/m^3]
g	gravitational constant [m/s^2]
h	Height [m]
θ_{ij}	Contact angle between phases i and j [angle degree]
r	Pore throat radii [mm]
N_{vc}	Capillary number
u_w	Fluid velocity of water [m/s]
F^{18}	Fluorodeoxyglucose
τ	Shear stress [Pa]
τ_y	Yield stress [Pa]
Δp_f	Differential pressure of foam [Pa]
Δp_g	Differential pressure of gas [Pa]
f_g	Gas fraction [fraction of total flow]
Q	Flow rate [m^3/s]
V_b	Bulk volume [ml]
D	Diameter [cm]
L	Length of core [cm]
π	Mathematical constant pi
m_{sat}	Mass of saturated core plug [g]
m_{dry}	Mass of dry core plug[g]
X_D	Normalized/Dimensionless length

Appendix D – Abbreviations

IFT	Institutt for fysikk og teknologi
UiB	Universitetet i Bergen
HUH	Haukeland University Hospital
IOR	Increased oil recovery
EOR	Enhanced oil recovery
CT	Computed tomography
PET	Positron emission tomography
1D	One-dimensional
2D	Two-dimensional
3D	Three-dimensional
FS	Full scale
FDG	Fluorodeoxyglucose
CMC	Critical micelle concentration
CDC	Capillary desaturation curve
NCS	Norwegian continental shelf
CO_2	Carbon-dioxide
MRF	Mobility reduction factor
GOR	Gas-oil ratio
FAWAG	Foam-assisted water-alternating gas injection
USD	The United States dollar
M	Million
US	United States
POM	Polyoxymethylen

Appendix E - Additional Theory

This appendix consist of additional theory that was not necessarily directly related to topics, results and/or discussion presented in this thesis. However, it helps the reader obtain a comprehensive perspective which underlies the research conducted in this work. Note that the sections presented in this appendix is supposed to function as theoretical supplement for the reader - if needed. Thus, each section may be reviewed individually, and they have no relevant sequential context.

AE.1 Capillary Pressure

In a reservoir at initial conditions, there exists a force equilibrium between buoyancy, which separate the fluids according to their density, and capillary forces (Zolotukhin and Ursin, 2000). These forces determine the initial fluid distribution, and hence the volumes of fluid initially in place. The presence of interfacial tension at the contact surface between two immiscible fluids causes a differential pressure between the wetting phase and the non-wetting phase across the entire contact surface, defined as capillary pressure (Donnez, 2007). This can be mathematically expressed as:

$$P_c = p_{nw} - p_w \tag{A4}$$

where p_{nw} [Pa] is the pressure of the non-wetting phase and p_w [Pa] is the pressure of the wetting phase. Capillary pressure is a result from interactions of forces (force imbalance) acting within and between liquids and their bounding solids. These forces include liquid-liquid forces (cohesive) and liquid-solid forces (adhesive) (Zinszner and Pellerin, 2007). Capillary pressure can also be directly related to the height of the interface between two immiscible fluids above the level at which the capillary pressure is zero, meaning that the capillary pressure is in equilibrium with the fluid gravity:

$$P_c = (\rho_i - \rho_j) g h \tag{A5}$$

where ρ_i [kg/m^3] is the density of phase i and ρ_j [kg/m^3] is the density of phase j, g [m/s^2] is the gravity constant, and h [m] is the height.

When oil migrates into a water-wet and water filled reservoir (drainage process), the oil must overcome a certain capillary threshold pressure in order to displace the water filled pores. Oil will therefore migrate into the biggest pores first (requires lower capillary pressure). A normal fluid distribution in a water-wet reservoir will have the smallest pores filled with water and the biggest pores filled with oil with water films along the pore wall. When water is injected into a water-wet reservoir for IOR/EOR purposes, the water films will thicken and swell

around the oil to form a collar. Eventually, at a certain capillary pressure, the water will snap off in the pore throat and recede/withdraw to the center of the pore, making the oil phase discontinuous and capillary trapped, prohibiting the flow of water and thereby effectively reducing the relative permeability of water. The immobile and capillary trapped oil (residual oil saturation) prevents the imbibition process to reach the same water saturation prior to the drainage process. This saturation difference is commonly known as hysteresis, and affects important reservoir parameters including relative permeability, capillary pressure and fluid distribution (Ahmed, 2010, Zolotukhin and Ursin, 2000, Donnez, 2007).

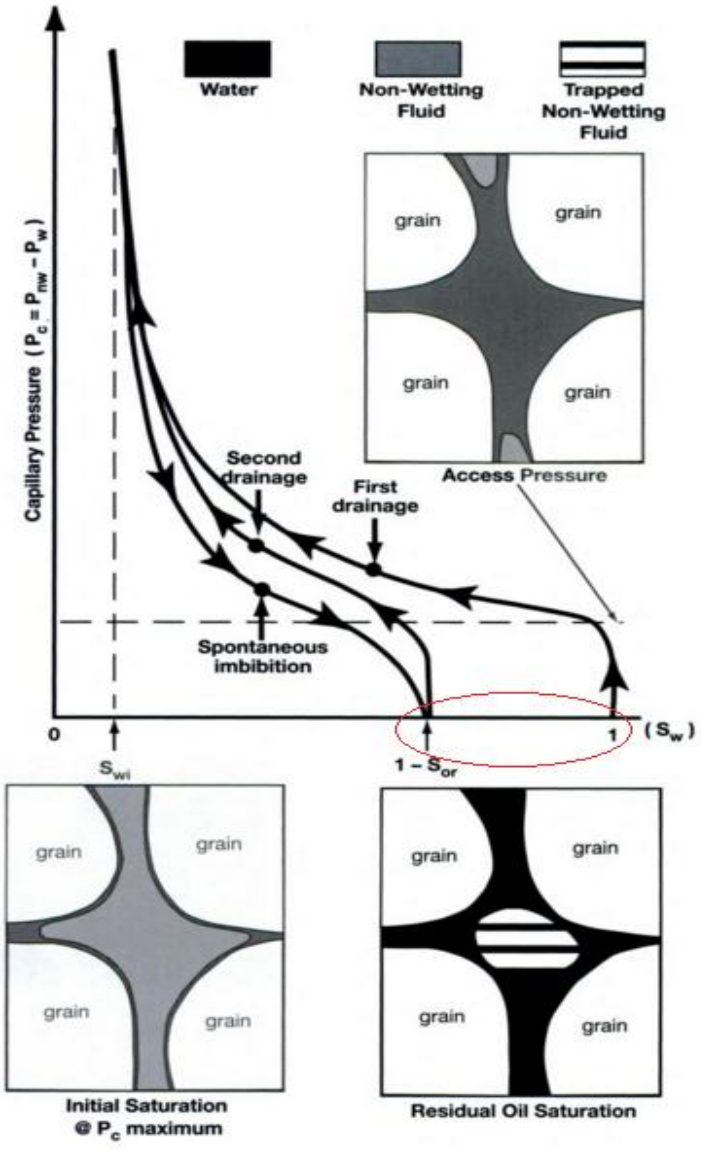

Figure A1: Capillary pressure curve for two phase flow in the conditions of primary drainage, imbibition and secondary drainage, modified from (Zinszner and Pellerin, 2007). The red circle represents the residual oil saturation which is a target for IOR and EOR techniques. The ambition is to remobilize discontinuous oil and hence lowering the residual oil saturation.

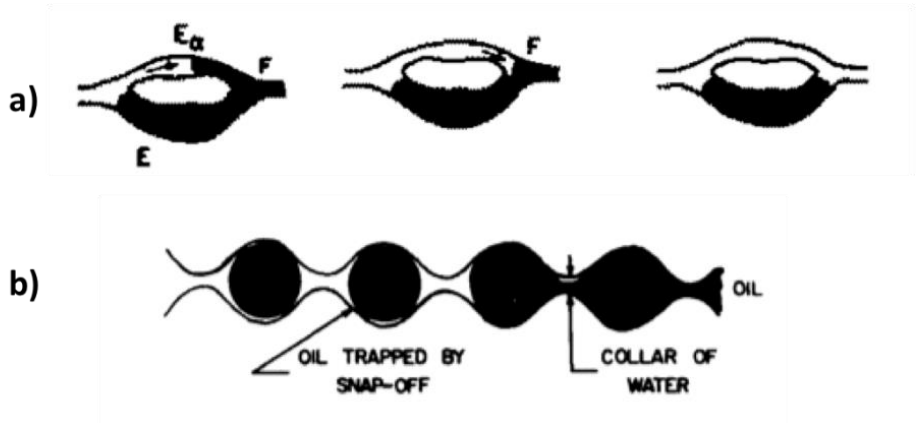

Figure A2: Immobile and discontinuous oil that constitutes the residual oil saturation of a water-wet system after an imbibition process due to bypassing and snap-off, modified from (Skarestad and Skauge, 2014). a) The wetting phase in the small channel bypasses oil in the larger pore because of a higher capillary pressure. b) The wetting phase snaps off in the pore throats due to a high capillary pressure and isolates oil droplets.

AE.2 Capillary Number

During a water flood, reservoir heterogeneity in combination with viscous, capillary and gravitational forces influence both the microscopic and macroscopic sweep efficiency (Dake, 1978). The capillary forces capture the residual oil in the pores, making it more difficult to recover. The viscous forces are related to the velocity and viscosity of the fluid that displaces the oil, and the gravitational force can both stabilize the front and cause segregation. The relationship between the acting viscous and capillary forces in a water/oil system is dimensionless, and defined as the capillary number:

$$N_{vc} = \frac{Viscous\ forces}{Capillary\ forces} = \frac{u_w \mu_w}{\sigma_{ow}} \tag{A6}$$

where u_w [m/s] is the injection velocity of water, μ_w [Pas] is the viscosity of water and σ_{ow} [J/m^2] is the interfacial tension between oil and water. Lake (1989) reports that several laboratory experiments has been conducted to show how the capillary number relates to residual oil saturation presented as a curve called the capillary desaturation curve (CDC). The curve shows that after a certain critical capillary number, the residual saturation decreases, leading to an improved microscopic recovery. The capillary number can be increased by either increasing the viscous forces (injection velocity or viscosity) or by reducing the capillary forces (interfacial tension).

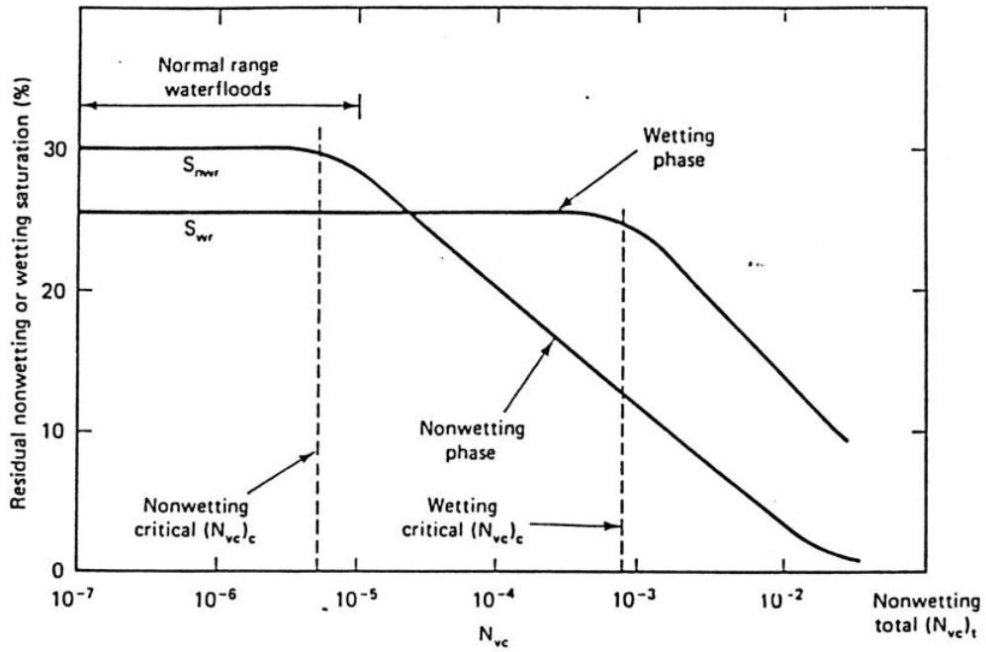

Figure A3: Schematic capillary desaturation curve showing residual saturation (%) vs capillary number. Non-wetting capillary numbers are normally in the range of 10^{-7} – 10^{-5} after conventional water flooding (Lake, 1989).

Appendix F – PET/CT Imaging

Larger individual images from the picture collage in **Figure 46** are presented in this section.

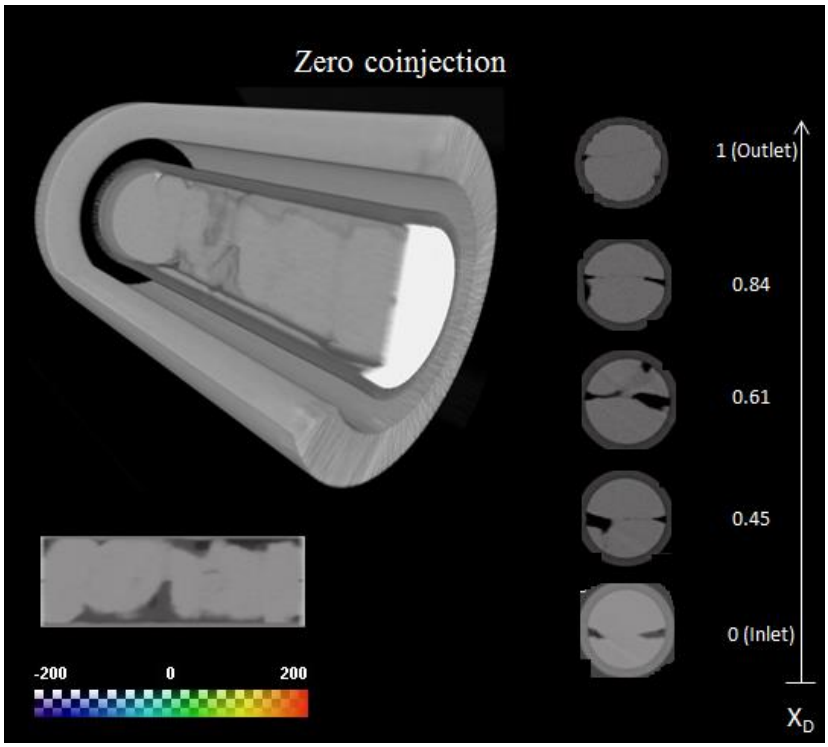

Figure A4: : Zero co-injection

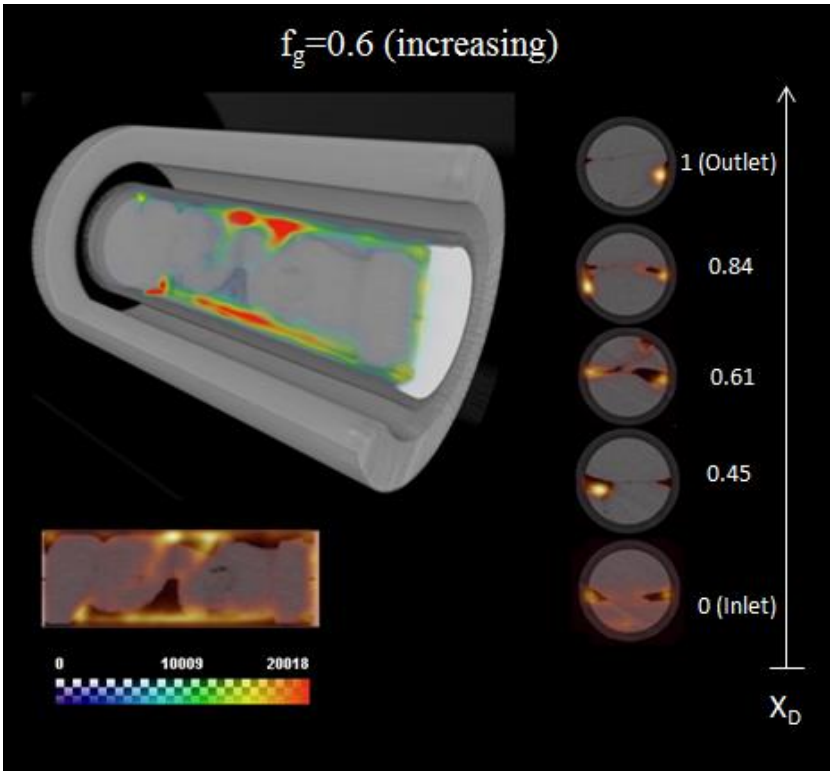

Figure A5: f_g=0.6 (co-injection with increasing gas fraction)

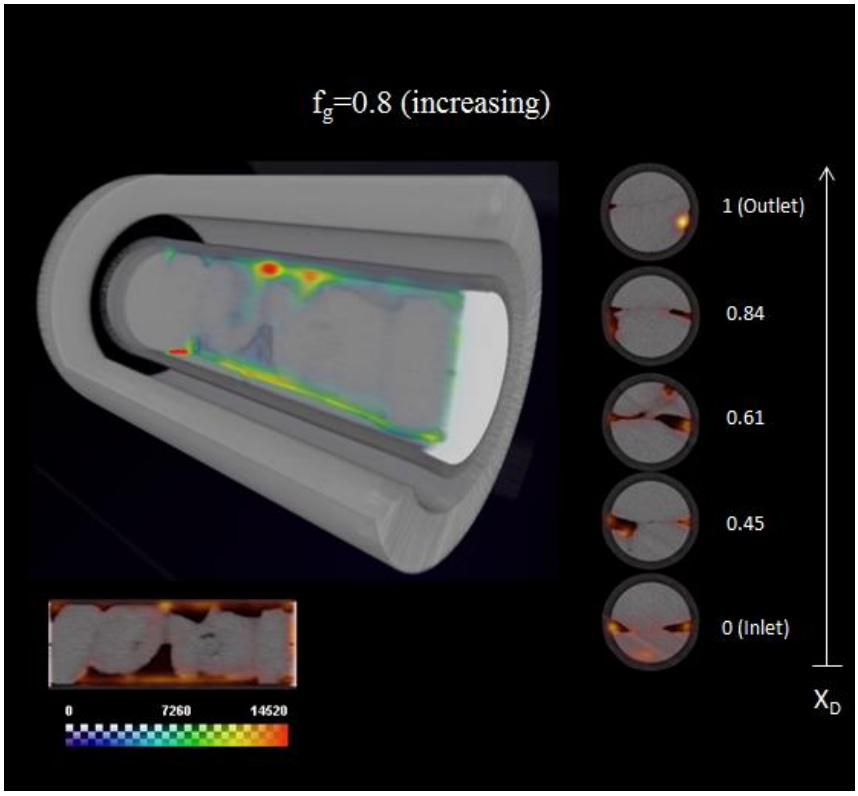

Figure A6: f_g=0.8 (co-injection with increasing gas fraction)

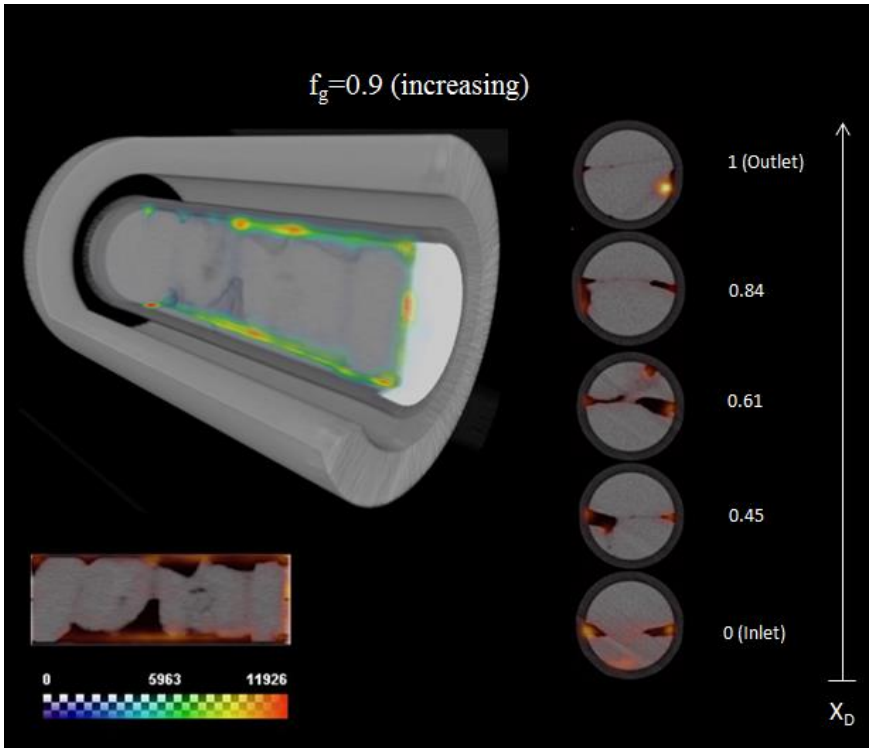

Figure A7: f_g=0.9 (co-injection with increasing gas fraction)

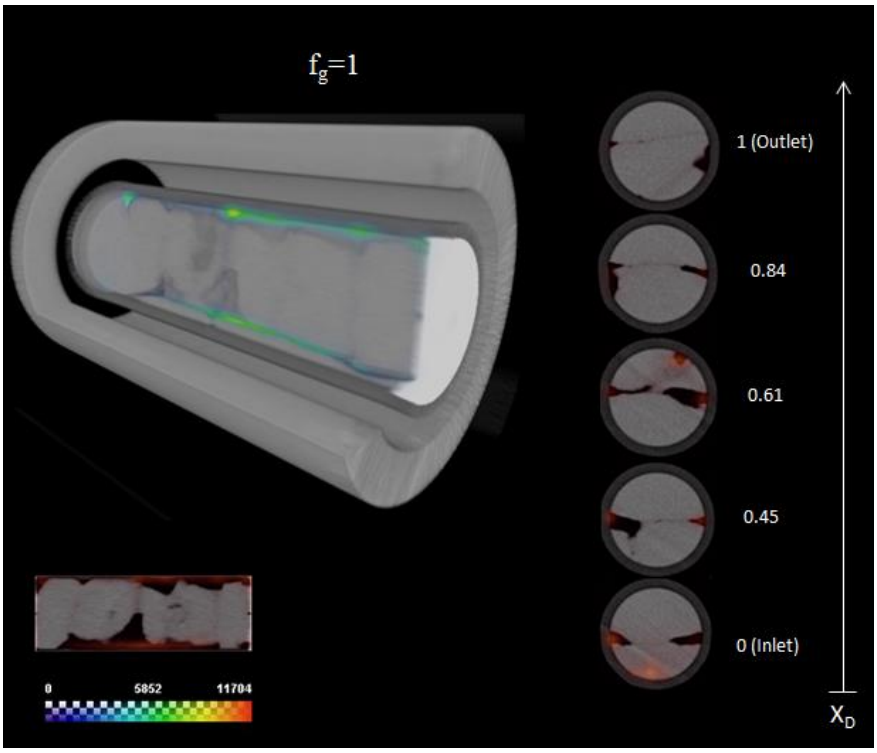

Figure A8: f_g=1

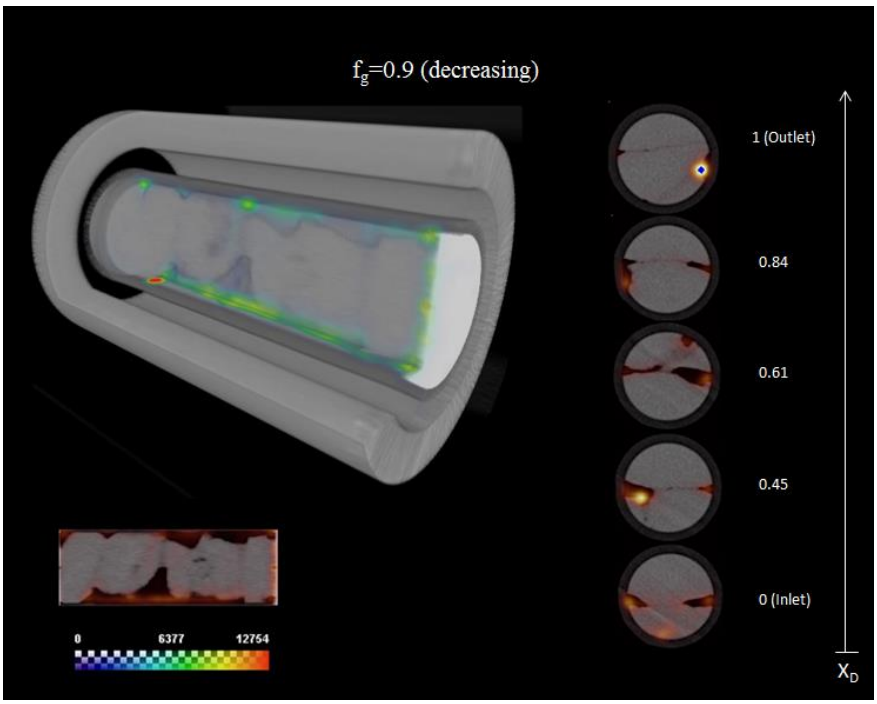

Figure A9: f_g=0.9 (co-injection with decreasing gas fraction)

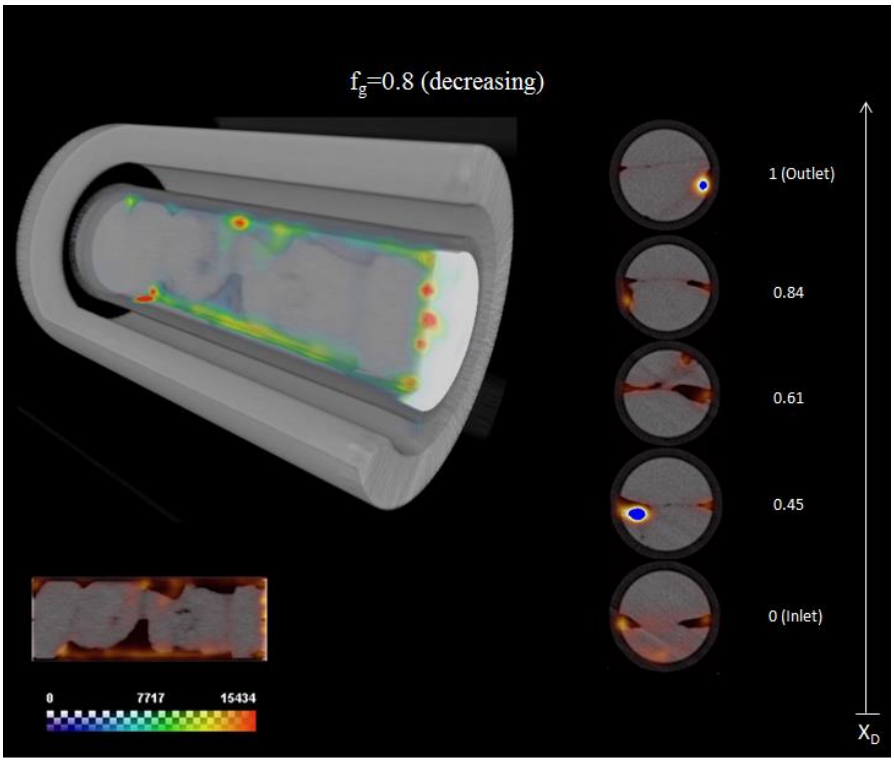

Figure A10: f_g=0.8 (co-injection with decreasing gas fraction)

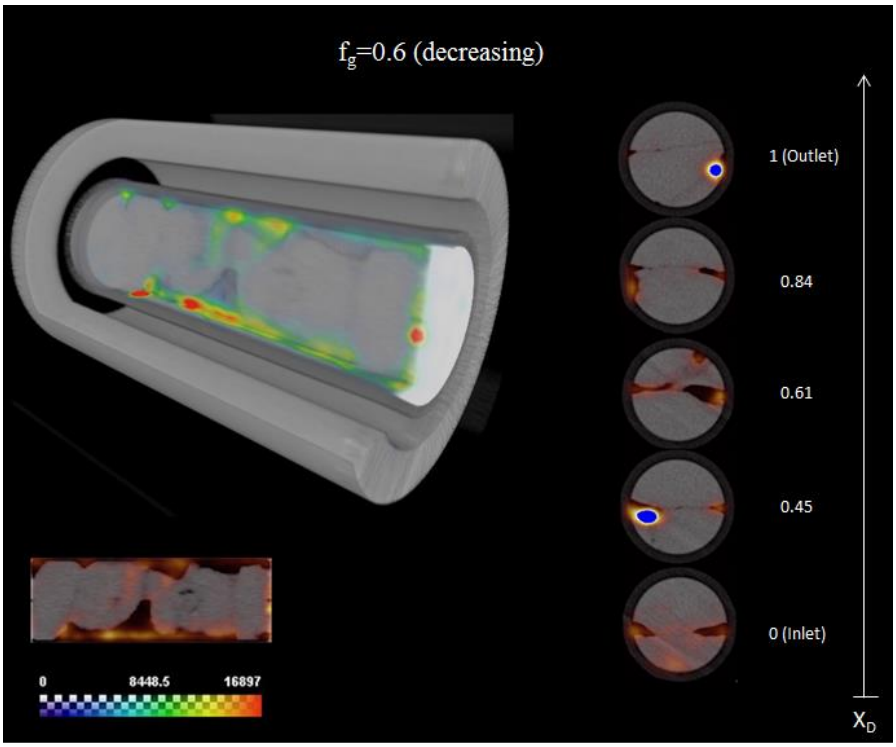

Figure A11: f_g=0.6 (co-injection with decreasing gas fraction)

References

AHMED, T. 2010. *Reservoir Engineering Handbook,* Boston, Gulf Professional Publishing.

ALLAN, J. & SUN, S. Q. 2003. Controls on Recovery Factor in Fractured Reservoirs: Lessons Learned from 100 Fractured Fields. Society of Petroleum Engineers.

BEAR, J., TSANG, C. F. & DE MARSILY, G. 2012. *Flow and Contaminant Transport in Fractured Rock,* Elsevier Science.

BELHAIJ, A., ALQURAISHI, A. & AL-MAHDY, O. 2014. Foamability and Foam Stability of Several Surfactants Solutions: The Role of Screening and Flooding. Society of Petroleum Engineers.

BERNARD, G. C., HOLM, L. W. & HARVEY, C. P. 1980. Use of Surfactant to Reduce CO2 Mobility in Oil Displacement.

BIKERMAN, J. J. 1973. *Foams,* Springer-Verlag Berlin Heidelberg.

BRATTEKÅS, B. 2014. *Conformance Control for Enhanced Oil Recovery in Fractured Reservoirs.* Ph.D., University of Bergen.

BRATTON, T., CANH, D. V., QUE, N. V., DUC, N. V., GILLESPIE, P., HUNT, D., LI, B., MARCINEW, R., RAY, S., MONTARON, B., NELSON, R., SCHODERBEK, D. & SONNELAND, L. 2006. The Nature of Naturally Fractured Reservoirs. *Oildfield Review Summer 2006.*

BUCHGRABER, M., CASTANIER, L. M. & KOVSCEK, A. R. 2012. Microvisual Investigation of Foam Flow in Ideal Fractures: Role of Fracture Aperture and Surface Roughness. 2012 ed. Onepetro.org: Society of Petroleum Engineers.

CASTEEL, J. F. & DJABBARAH, N. F. 1988. Sweep Improvement in CO2 Flooding by Use of Foaming Agents.

CHILINGAR, G. V. & YEN, T. F. 1983. Some Notes on Wettability and Relative Permeabilities of Carbonate Reservoir Rocks, II. *Energy Sources,* 7**,** 67-75.

COOK, M. 2012. *An Introduction to Reservoir Engineering,* Nautilus Limited.

DAKE, L. 1978. *Fundamentals of Reservoir Engineering,* Elsevier Science.

DAS, D. B. & HASSANIZADEH, S. M. 2005. *Upscaling Multiphase Flow in Porous Media: From Pore to Core and Beyond,* Springer Netherlands.

DONNEZ, P. 2007. *Essentials of Reservoir Engineering,* Editions TECHNIP.

ENICK, R. M. & OLSEN, D. K. 2012. Mobility and Conformance Control for Carbon Dioxide Enhanced Oil Recovery (CO2-EOR) via Thickeners, Foams, and Gels - A Detailed Literature Review of 40 Years of Research. U.S. Department of Energy.

ERDAL, A. 2013. Måling og behandling av måledata. *Grunnleggende målevitenskap og eksperimentalfysikk.* Bergen: Institutt for Fysikk og Teknologi.

ERSLAND, G. 2008. Studies of flow mechanisms and hydrate phase transitions in fractured rocks. Department of Physics and Technology, University of Bergen, PhD Thesis.

ETTINGER, R. A. & RADKE, C. J. 1992. Influence of Texture on Steady Foam Flow in Berea Sandstone.

EXEROWA, D. & KRUGLYAKOV, P. M. 1997. *Foam and Foam Films : Theory, Experiment, Application,* Burlington, Elsevier Science.

FARAJZADEH, R., ANDRIANOV, A., KRASTEV, R., HIRASAKI, G. & ROSSEN, W. R. 2012. Foam-Oil Interaction in Porous Media: Implications for Foam Assisted Enhanced Oil Recovery. Society of Petroleum Engineers.

FARAJZADEH, R., WASSING, L. B. M. & BOERRIGTER, P. M. 2010. Foam Assisted Gas Oil Gravity Drainage in Naturally-Fractured Reservoirs. Society of Petroleum Engineers.

FERNØ, M. A. 2012. Enhanced Oil Recovery in Fractured Reservoirs. *In:* ROMERO-ZERÓN, L. (ed.) *Introduction to Enhanced Oil Recovery (EOR) Processes and Bioremediation of Oil-Contaminated Sites.* InTech.

FERNØ, M. A., GAUTEPLASS, J., PANCHAROEN, M., HAUGEN, Å., GRAUE, A., KOVSCEK, A. R. & HIRASAKI, G. 2016. Experimental Study of Foam Generation, Sweep Efficiency, and Flow in a Fracture Network.
FERNØ, M. A., HAUGEN, Å. & GRAUE, A. 2011. Wettability effects on the matrix–fracture fluid transfer in fractured carbonate rocks. *Journal of Petroleum Science and Engineering,* 77**,** 146-153.
FERNØ, M. A., HAUGEN, Å., GRAUE, A. & J.J, H. 2008. The Significance of Wettability and Fracture Properties on Oil Recovery in Fractured Carbonates. *Society of Core Analysts Symposium.* Abu Dhabi.
FIROOZABADI, A. 2000. Recovery Mechanisms in Fractured Reservoirs and Field Performance.
FRIEDMANN, F., SMITH, M. E., GUICE, W. R., GUMP, J. M. & NELSON, D. G. 1994. Steam-Foam Mechanistic Field Trial in the Midway-Sunset Field.
GLOVER, C. J., PUERTO, M. C., MAERKER, J. M. & SANDVIK, E. L. 1979. Surfactant Phase Behavior and Retention in Porous Media.
GLUYAS, J. & SWARBRICK, R. 2012. *Petroleum Geoscience,* Blackwell Publishing.
HADLEY, G. F. & HANDY, L. L. 1956. A Theoretical and Experimental Study of the Steady State Capillary End Effect. Society of Petroleum Engineers.
HATIBOGLU, C. U. & BABADAGLI, T. 2004. Experimental Analysis of Primary and Secondary Oil Recovery From Matrix by Counter-Current Diffusion and Spontaneous Imbibition. Society of Petroleum Engineers.
HAUGEN, Å., FERNØ, M. A., GRAUE, A. & BERTIN, H. J. 2012. Experimental Study of Foam Flow in Fractured Oil-Wet Limestone for Enhanced Oil Recovery.
HENRY, R. L., FISHER, D. R., PENNELL, S. P. & HONNERT, M. A. 1996. Field Test of Foam to Reduce CO2 Cycling. Society of Petroleum Engineers.
HIRASAKI, G. J. & LAWSON, J. B. 1985. Mechanisms of Foam Flow in Porous Media: Apparent Viscosity in Smooth Capillaries. Onepetro.org: Society of Petroleum Engineers.
HJARTNES, T. N. 2015. *An Experimental Study of Tertiary CO_2 Injection Strategies in Fractured Limestone Rocks.* Master's Degree Master Thesis in Reservoir Physics, University of Bergen.
HORJEN, H. 2015. *CO_2 Foam Stabilization with Nanoparticles and EOR in Fractured Carbonate Systems.* Master Degree, Universitetet i Bergen.
HUANG, D. D. & HONARPOUR, M. M. 1996. Capillary End Effects in Coreflood Calculations. *International Symposium of the Society of Core Analysts.* Montepellier, France.
HUBBERT, M. K. 1956. Nuclear Energy and the Fossil Fuel. American Petroleum Institute.
JHA, B. 2011. In The Mix. http://news.mit.edu/2011/fluid-mixing-0519: MIT News.
JOHANSEN, S. A. 2016. *An Experimental Study of Foam Flow in Fractured Systems of Increasing Size.* Master's Degree, University of Bergen.
KAMARI, A., SATTARI, M., MOHAMMADI, A. H. & RAMJUGERNATH, D. 2015. Reliable method for the determination of surfactant retention in porous media during chemical flooding oil recovery. *Fuel,* 158**,** 122-128.
KAPETAS, L., VINCENT BONNIEU, S., DANELIS, S., ROSSEN, W. R., FARAJZADEH, R., EFTEKHARI, A. A., MOHD SHAFIAN, S. R. & KAMARUL BAHRIM, R. Z. 2015. Effect of Temperature on Foam Flow in Porous Media. Society of Petroleum Engineers.
KEELAN, D. K. & PUGH, V. J. 1975. Trapped-Gas Saturations in Carbonate Formations.

KETCHAM, R. A. & CARLSON, W. D. 2001. Acquisition, optimization and interpretation of X-ray computed tomographic imagery: applications to the geosciences. *Computers & Geosciences,* 27**,** 381-400.
KHATIB, Z. I., HIRASAKI, G. J. & FALLS, A. H. 1988. Effects of Capillary Pressure on Coalescence and Phase Mobilities in Foams Flowing Through Porous Media.
KIL, R. A., NGUYEN, Q. P. & ROSSEN, W. R. 2011. Determining Trapped Gas in Foam From Computed-Tomography Images.
KOSSACK, C. A., AASEN, J. O. & OPDAL, S. T. 1989. Scaling-Up Laboratory Relative Permeabilities and Rock Heterogeneities with Pseudo Functions for Field Simulations. *SPE Synposium on Reservoir Simulation* Houston, TX: SPE.
KOVSCEK, A., TRETHEWAY, D., RADKE, C. & PERSOFF, P. 1995. Foam Flow Through A Transparent Rough-Walled Rock Fracture. Onepetro.org: National Energy Technology Laboratory.
KOVSCEK, A. R. & BERTIN, H. J. 2002. Estimation of Foam Mobility in Heterogeneous Porous Media. Onepetro.org: Society of Petroleum Engineers.
KOVSCEK, A. R., PATZEK, T. W. & RADKE, C. J. 1993. Simulation of Foam Transport in Porous Media. Society of Petroleum Engineers.
KOVSCEK, A. R. & RADKE, C. J. 1993. Fundamentals of foam transport in porous media. *Other Information: PBD: Oct 1993.*
KOVSCEK, A. R., TADEUSZ, W. P. & RADKE, C. J. 1997. Mechanistic Foam Flow Simulation in Heterogeneous and Multidimensional Porous Media. Onepetro.org: Society of Petroleum Engineers.
KRISTIANSEN, T. S. & HOLT, T. 1992. Properties of Flowing Foam in Porous Media Containing Oil. Onepetro.org: Society of Petroleum Engineers.
KULL, T., PAXSON, J., SERVICE, U. O. T. A. A. P. E. & DEPARTMENT, A. P. I. P. 1984. *Coring and Core Analysis,* Petroleum Extension Service, Division of Continuing Education, University of Texas at Austin.
KUMAR, A., FARMER, C. L., JERAULD, G. R. & LI, D. 1997. Efficient Upscaling from Cores to Simulation Models. Society of Petroleum Engineers.
KUMAR, A. T. A. & JERAULD, G. R. 1996. Impacts of Scale-up on Fluid Flow from Plug to Gridblock Scale in Reservoir Rock. Society of Petroleum Engineers.
LAKE, L. W. 1989. *Enhanced oil recovery,* Prentice Hall.
LIE, S. H. 2013. *Diffusion as an Oil Recovery Mechanism During CO_2 Injection in Fractured Reservoirs.* Master Degree, University of Bergen.
LOHNE, A., VIRNOVSKY, G. A. & DURLOFSKY, L. J. 2006. Two-Stage Upscaling of Two-Phase Flow: From Core to Simulation Scale.
MAINI, B. & NOVOSAD, J. 1989. Surfactant Retention in Porous Media in Foam Flooding Processes for Enhanced Oil Recovery. *In:* MITTAL, K. L. (ed.) *Surfactants in Solution.* Springer US.
MASOUDI, R., ANN GIDDINS, M., KARKOOTI, H., JALAN, S. & VALERO GIL, A. A. 2015. Foam Simulation From Coreflood to Field Scale. Society of Petroleum Engineers.
NELSON, R. 2001. *Geologic Analysis of Naturally Fractured Reservoirs,* Elsevier Science.
NGUYEN, Q. P. 2011. Gas Trapping During Foamed FLow in Porous Media. *In:* SABA, D. L. (ed.) *Computed Tomography - Special Applications.* InTech.
OMAMI, G., TAMIMI, D. & BRANSTETTER, B. F. 2014. Basic principles and applications of (18)F-FDG-PET/CT in oral and maxillofacial imaging: A pictorial essay. *Imaging Science in Dentistry,* 44**,** 325-332.
OZBAYOGLU, M. E., AKIN, S. & EREN, T. 2005. Foam Characterization Using Image Processing Techniques. Onepetro.org: Society of Petroleum Engineers.

PANCHAROEN, M., FERNØ, M. A. & KOVSCEK, A. R. 2012. Modeling Foam Displacement in Fractures. *Journal of Petroleum Science and Engineering,* 100**,** 50-58.
PERSOFF, P., RADKE, C. J., PRUESS, K., BENSON, S. M. & WITHERSPOON, P. A. 1991. A Laboratory Investigation of Foam FLow in Sandstone at Elevated Pressure. Onepetro.org: Society of Petroleum Engineers.
PRINCEN, H. M. 1983. Rheology of Foams and Highly Concentrated Emulsions: I. Elastic Properties and Yield Stress of a Cylindrical Model System. *Journal of Colloid and Interface Science,* 91**,** 160-175.
RANSOHOFF, T. & RADKE, C. 1988. Mechanisms of Foam Generation in Glass-Bead Packs. Onepetro.org: Society of Petroleum Engineers.
ROMSTED, L. S. 2014. *Surfactant Science and Technology: Retrospects and Prospects,* CRC Press.
ROSSEN, W. R. 1989. Theory of Mobilization Pressure Gradient of Flowing Foams in Porous Media: I. Incompressible Foam. *Journal of Colloid and Interface Science,* Volume 136**,** 1-16.
ROSSEN, W. R. 1990. Theory of Mobilization Pressure Gradient of FLowing Foams in Porous Media - II. Effect of Compressibility. *Journal of Colloid and Interface Science,* 136.
SANCHEZ, J. M. & HAZLETT, R. D. 1992. Foam Flow Through an Oil-Wet Porous Medium: A Laboratory Study. Onepetro.org: Society of Petroleum Engineers.
SANCHEZ, J. M., SCHECHTER, R. S. & MONSALVE, A. 1986. The Effect of Trace Quantities of Surfactant on Nitrogen/Water Relative Permeabilities. Society of Petroleum Engineers.
SANI, A. M., SHAH, S. N. & BALDWIN, L. 2001. Experimental Investigation of Xanthan Foam Rheology. Society of Petroleum Engineers.
SCHLUMBERGER 2016. Carbonate Reservoirs. www.slb.com: Schlumberger.
SCHRAMM, L. L. 1994. *Foams: Fundamentals and Applications in the Petroleum Industry*, American Chemical Society.
SCHRAMM, L. L. 2000. *Surfactants: Fundamentals and Applications in the Petroleum Industry*, Cambridge University Press.
SHAN, D. & ROSSEN, W. R. 2004. Optimal Injection Strategies for Foam IOR.
SHENG, J. 2013. *Enhanced Oil Recovery Field Case Studies*, Elsevier Science.
SHI, J. X. & ROSSEN, W. R. 1998. Improved Surfactant-Alternating-Gas Foam Process to Control Gravity Override. Society of Petroleum Engineers.
SIMJOO, M., DONG, Y., ANDRIANOV, A., TALANANA, M. & ZITHA, P. L. J. 2013. Novel Insight Into Foam Mobility Control.
SINGH, R. & MOHANTY, K. K. 2016. Foams With Wettability-Altering Capabilities for Oil-Wet Carbonates: A Synergistic Approach.
SKARESTAD, M. & SKAUGE, A. 2014. *Reservoarteknikk II,* Bergen, Universitetet i Bergen.
SKAUGE, A., AARRA, M. G., SURGUCHEV, L., MARTINSEN, H. A. & RASMUSSEN, L. 2002. Foam-Assisted WAG: Experience from the Snorre Field. Society of Petroleum Engineers.
SPENCE, G. H., REDFERN, J., AGUILERA, R., BEVAN, T. G., COSGROVE, J. W., COUPLES, G. D. & DANIEL, J. M. 2014. *Advances in the Study of Fractured Reservoirs*, Geological Society.
STEVENSON, P. 2011. *Foam Engineering : Fundamentals and Applications,* Hoboken, Wiley.

SUFFRIDGE, F. E., RATERMAN, K. T. & RUSSELL, G. C. 1989. Foam Performance Under Reservoir Conditions. Society of Petroleum Engineers.
SUNMONU, R. M. & ONYEKONWU, M. 2013. Enhanced Oil Recovery using Foam Injection; a Mechanistic Approach. Society of Petroleum Engineers.
SURGUCHEV, L. M. & HANSSEN, J. E. 1996. Foam Application in North Sea Reservoirs, I: Design and Technical Support of Field Trials. Society of Petroleum Engineers.
WARREN, J. E. & COSGROVE, J. J. 1963. The Effective Mobility Ratio For Immiscible Displacement. Society of Petroleum Engineers.
WARREN, J. E. & ROOT, P. J. 1963. The Behavior of Naturally Fractured Reservoirs.
WILSON, A. J. 2013. *Foams: Physics, Chemistry and Structure*, Springer London.
YAGHOOBI, H. 1994. Laboratory Investigation of Parameters Affecting CO2-Foam Mobility in Sandstone at Reservoir Conditions. Society of Petroleum Engineers.
YU, L. & WARDLAW, N. C. 1986. The Influence of Wettability and Critical Pore-throat Size Ratio on Snap-off. *Journal of Colloid and Interface Science*.
ZHANG, Z., FREEDMAN, V. & ZHONG, L. 2009. Foam Transport in Porous Media - A Review. U. S Deparment of Energy.
ZINSZNER, B. & PELLERIN, F. M. 2007. *A Geoscientist's Guide to Petrophysics*, Editions Technip.
ZOLOTUKHIN, A. B. & URSIN, J. R. 2000. *Introduction to Petroleum Reservoir Engineering*, Høyskoleforlaget, Norwegian Academic Press.